Intrinsic bulk and interface defects in 4H silicon carbide

Lars Sundnes Løvlie

Thesis submitted in partial fullfilment for the
Degree of PhD

Department of Physics
Faculty of Mathematics and Natural Sciences
University of Oslo

© Lars Sundnes Løvlie, 2012

Series of dissertations submitted to the
Faculty of Mathematics and Natural Sciences, University of Oslo
No. 1205

ISSN 1501-7710

All rights reserved. No part of this publication may be
reproduced or transmitted, in any form or by any means, without permission.

Cover: Inger Sandved Anfinsen.
Printed in Norway: AIT Oslo AS.

Produced in co-operation with Unipub.
The thesis is produced by Unipub merely in connection with the
thesis defence. Kindly direct all inquiries regarding the thesis to the copyright
holder or the unit which grants the doctorate.

Abstract

Electrically active, unintentionally introduced defects in a semiconductor crystal may lead to undesirable device properties, and it is therefore important to gain control and understanding of such defects in order to achieve control at device level. Intrinsic defects are usually harder to remove and control than impurities, and in SiC these defects are not only numerous, but also extremely thermally stable, making them somewhat difficult to remove or deactivate. Bulk defects, specifically those corresponding to the $Z_{1/2}$ and $EH_{6/7}$ levels measured using deep level transient spectroscopy (DLTS), appear in concentrations around 10^{12} - 10^{13} cm^{-3} in as-grown material, while the density of interface states (D_{it}) numbers around 10^{14} eV^{-1} cm^{-2} in typical thermally oxidized 4H-SiC material. These two factors severely limit the minority carrier lifetime and the channel mobility in MOS-devices, respectively, and are therefore highly relevant problems to study and - if possible - solve.

This thesis concerns both of the above-mentioned concerns regarding (i) intrinsic bulk defects, mainly regarding the $Z_{1/2}$ and $EH_{6/7}$ levels in DLTS spectra, and (ii) interface defects studied with the capacitance-voltage (C-V) and thermally dielectric relaxation current (TDRC) techniques. We have studied in depth the oxidation-enhanced annealing of $Z_{1/2}$, thus revealing explicitly the depth-distribution of the in-diffusing carbon interstitials during oxidation, and extracted the diffusivity and generation rate using numerical simulations based on a reaction-diffusion model.

We have also studied the diffusion properties of the $Z_{1/2}$, $EH_{6/7}$ and S_1/S_2 defect centers, by irradiating the 4H polytype of SiC with a focused proton beam and subsequently performing laterally and vertically resolved DLTS measurements. These experiments showed that the defects move very long distances during irradiation. The proton radiation ionizes the host atoms and generates an excess of electron-hole-pairs, and it is therefore suggested that the long-distance migration is recombination enhanced. However, there are also several indications that extended defects play a major role, such as the very high degree of anisotropy in the vertical depth distribution, the detection of broadened peaks and very broad features in the DLTS spectra and the simularity between the migration velocity in our case with that previously detected for the recombination-enhanced dislocation glide phenomenon.

Finally, we have studied the fundamental nature of the interface defects in SiO_2 / 4H-SiC MOS structures, and the influence of introducing excess nitrogen during oxidation as a means to lower the D_{it} which is usually considered to be responsible for the low channel mobility in MOSFET devices. An attempt is made at separating the contributions to the combined interface state density from the three distinct types of states which have been distinguished thus far; "true" D_{it}, fast (N_{it}^{fast}) and slow (N_{it}^{slow}) interface states. Our results show that the nitridation mainly reduces the true D_{it}, and also indicates that the N_{it}^{slow} and N_{it}^{fast} originate from different defect centers. We also compare the density of interface states as extracted by different methods (C-V, TDRC and conductance spectroscopy) on the same samples, and study in detail an "anomalous" phenomenon in C-V measurements which is believed to be due to charge transfer between D_{it} and N_{it}^{fast}.

Acknowledgements

As it turns out, research can be quite hard work, and consequently this thesis has been too long in the making. Fortunately, I had the pleasure of performing this work in a research group with extremely hard-working, dedicated and competent people at the UiO MiNaLab group (now Light and Electricity from Novel Semiconductors, LENS).

Thank you, Bengt Svensson, for being an excellent supervisor on both my master- and phd-thesis, and for really setting the standard in both management and research. I also want to thank Edouard Monakhov for being my second supervisor, as well as Ioana Pintilie for several years of great company and for mentoring me in many areas of research! Also, a big thank you to Lasse Vines for bearing with me during our too many late night proton irradiation experiments and for contributing in a large part to those results which we finally managed to get.

I spent a year at the Institute for Energy Research (IFE), another first-class research facility with first-class people and, hence, a terrific social work-environment. Thank you, Sean-Erik Foss, Martin Kirkengen and Ørnulf Nordseth, for being excellent managers and for being flexible when it took much more time to finish this thesis than I initially thought it would.

Thank you, all those who made both my professional and social life enjoyable at MiNaLab and IFE through the years from 2005 - 2012! "Ingen nevnt, ingen glemt", and if you feel left out of this acknowledgement then I most likely meant to give you a big "Thank you" in this paragraph.

Pappa er akademiker, men har aldri hatt noko med naturvitenskap å gjere, mens mamma har teknisk bakgrunn men lite tålmodigheit til overs for «trivialitetar» (i.e. grunnforskning). Sammen gir imidlertid slike personligheiter ein forbausande potent kombinasjon om ein skal seie det sjølv. Derfor må eg jo takke familia mi i Volda, Trondheim, Spania eller kor de no måtte vere akkurat i dag. Det er nok temmelig sikkert at fleire har lurt på om denne dagen virkelig ville komme, og det tenkte eg sjølv også ei stund. Derfor er det hyggelig å kunne overraske med denne avhandlinga no.

Til slutt vil eg takke min - på altfor mange områder - bedre halvdel, nøyaktige korrekturleser og LaTeX-ekspert, vakre sambuar og noverande trivelige kollega, Hanne-Torill Mevik, for at du hadde tålmodigheit med meg heilt til slutten sjølv om det åt opp all mi fritid i mykje lenger tid enn du hadde blitt forespegla. Eg gleder meg stort til at vi no får meir tid sammen til alt det vi skulle fått gjort dei siste åra!

Det blir nok mange motvillige turar til diverse skobutikkar og IKEA for å betale tilbake for over 4 års doktorgradsstudier.

Lars Sundnes Løvlie   Oslo, March 2012

Contents

1 Introduction **1**

1.1 A relevant history of SiC 1

1.2 Motivation for defect studies in SiC 2

2 General and structural properties of SiC **3**

2.1 Crystal structure 3

2.2 Point defects 5

2.3 Diffusion, migration and reaction kinetics 6

2.4 Ion implantation and radiation damage 8

2.5 Capture, emission and recombination of charge carriers 10

3 Experimental techniques and instrumentation **15**

3.1 Capacitance-Voltage measurements 15

3.1.1 On Schottky or pn-diodes 15

3.1.2 On MOS structures 17

3.2 Deep Level Transient Spectroscopy 18

3.2.1 Principle of operation 18

3.2.2 Depth profiling 22

3.2.3 Experimental setup 23

3.3 Thermal Dielectric Relaxation Current 23

3.3.1 Extracting the density of interface states 24

3.3.2 Extracting the total number of traps 27

3.4 Secondary Ion Mass Spectrometry 28

3.5 Ion Implantation 28

4 Previous knowledge and present contributions **31**

4.1 Interface defects in SiO_2 / 4H–SiC structures 31

4.1.1 Thermal oxidation of 4H-SiC 31

4.1.2 Interface defects 32

4.2 Prominent intrinsic defect centers 35

4.2.1 $Z_{1/2}$ 35

4.2.2 $EH_{6,7}$ 37

4.2.3 S_1/S_2 38

4.3 Oxidation-enhanced annealing of point defects 38

4.4 Long range lateral migration of defects 40

4.4.1 Introduction 41

4.4.2 Experiment 41

4.4.3 Results 42

4.4.4 Discussion 44

4.4.5 Summary 47

5 Summary and outlook **49**

6 Summary of the papers **51**

6.1 Paper I 51

6.2 Paper II 51

6.3 Paper III 52

6.4 Paper IV 52

6.5 Paper V 53

6.6 Paper VI 53

6.7 Paper VII 54

6.8 Paper VIII 54

References **55**

List of Figures

2.1 The stacking sequence of 4H-SiC 4

2.2 The temperature dependence of the free electron concentration in Si vs. 4H-SiC 4

2.3 Schematic 2-dimensional lattice, illustrating different types of point defects. 6

2.4 Ion and vacancy depth profiles due to ion implantation. 9

2.5 The band gap and brillouin zone of 4H-SiC. 10

2.6 Energy band diagram of a Schottky barrier junction. 11

3.1 Extracting the doping profile vs. depth using capacitance-voltage measurements. 16

3.2 Band diagram of a MOS structure. 17

3.3 Band diagram illustrating the principle of Deep Level Transient Spectroscopy (DLTS). 20

3.4 The DLTS spectrum and arrhenius plot for extraction of defect parameters. . 22

3.5 Schematic illustration of DLTS setup. 24

3.6 Schematic illustration of the procedure for Thermal Dielectric Relaxation Current (TDRC) measurements. 25

3.7 A simplified diagram of the experimental setup for TDRC measurements . . 25

3.8 The narrow peak of the P-function which appears in the TDRC-formulation plotted vs. energy and temperature 26

3.9 Overview of the Cameca IMS 7f SIMS instrument at MiNaLab 29

3.10 Schematic overview of the NEC 1 MV pelletron ion implanter at MiNaLab 30

4.1 Oxide thickness vs. time for (0001) 4H-SiC at temperatures in the range 1050 - 1175 °C. 32

4.2 Schematic illutration of the density of interface states in the SiC bandgap of SiO_2 / 4H-SiC devices 33

4.3 DLTS spectra with S_1/S_2, $Z_{1/2}$ and $EH_{6/7}$ after low-energy proton surface irradiation 35

4.4 The first-order decay of $Z_{1/2}$ during thermal oxidation after 4.3 MeV Si-implantation, with the concentration recorded at a depth of 0.8 μm from the surface. 39

4.5 Simulated (lines) compared with experimentally measured (symbols) concentration vs. depth profiles after implantation and subsequent annealing at (a) 1100 $^\circ$C and (b) 1175 $^\circ$C. Clearly the solutions for C_I satisfy the demand that [C_I] must be time-independent within the peak-region of the $Z_{1/2}$-distribution. 40

4.6 Micrograph and close-up of proton irradiated area 42

4.7 DLTS spectra after focused beam proton irradiation 43

4.8 Distribution of the $Z_{1/2}$ concentration as a function of the distance from the beam position in the sputtered crater 44

4.9 Lateral distribution of the defects 45

4.10 Depth distribution of the defects 45

List of Tables

2.1 Summary of commonly observed bandgap levels in n-type 4H-SiC. 13

4.1 The band gap position and apparent capture cross section (σ_n) of the trapping centers which are detectable in Fig. 4.7. 43

List of papers

Included papers

I. **Enhanced annealing of implantation-induced defects in 4H-SiC by thermal oxidation**
L. S. Løvlie and B. G. Svensson, *Applied Physics Letters* **98**, 052108 (2011).

II. **Kinetics of oxidation-enhanced annealing of implantation-induced defects in 4H-SiC**
L. S. Løvlie and B. G. Svensson, submitted to *Physical Review B*.

III. **Enhanced annealing of MeV ion implantation damage in n-type 4H silicon carbide by thermal oxidation**
L. S. Løvlie and B. G. Svensson, *Materials Science Forum* Vols. **679-680**, pp. 233-236 (2011).

IV. **A laterally resolved DLTS study of intrinsic defect diffusion in 4H-SiC after low energy focused proton beam irradiation**
L. S. Løvlie, L. Vines and B. G. Svensson, *Materials Science Forum* Vols. **645-648**, pp. 431-434 (2010).

V. **Long range lateral migration of intrinsic point defects in n-type 4H-SiC**
L. S. Løvlie, L. Vines and B. G. Svensson, accepted for publication in *Journal of Applied Physics* (17. Feb. 2012).

VI. **Analysis of electron traps at the 4H-SiC/ SiO_2 interface; influence by nitrogen implantation prior to wet oxidation**
I. Pintilie, C. M. Teodorescu, F. Moscatelli, R. Nipoti, A. Poggi, S. Solmi, L. S. Løvlie and B. G. Svensson, *Journal of Applied Physics* **108**, 024503 (2010).

VII. **Non-nitridated oxides: abnormal behaviour of n-4H-SiC / SiO_2 capacitors at low temperature caused by near interface states**
I. Pintilie, F. Moscatelli, R. Nipoti, A. Poggi, S. Solmi, L. S. Løvlie and B. G. Svensson, *Materials Science Forum* Vols. **679-680**, pp. 346-349 (2011).

VIII. **Interface states in 4H- and 6H-SiC MOS capacitors: a comparative study between conductance spectroscopy and thermal dielectric relaxation current technique**

L. S. Løvlie, I. Pintilie, S. Kumar C. P., U. Grossner, B. G. Svensson, S. Beljakowa, S. A. Reshanov, M. Krieger and G. Pensl, *Materials Science Forum* Vols. **615-617**, pp. 497-500 (2009).

Related, but not included, papers

1. **The influence of excess nitrogen, on the electrical properties of the 4H-SiC / SiO_2 interface**
   I. Pintilie, F. Moscatelli, R. Nipoti, A. Poggi, S. Solmi, L. S. Løvlie and B. G. Svensson, *Materials Science Forum* Vols. **679-680**, pp. 326-329 (2011).

2. **The influence of growth conditions on the annealing of irradiation induced $EH_{6/7}$ defects in 4H-SiC**
   I. Pintilie, L. S. Løvlie, K. Irmscher, G. Wagner, B. G. Svensson and B. Thomas, *Materials Science Forum* Vols. **615-617**, pp. 369-372 (2009).

Chapter 1

Introduction

Silicon carbide is, and has been for over one hundred years, a widely used material due its excellent mechanical properties and hardness. Applications as an electronic material, however, have only fairly recently become the subject of extensive research. Pioneering research began in the early 20th century with important results in industrial bulk production processes of the material and a demonstration of the first ever light emitting diode (LED) in any material. As a semiconductor, and competitor to the omnipresent Si-technologies, SiC is considered superior in many applications requiring high power, temperature or frequency due its large band gap, large dielectric breakdown field, large thermal conductivity, high saturation velocity and very low sensitivity to harsh chemical environments, as has been stated ad nauseum in SiC-related publications. Power electronics today is mostly made of Si, but Si-based transistors stop working at about 200 °C while a corresponding device made of SiC could function well up to perhaps 600 °C (not accounting for packaging-related issues). In principle it now seems fully possible to make integrated devices from SiC, although some technical (and economical) issues still remain to be solved. In addition to its attractive properties, SiC consists of non-toxic and very abundant elements, like Si, contrary to that of competing new materials such as GaN.

1.1 A relevant history of SiC

The seeded sublimation growth technique for the growth of single crystalline SiC substrates was invented in the USSR in the late 1970s, and today this method is used by a number of companies supplying SiC substrates in any of the three most common polytypes 4H, 6H and 3C, with Cree Inc. (estab. 1987) as the largest producer. The most important applications and market drivers are high intensity LEDs (made in a device layer of GaN on either a SiC or sapphire substrate) and power electronics such as Schottky diodes and transistors for rectifier and inverter applications. Substrates of the 4H-SiC polytype have been commercially available since 1994, while 6H-SiC substrates have been available since 1991 [1]. Today, substrates up to 150 mm diameter (6 inches) are commercially available.

1.2 Motivation for defect studies in SiC

Ever since large electronic grade SiC substrates became available they have been plagued with persistent defects which limit performance or reliability and which have been difficult to remove. This includes both structural defects such as stacking faults, dislocations and micropipes, electrically active point defects and a poor quality of the interface between SiC and SiO_2 and other candidate dielectrics for MOS devices such as Al_2O_3. Another important issue was the problem of achieving semi-insulating material, since nitrogen acts as a donor dopant in SiC and hence residual nitrogen easily causes material to become n-doped during growth.

Most impurities have very low diffusivities in SiC, which means that the only relevant technique for selective area doping is ion implantation. Ion implantation inevitably leads to significant numbers of radiation induced defects in the active areas of devices. In addition, two important defect centers with trapping levels in the band gap of 4H-SiC are typically introduced during growth, namely the $Z_{1/2}$ and $EH_{6/7}$ centers, with levels at 0.65 eV and 1.55 eV below the conduction band, respectively. The $Z_{1/2}$ center in particular has been shown to have a detrimental effect on the minority charge carrier mobility and lifetime, and it is therefore important to understand its composition and behavior, and to develop techniques to remove it where necessary. This, in addition to the increasing structural quality and purity of the available SiC material, has led to an increasing focus on the identity and behavior of intrinsic point defects.

Two decades of fairly extensive research efforts have enabled reasonable control over such phenomena as micropipes (micropipe-free substrates are now common) and many other growth related defects. However, most of the various defects in SiC are still far from well understood, and probably among the least understood are intrinsic point defects, some of which are thermally stable up to 2000 °C and therefore difficult to remove. These are point defects related to the fundamental defects like Si or C vacancies, interstitials, antisites and complexes thereof, and this work is focused on the nature and behavior of such defects. The focus of this work is restricted to intrinsic point defects in n-type material of the 4H-SiC polytype (papers I-V) and interface states at the SiO_2 / 4H-SiC interface (papers VI-VIII), although some of the aquired knowledge applies to other polytypes as well.

This thesis is organized as follows; Chapter 2 introduces the necessary background topics for interpretation of the results, chapter 3 describes the experimental methods employed during the course of this work, chapter 4 provides a detailed discussion of previous knowledge along with new knowledge from this work while chapter 5 summarizes those results and some suggestions for future work are presented.

Chapter 2

General and structural properties of SiC

This chapter presents some important background knowledge regarding silicon carbide and semiconductors in general, such as the crystal structure and the electrical behavior and diffusion of defects and reactions between defects. From the perspective of point defects, while they have minor impact on the overall structural properties, it's still crucial to have information on the detailed crystal structure of silicon carbide since this can yield important clues to the identity of the point defects.

2.1 Crystal structure

SiC can exist in an infinite number of polytypes, but the crystal structure of all the polytypes can be thought of as double layers of hexagonal Si- and C-lattices stacked in a specific sequence, as illustrated in fig. 2.1. The hexagonal polytypes have stacking orders such as ABAB, ABCB, ABCACB, etc. for 2H-, 4H- and 6H-SiC, while ABC produces the cubic polytype 3C-SiC. SiC polytypes all have rather wide and indirect bandgaps, with values 2.39, 3.0 and 3.26 eV for the 3C, 6H and 4H polytypes, respectively, and many other properties are also strongly polytype dependent. In other words, two hexagonal lattices are interlaced, the Si- and C-sublattice. Each layer is attached to the layer below through the Si-atom and to the layer above through the C-atom in the base. Thus, a SiC-wafer will be terminated with a layer of Si-atoms on one side and C-atoms on the other side if cut perpendicular to the c-axis, and one can refer to the (0001) Si-face and the $(000\bar{1})$ C-face of a wafer where the numbers in parentheses denote the (hkil) Miller indices of the crystal planes. 3C-SiC is also referred to as β-SiC, while the hexagonal and rhombohedral polytypes are collectively referred to as α-SiC.

Unlike in a single-element material like silicon where all lattice sites are equal in a perfect crystal, in 4H-SiC there are two inequivalent lattice positions: one cubic 'k' site and one hexagonal 'h' site, where all the cubic sites are in the B layers (because the structure immediately below and above is similar to the 3C-SiC structure) while the hexagonal sites are in the A and C layers (because the structure in the immediate vicinity looks like the 2H-SiC structure).

In some cases this can be exploited to find out if two defect centers are related; e.g. in 6H-SiC there are two cubic sites and one hexagonal site, hence if two defect centers appear with a 2:1

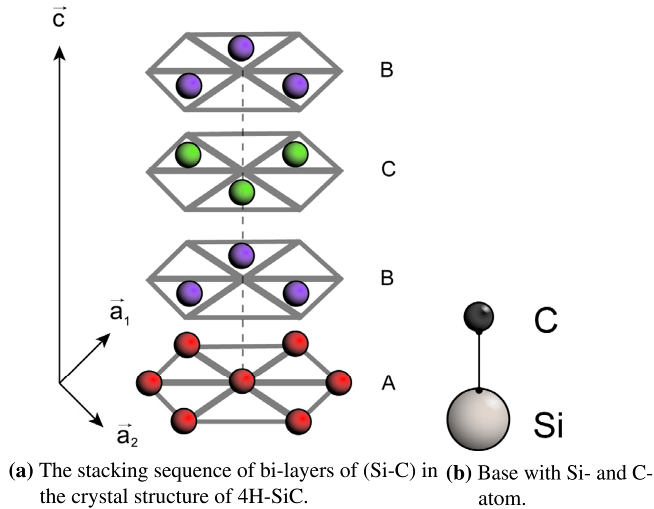

(a) The stacking sequence of bi-layers of (Si-C) in the crystal structure of 4H-SiC. **(b)** Base with Si- and C-atom.

Figure 2.1: The stacking sequence of 4H-SiC, ABCB. At each lattice point (colored spheres) a base consisting of a Si-C pair is positioned.

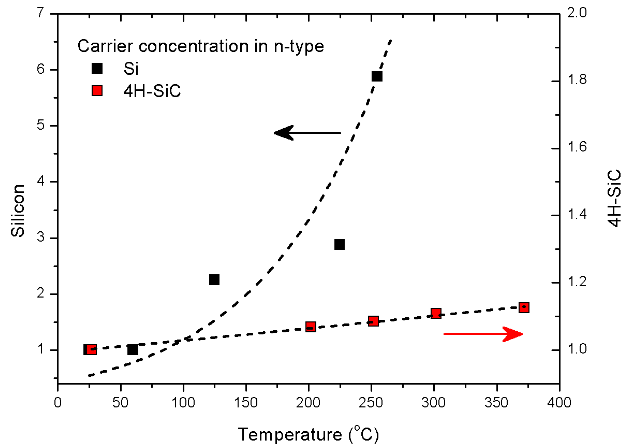

Figure 2.2: The relative increase in free electron concentration, relative to the value at room temperature (RT), in Si and 4H-SiC with increasing temperature. The Si $p^+ - n^- - n^+$ sample had an effective doping level of 8×10^{13} cm^{-3} at RT, while the 4H-SiC Schottky diode had an effective doping concentration of about 2×10^{15} cm^{-3} at RT.

concentation ratio and the annealing behavior is similar then the two centers may be due to the same complex or impurity located at the two unequal lattice sites. This distinction does not appear as easily in 4H-SiC, since it contains equal numbers of cubic and hexagonal sites, hence defect levels which appear in a 1:1 concentration ratio may either be two different defect centers correlated through some reaction mechanism, two different charge states of the same defect center or the same defect but located at the two inequivalent lattice positions.

The Si-C bond may have a slightly ionic character, although they probably have a mainly covalent nature (88%) [2]. SiC does not melt, but rather sublimates directly from solid to gas phase. Commercial material is grown by variations on the so-called seeded sublimation growth, where the solid Si and C feedstock is at about 2400 °C while the seed crystal is at a slightly lower temperature to promote condensation of gas onto the seed [3]. Due to the high density of structural defects in SiC substrates, in particular micropipes, devices are typically fabricated in an epitaxial layer grown by chemical vapor deposition (CVD) techniques with silane and propane as precursor gases.

In terms of impurities and dopants, some preferrably occupy C-sites (N) while others occupy Si-sites (P, Al). This is the basis for site-competition epitaxy for dopant control [4], based on adjusting the Si/C ratio during growth which are activated by occupying substitutional sites. The two unequal lattice sites in 4H-SiC may also lead to two occupancy levels for each dopant. Nitrogen, the most commonly used donor element, has levels at 45 and 100 meV below the conduction band, while aluminium, the most common acceptor, has a slightly deeper acceptor level at about 200 meV above the valence band for all polytypes (the valence bands of 3C-, 4H- and 6H-SiC are almost aligned with each other). The layered structure along the c-axis implies that several material properties — notably the electrical mobility — will be anisotropic to some degree, i.e. the value along the c–axis will differ from that in the so-called basal plane defined by the $\vec{a}$-directions.

Some defects also appear to have extremely anisotropic diffusivity, as observed in long-range migration experiments using a proton beam (paper IV, V and section 4.4), where the diffusivity was found to be very slow in directions close to parallell with the c-axis and very rapid in directions close to the basal plane (in material grown 4°off-axis relative to the c-axis). 4H-SiC is currently the polytype of choice for power and high-temperature applications due its large bandgap and its high and nearly isotropic bulk mobility. Due to the wide bandgaps of the SiC polytypes the thermal generation rate of charge carriers is much smaller than in e.g. silicon, which roughly translates into much higher operating temperatures, which is a large part of the motivation with developing SiC devices in the first place. An informal measurement of the increase in the free carrier concentration in n-type silicon vs. 4H-SiC is included in fig. 2.2. This also implies that in unipolar devices, such as the Schottky diode structures employed in this work, the material contains exclusively majority carriers since thermal generation of minority carriers is negligible at room temperature.

2.2 Point defects

Defects in a crystalline material can have 0, 1, 2, or 3 dimensions depending on whether the defect upsets the short range order of the crystal structure in a point, along a line, in a plane or in a volume. This thesis deals with intrinsic growth- or radiation-induced point

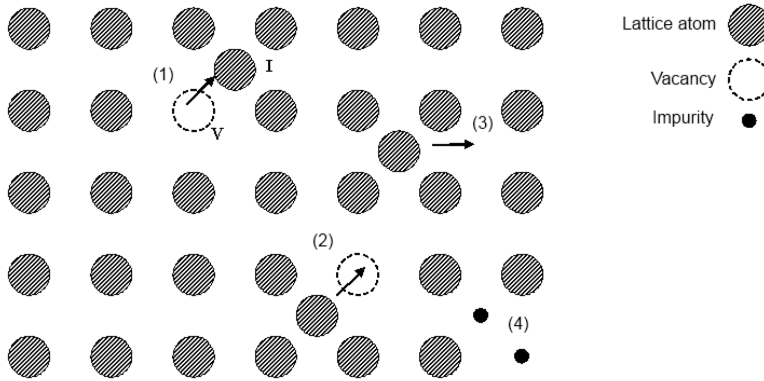

Figure 2.3: A schematic 2-dimensional lattice, illustrating (1) generation of a native interstitial atom, (2) annihilation of an interstitial with a vacancy, (3) a native interstitial atom migrating through the crystal and (4) interstitial and substitutional impurities.

defects in SiC, and these are of a size on the order of the Si- and C-atoms themselves. Point defects in a crystal with 2 elements fall into one of four fundamental categories; vacancies, interstitials, antisites (e.g. Si_C, Si at a C-site and vice versa) and impurities (which may exist in substitutional or interstitial lattice positions). Generation and annihilation of an interstitial and its vacancy (Frenkel pairs) is visualized in an idealized 2-dimensional crystal lattice in figure 2.3. Foreign atoms are referred to as impurities, which are electrically active if they give rise to electron states in the forbidden band gap which can act as recombination or trapping centers. In a compound semiconductor like SiC these defects can reside on either the carbon or silicon sublattice. Thus, carbon and silicon vacancies are referred to as V_{Si} and V_C, while interstitials are referred to as I_{Si} and I_C.

2.3 Diffusion, migration and reaction kinetics

Defect diffusion describes the motion of a random-walking defect through the crystal lattice. First of all, a defect must be created by overcoming a formation energy barrier, and subsequent motion requires the defect to overcome a migration barrier in order to progress from one position to another through the crystal. Defect motion can occur through several processes, such as pure interstitial motion, the vacancy mechanism or the interstitialcy mechanism. In the interstitial mechanism the defect jumps from one interstitial position to another, while in vacancy diffusion a substitutional defect may switch places with a neighboring vacancy to move one lattice position. The interstitialcy process is a two-step process where one specimen first moves into a substitutional position by pushing away the original occupant of that position which subsequently moves into another substitutional position by kicking out the current occupant.

Diffusion is usually a thermally activated process[1]; the defect will need some thermal energy since there is usually a formation and migration barrier to overcome. The diffusivity factors

[1]Some special cases may be athermal, i.e. they can occur even at 0 K, a case in point being migration of the self-interstitial in Si which is driven by cyclic changes in the defect's charge state [5].

into the diffusion equation, which in one dimension for a defect species A with concentration $[A]$ is

$$\frac{\partial [A]}{\partial t} = D \frac{\partial^2 [A]}{\partial x^2} \tag{2.1}$$

The diffusivity, D (cm^2/s), can be anisotropic, in which case it is generally a matrix and the equation must then be solved for the appropriate number of dimensions. The diffusivity can be expressed by the following Arrhenius-relationship

$$D = D_\infty e^{-E_a/kT} \tag{2.2}$$

where D_∞ is a temperature-independent prefactor and E_a is the thermal (activation) energy required for diffusion to occur, including both the formation and migration barrier. The diffusion equation is also referred to as Fick's second law, and it can be derived — by invoking conservation of mass — from Fick's first law which describes the relationship between the flux of defects, J ($1/cm^2s$), and the concentration gradient,

$$J = -D \frac{\partial [A]}{\partial x} \tag{2.3}$$

If a defect has a high enough thermal energy it can either, through migration of either reactant, take part in a reaction with other defects or a defect complex may dissociate into its individual constituents, depending on its particular thermal stability. The thermal stability of a defect species, i.e. the temperature which is required for the species to become mobile or to dissociate, is an important characteristic of the species and sometimes the only property which can be used to correlate measurements of the same defect species between different characterization techniques. Defect reactions are analogous to chemical reactions and are described in the same manner. Thus, the reaction rate, $c(x, t, T)$, which describes the rate of change of the concentration, and the order of a reaction, α, is described as

$$\frac{d[A]}{dt} = -c[A]^\alpha \tag{2.4}$$

The dissociation of species A can be written as

$$A \rightarrow A_1 + A_2 + \ldots + A_n \tag{2.5}$$

where $A_1 \ \ldots \ A_n$ are the individual constituents of A after it has broken up into n parts. A first-order reaction, $\alpha = 1$, such as a dissociation process does not depend on the concentration of any other defect species. The solution is a simple exponential decay from the initial concentration, $[A]_0$,

$$[A] = [A]_0 \ e^{-ct} \tag{2.6}$$

Reactions are usually thermally activated processes and the rate (in units s^{-1}) therefore follows an Arrhenius relationship,

$$c(x, t, T) = c_0(x, t) \ e^{-E_a/kT} \tag{2.7}$$

The prefactor c_0 is usually interpreted as a jump or attempt-to-escape frequency over the potential barrier E_a which must be surmounted for the reaction to proceed. Consequently,

the activation energy for the reaction can be extracted by measuring $[A]$ vs. time at several temperatures and performing a linear fit of $\ln c$ vs. $1/kT$, referred to as an isothermal annealing experiment.

A general second-order diffusion-limited reaction can according to eq. (2.4) be described as

$$\frac{d[A]}{dt} = -c[A_1][A_2] \tag{2.8}$$

In addition to dissociations, a reaction will also follow first-order kinetics even if two defect species are involved if (1) one of the species has a much larger concentration and lower diffusivity than the other, essentially acting as a stationary sink for the diffusing species, or if (2) one of the species is continously replenished from a source. In either of those cases, the rate of change becomes

$$\frac{d[A]}{dt} = -c[A_1][A_2] \equiv c'[A_2] \tag{2.9}$$

where $[A_1] \gg [A_2]$, which consequently yields a first-order annealing behavior for A.

The reaction rate of a diffusion-limited reaction is limited by the rate at which the reactants can migrate, which is intuitively the case in solid-state reactions. In other words, the activation energy for diffusion in eq. (2.2) is larger than the one for reaction in eq. (2.7). Thus, if the reactants have enough energy to be mobile, then they will also most likely have enough energy to react if they encounter each other. The reaction rate of a diffusion-limited second order reaction can be expressed as $c = 4\pi R(D_{A_1} + D_{A_2})$ [6], where R is a geometrical factor called the reaction radius, usually assumed to be of the order 1-10 nm. The general solution in the second-order case yields a non-linear relationship between $\ln c$ and $1/kT$.

The general equation to be solved for each species, here written in terms of the simultaneous reaction $A_1 + A_2 \rightarrow A$ and dissociation $A \rightarrow A_1 + A_2$, is

$$\frac{\partial[A(x,t)]}{\partial t} = -c_{diss}[A] + 4\pi R(D_{A_1} + D_{A_2})[A_1][A_2] + D_A \frac{\partial[A(x,t)]}{\partial x^2} \tag{2.10}$$

where c_{diss} is the dissociation rate of A. If the defect A is involved in further reactions, then the corresponding equations must be solved simultaneously with the above equation in order to determine $[A(x,t)]$ at all times.

2.4 Ion implantation and radiation damage

The energy loss, or stopping, of energetic ions and subatomic particles such as protons or electrons as they traverse a crystal structure cause non-permanent damage by ionizing the host atoms, referred to as electronic stopping, and possibly permanent damage by knocking out and displacing the host atoms themselves, referred to as nuclear stopping. Displaced host atoms may quickly find their way back to a substitutional site, so-called dynamic annealing which repaires the crystal before the damage can be detected, or they may migrate away as interstitials and subsequently form stable defects. At least 90% of all Frenkel pairs, a displaced host atom and the vacancy it leaves behind, in SiC anneal dynamically during

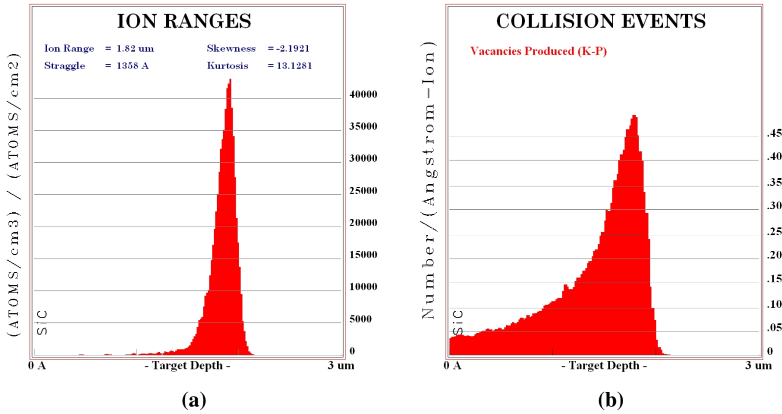

Figure 2.4: (a) Incident ion and (b) vacancy depth profile per incident ion and Ångström as a consequence of ion implantation of 4.3 MeV Si-ions, as simulated by TRIM [8].

ion implantation, while the remainder end up forming stable defect configurations [7]. In the context of ion implantation the goal is to cause displacement of host atoms and for the implanted impurities to find a suitable position in the crystal lattice, thereby causing the dopant to become electrically active with at least one shallow donor or acceptor level in the bandgap. The displacement damage typically becomes more frequent as the particles slow down, and a distinctive tail leads up to a pronounced peak in the concentration of defects which is formed near the projected range of the particles. The damage can be simulated by using Monte-Carlo methods, and an implantation profile is illustrated in Fig. 2.4 for 4.3 MeV Si-ions [8]. A typical ion implantation to introduce dopants into the material is performed at elevated temperature, perhaps as high as 1000 °C, and followed by a post-implant activation anneal at around 1500 °C [9].

Due to the significantly larger mass of Si compared to C, the former requires the transfer of a larger amount of energy from the incident particle for displacement of the lattice Si atom to occur. The threshold for displacing C-atoms is thought to be about 20 eV while for Si-atoms it is closer to 30 eV, which in the case of electron irradiation translates into a necessary particle energy of about 150 keV for displacing C-atoms and 300 keV or higher energy for Si-atoms [10]. This difference has been exploited, selectively creating only C-related defects, in order to investigate the origins of various defect signatures [11–13].

Ion implantation of Si- or C-ions, electron and proton radiation produce a rich variety of intrinsic defects in 4H-SiC, several of which introduce trapping levels in the upper part of the bandgap which are therefore detectable in investigations performed on n-type material. The most prevalent are the $Z_{1/2}$ and $EH_{6/7}$ levels at E_C - 0.65 eV and E_C - 1.55 eV, respectively. These levels are the only ones to consistently appear in as-grown 4H-SiC, in concentrations of about 10^{12} - 10^{13} cm^{-3}, and they also appear in greatly increased concentration after irradiation when followed by a low-temperature anneal (about 200 °C) which makes less stable defects mobile [14].

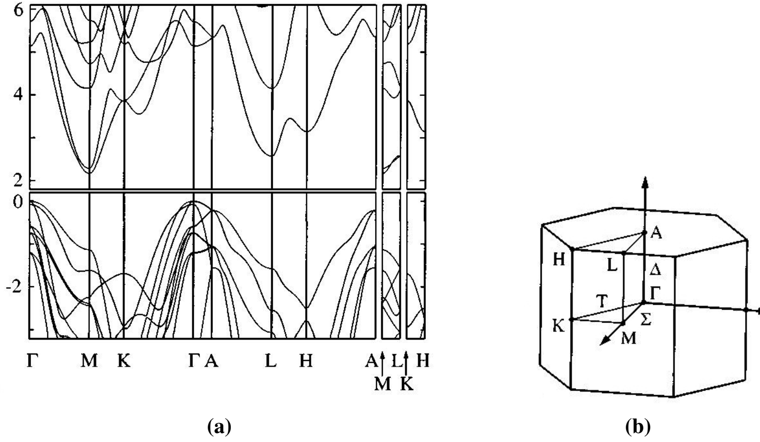

(a) (b)

Figure 2.5: (a) The band gap of 4H-SiC calculated using DFT methods, from [15]. The minimum, indirect band gap is between the Γ and M directions of the wavevector. (b) The brillouin zone of 4H-SiC.

2.5 Capture, emission and recombination of charge carriers

Electronic states in the band gap of a semiconductor are introduced by imperfections in the crystal structure generated during the growth, by impurities which are introduced either intentionally (doping) or unintentionally (contamination) during processing or generated during ion implanation or irradiation by elementary particles. The various valence and conduction bands of 4H-SiC, calculated using ab-initio methods, are shown in Fig. 2.5, where the indirect band gap between the M and Γ k-points in reciprocal space is also visible. Electronic states which are located closer to either band edge than about 200 meV (less in Si) are usually referred to as shallow levels and will act as donors or acceptors at 50 - 100 K and above. Conversely, levels which are further from the band edges are deep levels and may cause serious problems since they can act as efficient recombination centers. Alternatively deep levels can be intentionally introduced in active parts of a device where the lifetime needs to be tailored, e.g. in the base region of bipolar switches to increase the switching frequency or reduce the recombination loss during switching.

The occupancy of a trapping level in the band gap changes by exchanging electrons with the conduction band and holes with the valence band, through emission and capture processes. These thermally activated processes are described by emission and capture rates of the respective charge carriers; traps which are unoccupied by electrons can either capture an electron from the conduction band or emit a hole to the valence band, and vice versa for occupied traps. Thus, the occupancy changes as

$$\frac{dn_t}{dt} = (c_n + e_p) \cdot (N_t - n_t) - (e_n + c_p) \cdot n_t \tag{2.11}$$

where $c_{n/p}$ is the capture rate of electrons / holes, $e_{n/p}$ is the emission rate of electrons / holes and N_t is the total number of traps and n_t is the number of occupied traps. Many electrical

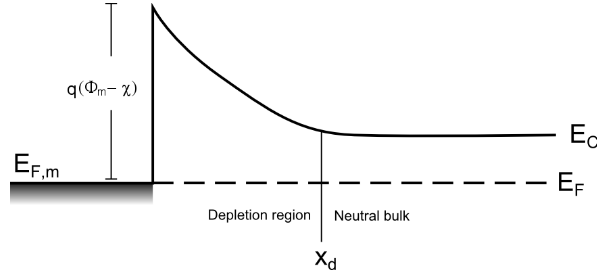

Figure 2.6: Schottky barrier junction at no applied bias. Φ_m is the workfunction of the metal, χ is the electron affinity of the semiconductor and x_d is the depletion depth. With reverse bias applied E_F shifts down and x_d moves deeper into the semiconductor, leaving behind a greater positive space charge due to fixed donors in the depletion region to compensate for the negative charge on the metal electrode.

characterization methods use samples with a pn- or Schottky junction where the capture process in the substrate material can effectively be stopped by applying a reverse bias across the junction, which depletes the material within the space charge region of charge carriers and leaves only the transient discharging of charge carriers from already occupied traps (cf. Fig. 3.3). This allows the extraction of the emission rate of charge carriers from a trap, since (2.11) then simplifies to

$$\frac{dn_t}{dt} = -e_n n_t \tag{2.12}$$

in n-type material with a negligible concentration of holes, unless intentionally injected from the p-side of a pn-junction by applying a forward bias prior to the reverse bias. Capture processes occur while no reverse bias is applied. Clearly the trap occupancy under reverse bias follows simple exponential decay.

$$n_t = N_t \exp(-e_n t) \tag{2.13}$$

Figure 2.6 contains a schematic illustration of the mechanism behind a Schottky rectifying junction, where the Fermi level in the metal, $\mathrm{E_{F,m}}$, is equal to the Fermi level $\mathrm{E_F}$ in the SiC (with no applied bias). The Schottky barrier, $\Phi_\mathrm{B} = q(\Phi_\mathrm{m} - \chi)$, determines the small saturation current of electrons from the metal to the conduction band in reverse bias. The important property of the junction for the purposes of electrical characterization is the depletion region, which extends from the metal / semiconductor interface and down to x_d contains a certain density of ionized fixed donors. x_d increases with increasing reverse bias, as described in section 3.1.

At thermal equilibrium with no applied bias $dn_t/dt = 0$, and the capture and emission processes must balance out for each carrier type according to the principle of detailed balance, so eq. (2.11) yields

$$N_t c_n - n_t(c_n + e_n) = 0 \tag{2.14}$$
$$N_t e_p - n_t(c_p + e_p) = 0 \tag{2.15}$$

Solved for the electron occupancy of the trap this leads to

$$\frac{n_t}{N_t} = \frac{c_n}{e_n + c_n} = \frac{e_p}{e_p + c_p} \tag{2.16}$$

However, the occupancy can also be described by the Fermi-Dirac distribution function,

$$\frac{n_t}{N_t} = f(E_t) = \frac{1}{1 + e^{(E_t - E_F)/kT}} \tag{2.17}$$

where $f(E_t)$ is the probability of finding an electron at the trap position E_t, k is the Boltzmann constant and E_F is the Fermi level which is determined by the effective doping in the material. Inserting for the above into eq. (2.16) yields the following for the emission rates

$$e_{n/p} = c_{n/p}\ e^{\pm(E_t - E_F)/kT} \tag{2.18}$$

Ignoring the effect of entropy and considering only electrons, the capture rate can be shown to be equal to $c_n = \sigma_n\ v_{th}\ n$, where the carrier concentration n can be written in terms of the Fermi level and the density of states in the conduction band, to finally yield

$$e_n = \sigma_n\ v_{th}\ N_c\ e^{-(E_c - E_t)/kT} \tag{2.19}$$

σ_n is the capture cross section for electrons, v_{th} is the thermal velocity of the carriers and N_c is the density of states in the conduction band. From the expressions for e_n and c_n one can see that the capture rate is proportional to the carrier concentration, as one would expect, but not to the trap position, while the emission rate depends on the trap position and capture cross section which are characteristic properties of the trapping level. The extraction of these parameters, in addition to the concentration, from the emission rate is the principal goal of many electrical characterization techniques.

However, the energy required to move an electron from $\mathrm{E_t}$ and inserting it into $\mathrm{E_c}$ is the chemical potential, which is equivalent to the Gibbs energy $\Delta G(T) = E_c - E_t \equiv \Delta H - T\Delta S$, where the rightmost expression follows from a thermodynamic identity between G and the enthalpy H and entropy S. Inserting this into equation (2.19) yields

$$e_n = e^{\Delta S/k}\ \sigma_n\ v_{th}\ N_c\ e^{-\Delta H/kT} \tag{2.20}$$

where $\sigma_{na} \equiv e^{\Delta S/k}\ \sigma_n$ and ΔH are referred to as the apparent capture cross section and activation enthalpy, respectively.

In order for recombination to occur, the trap must be in communication with both bands since recombination requires the trapping of first one kind of carrier and then trapping of the other kind before the first carrier is emitted. The emission rate of a level in the band gap is large if it is close to either band edge, although this also depends on $\sigma_{n/p}$. In this case trapped charge carriers may spend too little time at the level for recombination to occur, and it most likely behaves as a trapping center without contributing much to recombination. A deep level which is far from either band may act mainly as a recombination center since trapped carriers spend a longer time at the level, which increases the probability of trapping carriers of both polarities before the first one is emitted. The energy position below the conduction band edge and σ_n of the most relevant intrinsic deep levels in the upper half of the band gap of 4H-SiC are summarized in table 2.1.

Label	Position below E_C (eV)	Extrap. σ_n (cm^2)	Meas. σ_n (cm^2)	Reference
$Z_{1/2}$	0.60 – 0.70 eV	5×10^{-14}	5×10^{-17}	[14, 16–18]
$EH_{6/7}$	1.50 – 1.65 eV	5×10^{-13}	$> 5 \times 10^{-15}$	[16–18]
S_1	0.40 – 0.45 eV	5×10^{-15}	8×10^{-17}	[16, 19, 20]
S_2	0.72 eV	$10^{-14} - 10^{-15}$	3×10^{-15}	[19, 20]

Table 2.1: Summary of commonly observed bandgap levels in n-type 4H-SiC.

Chapter 3

Experimental techniques and instrumentation

The various experimental techniques which were used to produce the results presented in this thesis will be briefly introduced in this chapter. Particular emphasis is placed on deep level transient spectroscopy (DLTS) for studies of bulk defects with trapping levels in the band gap and thermal dielectric relaxation current (TDRC) for measurents of interface states in metal - oxide - semiconductor structures.

3.1 Capacitance-Voltage measurements

Capacitance-voltage characterization (C-V) characterization of a sample with a p-n or Schottky junction allows the measurement of the mean effective carrier concentration or its depth distribution from the junction and towards the bulk, as well as extracting the interface density of states in a MOS structure and their behaviour as a function of applied voltage, frequency and temperature.

3.1.1 On Schottky or pn-diodes

A p^+n- or Schottky-junction structure is effectively a parallel plate capacitor with the following voltage-dependent capacitance

$$C(V) = \frac{\epsilon_s A}{x_d(V)} \tag{3.1}$$

where ϵ_s is the permittivity of the semiconductor, A is the junction area and x_d(V) is the width of the depletion region into the base.

All C-V measurements on junctions in this work were performed on Ni / 4H-SiC Schottky contacts, deposited by e-beam or thermal evaporation, with circular Ni contacts of various

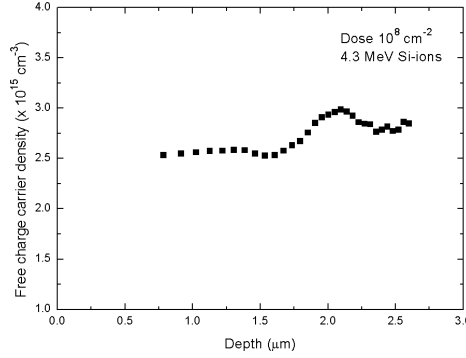

Figure 3.1: The doping profile of a N-doped Ni / 4H-SiC Schottky diode which has been implanted with 4.3 MeV Si-ions measured at 287 K. The effective bulk doping level is 2.8×10^{15} cm^{-3}, but implantation induced deep levels from the surface and down to the projected range of about 1.5 μm cause partial compensation of the nitrogen donors.

diameters (1 mm or smaller). The depletion capacitance of a p^+n or Schottky-junction on n-type material, where one can consider $N_A \gg N_D$, is given by

$$C = \frac{dQ}{dV} = \frac{\epsilon_s A}{x_d} = \epsilon A \sqrt{\frac{q}{2\epsilon (V_{bi} - V) N_D}} \tag{3.2}$$

It is often necessary to measure the effective doping profile, $N(x_d)$, e.g. as an input parameter to DLTS depth profiling of defect levels outlined in section 3.2.2. The charge density in a small volume Adx of the depletion region generated by a voltage change dV is $\rho = qN(x_d)$. Starting with Gauss's law,

$$\nabla \cdot \vec{E} \approx \frac{\Delta E}{\Delta x_d} = \frac{\rho}{\epsilon} \tag{3.3}$$

where E is the electric field, which is assumed to be normal to the surface. Since $\Delta V = x_d \Delta E$, this can be written in terms of $N(x_d)$ after inserting for ρ, as

$$N(x_d) = \frac{\epsilon}{q} \frac{\Delta V}{x_d \Delta x_d} \tag{3.4}$$

Differentiating eq. (3.2) and inserting yields

$$N(x_d) = -\frac{C^3}{q \epsilon_s A^2 (\Delta C / \Delta V)} \tag{3.5}$$

where x_d is calculated from the measured capacitance by using eq. (3.1). A typical effective doping profile in a Ni / 4H-SiC Schottky diode is presented in Fig. 3.1. This diode was implanted with 4.3 MeV Si-ions to a dose of 10^8 cm^{-2}, which causes partial compensation due to deep levels in the material from the surface and down to below the projected implantation peak range of 1.5 μm. The apparent small peak in the effective doping around 2 μm is an artifact introduced by the deep acceptor levels, and is entirely artificial [21].

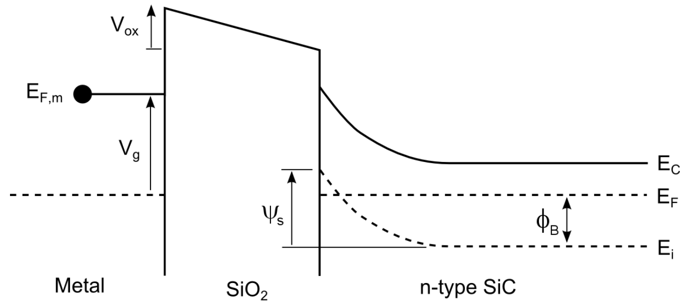

Figure 3.2: Band diagram of a MOS structure on n-type SiC in depletion-inversion, since the surface band bending, ψ_s, is larger than the bulk potential, ϕ_B, which means that the material is effectively p-type at the surface. The valence band is not shown.

3.1.2 On MOS structures

Defect states at the interface between the 4H-SiC wafer and a thermal oxide (or a deposited dielectric) are able to trap charge carriers. Their trapping and emission properties change with temperature and frequency, and the surface band bending changes with the applied bias. Thus, performing C-V measurements over a certain range of these parameters will reveal information regarding their nature and in particular their density and position in the band gap.

The band diagram of a MOS structure on an n-type semiconductor is illustrated in Fig. 3.2, where V_g is the applied gate bias, V_{ox} is the potential drop over the oxide, ψ_s is the surface band bending and ϕ_B is the so-called bulk potential determined by the bulk epi-layer doping. The MOS capacitor is depicted in depletion or weak inversion, although mobile inversion charge in SiC can be neglected due to the wide band gap which yields very low thermal generation rate of minority carriers. This means that the capacitor will be driven into deep depletion in response to an applied negative bias on the gate electrode, since only the positively ionized space charge is available to compensate the applied negative gate charge.

In an ideal capacitor without interface traps, a change in gate bias leads to a change in gate charge which must be compensated for by an equally large change in the charge near the surface of the semiconductor, realized by a change in the surface band bending. In a MOS device which contains interface traps, however, for the same applied gate bias that same charge on the semiconductor side will also fill trapping centers at the interface, which means that a smaller portion of the charge must reside in the semiconductor. This again leads to a smaller band bending than if there were no interface traps. Hence a larger bias is needed to bring the capacitor into accumulation, which means that the C-V curve is stretched out due to the charge trapped at interface states.

Although the stretchout of the C-V curve is independent on the measurement frequency, the measured capacitance is affected differently by interface traps when measured at low and high frequency. At a given DC bias and at high frequency the rapid variation of the Fermi level at the surface in response to the frequency of the small AC probing voltage will not give the interface traps time to emit any trapped charge carriers. Thus, they will not contribute any capacitance to the measured value, C_{hf}, and instead act as fixed charges. However, they will

change occupancy in response to the slowly varying DC bias during a gate voltage sweep, leading to the stretch-out effect described above. At low frequency the traps will be able to respond by both emitting and trapping charge carriers during a period of the AC signal, hence contributing an extra interface capacitance, C_{it}, to the measured value, C_{lf}. This difference between C_{hf} and C_{lf} can be used to calculate the D_{it} by observing that at low frequency the measured capacitance in depletion is

$$\frac{1}{C_{lf}} = \frac{1}{C_{ox}} + \frac{1}{C_s + C_{it}} \tag{3.6}$$

while at high frequency

$$\frac{1}{C_{hf}} = \frac{1}{C_{ox}} + \frac{1}{C_s} \tag{3.7}$$

Solving the above for the semiconductor capacitance, C_s, and inserting into the expression for C_{lf} yields D_{it} in terms of the measured low- and high-frequency capacitance by using its relation to the interface capacitance, $C_{it} = q^2 D_{it}$.

$$D_{it} = \frac{C_{ox}}{q^2} \left(\frac{C_{lf}/C_{ox}}{1 - C_{lf}/C_{ox}} - \frac{C_{hf}/C_{ox}}{1 - C_{hf}/C_{ox}} \right) \tag{3.8}$$

The low-frequency capacitance is typically *not* measured with a capacitance bridge and a low AC frequency, but rather by observing that

$$C \equiv \frac{dQ}{dV} = \frac{dQ}{dt}\frac{dt}{dV} = \frac{I}{dV/dt} \tag{3.9}$$

Hence, a measured I-V curve is directly proportional to C_{lf} by applying a linear voltage ramp, $V = V_0 + \beta t$.

3.2 Deep Level Transient Spectroscopy

Deep level transient spectroscopy (DLTS) [22] is one of many electrical characterization techniques which takes advantage of the fact that the availability of free charge carriers near a pn-, Schottky-junction or MOS-capacitor can be turned on and off by applying forward or reverse bias across the device, respectively. Thus, it is possible to isolate the processes of trapping of electrons or holes in a specific volume during forward or zero bias, and emission during reverse bias. The concentration (N_t), bandgap position (activation enthalpy, E_a) and apparent capture cross section ($\sigma_{n/p}$) can be extracted by studying the decay of the depletion capacitance during the emission of charge carriers from trapping levels after application of a filling pulse (reducing the reverse bias momentarily) to populate the trapping levels with charge carriers.

3.2.1 Principle of operation

A DLTS measurement starts out with a reverse bias V_r across the junction, and any majority carrier trap levels within the band gap in the depletion region are at equilibrium occupancy

(unoccupied), $n_t(t=0)=0$. No charge trapping occurs within the depletion region, except in a thin transition region between neutral bulk material and the depleted region, since all free carriers are swept out by the electric field. A forward voltage pulse V_p is then superimposed on the reverse bias for a specified pulse width t_p (typically about 50 ms), reducing the depletion region width to $x_p < x_d$. During the filling pulse traps in the previously depleted region, $x_p < x < x_d$, are exposed to free charge carriers, allowing charge trapping to occur. The filling pulse is set long enough to achieve full occupancy of the trap levels. At the end of the filling pulse the sample is again reverse biased at V_r and all charge trapping within the depletion region stops while only emission of trapped carriers occurs. In the case of majority carrier traps the depletion region contracts towards its equilibrium value because the emission of charge carriers from the defect centers leads to an increase in the space charge, and this contraction is monitored as an exponential increase in the depletion capacitance. This capacitance transient, $\Delta C(t)$, can be related to the concentration and trap properties (E_t and $\sigma_{n/p}$) by integrating the Poisson equation

$$\frac{\partial^2\psi}{\partial x^2} = -\frac{\rho(x,t)}{\epsilon_s\epsilon_0} \tag{3.10}$$

The temperature is scanned over a certain range, which corresponds to a scan over a corresponding range of E_t and $\sigma_{n/p}$. In n-type material with a donor-like level, if there is only one trap participating in the emission process at a given temperature then the position-dependent charge density is,

$$\rho(x,t) = q\left[N_{eff}^{+} + (N_t - n_t(t))\right]$$

where N_{eff}^{+} is the effective doping level and $0 \leq n(t) \leq N_t$, with $n(t=0)=N_t$. Immediately after a voltage pulse the depletion region can be divided into three regions with different ρ, as indicated in Fig. 3.3. Traps in the region $0 \leq x \leq x_p - \lambda$ are never filled and therefore this region has a constant charge density $N_{eff}^{+} + N_t$. The extracted trap concentration will be underestimated if this effect is not taken into account, since the measurement volume would appear larger than it actually is. Conversely, traps in the region $x_d - \lambda \leq x \leq x_d$ are never emptied, hence this region has a constant charge density N_{eff}^{+}. The charge density in the shaded area in the figure follows the above equation, increasing towards the equilibrium value at reverse bias as the occupancy $n(t)$ decreases with time from N_t towards 0. Integrating eq. (3.10) twice across the depletion region yields the voltage drop across the junction,

$$V(t) = \frac{1}{\epsilon_s\epsilon_0}\int_0^{x_d} x\rho(x,t)dx \tag{3.11}$$

As the traps emit their electrons under reverse bias the voltage over the junction will try to change to accommodate the increase in space charge density. However, in a constant-voltage DLTS system the instrumentation will keep the reverse bias constant during the emission. Thus, differentiating the voltage and equating to zero yields,

$$\left[N^{+}x_d + (N_t - n_t)(x_d - \lambda)\right]\frac{dx_d}{dt} = \frac{1}{2}\left[(x_d(t)-\lambda)^2 - (x_p(t)-\lambda)^2\right]\frac{dn_t}{dt} \tag{3.12}$$

In these calculations the assumption has been made that λ is only a function of temperature, it does not vary with voltage. In the so-called dilute limit the following is valid

$$N^{+} \approx N_d \gg N_a, N_t, n_t$$

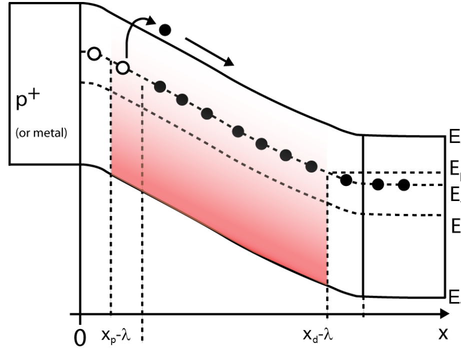

Figure 3.3: A band diagram illustrating the principle of DLTS. A trapping level E_t can be filled by superimposing a pulse bias V_p on top of the reverse bias $-V_r$. When the pulse bias is removed the sample returns to $-V_r$ and the occupancy of the traps within the measurement region (shaded) decays towards 0 with time.

Then the left hand side in eq. (3.12) greatly simplifies to

$$\begin{aligned} N_d x_d \frac{dx_d}{dt} &= \frac{1}{2}\left[(x_d(t)-\lambda)^2 - (x_p-\lambda)^2\right]\frac{dn_t}{dt} \\ \frac{dx_d/dt}{x_d} &= -\frac{dC_{rb}/dt}{C_{rb}} = \frac{1}{2}\frac{\left[(x_d(t)-\lambda)^2 - (x_p-\lambda)^2\right]}{x_d^2}\frac{1}{N_d}\frac{dn_t}{dt} \end{aligned} \tag{3.13}$$

where the reverse bias capacitance, $C_{rb}(t) = \epsilon_{Si}\epsilon_0 A/x_d(t)$, is introduced and the change in capacitance during the emission process is assumed to be small so C_{rb} is approximately constant. Integrating from t to $t=\infty$, using equation (2.13) and that $n_t(\infty)=0$ yields the exponential capacitance transient,

$$\Delta C(T,t) = -\Delta C_0 e^{-e_n(T)t} \tag{3.14}$$

The maximum amplitude of the transient is

$$\Delta C_0 = \frac{1}{2}\frac{(x_d(t)-\lambda)^2 - (x_p-\lambda)^2}{x_d^2}\frac{N_t}{N_d}C_{rb} \tag{3.15}$$

Equation (3.14) is a good approximation when the depletion approximation can be assumed, when the trap concentration is within the dilute limit and for uniform N_d and N_t. If $x_d \gg \lambda, x_p$ then equation (3.15) further simplifies to

$$\Delta C_0 = \frac{N_t}{2N_d}C_{rb}$$

Otherwise the factor

$$\alpha \equiv \frac{(x_d-\lambda)^2 - (x_p-\lambda)^2}{x_d^2}$$

can be expressed in terms of the measured reverse and pulse bias capacitance, C_p, as

$$\alpha(T) = \frac{(x_d-\lambda(T))^2 - (x_p-\lambda(T))^2}{x_d^2} = 1 - \left(\frac{C_{rb}}{C_p}\right)^2 - \frac{2C_{rb}}{\epsilon_{Si}\epsilon_0 A}\left(1-\frac{C_{rb}}{C_p}\right)\lambda(T) \tag{3.16}$$

λ can be found by integrating Poisson's equation twice and finding the point where the deep level crosses the Fermi-level. The result is

$$\lambda = \left[\frac{2\epsilon}{e^2 N_d} \left\{ E_c - E_t - kT \ln \left(\frac{N_c}{n} \right) \right\} \right]^{1/2} \tag{3.17}$$

The DLTS spectrum can now be constructed from a collection of capacitance transients recorded during a temperature scan. The spectrum is defined by

$$S_i(T) = \frac{1}{n_i} \sum_{t_j = t_d}^{t_d + t_i} \Delta C(T, t_j) w(t_j) \tag{3.18}$$

where $w(t)$ is a specific weighting function, n_i is the number of measured capacitance values in the i'th so-called rate window, t_i is the time length of the rate window. If the sampling interval between each measured capacitance value in a transient is τ, then $t_i = n_i \tau$. $t_d = \tau/2$ is the time at the start of the summation, which is a time delay to allow the instrumentation to recover from overload during the pulse bias. An example of a DLTS spectrum using the lock-in weigthing function, which has been almost exlusively used in this thesis, is shown in Fig. 3.4(a). The lock-in weighting function is defined as follows,

$$w = \begin{cases} -1 & 0 < t < t_i/2 \\ 1 & t_i/2 < t < t_i \end{cases} \tag{3.19}$$

The length of the time window determines at which value of the emission rate, $e_n(T)$, the spectrum has a maximum value. This can be understood by noting that for peaks in the DLTS spectrum one must have

$$\frac{dS}{dT} = \left(\frac{dS}{d(e_n t_i)} \right) \left(\frac{d(e_n t_i)}{dT} \right) = 0$$

where the last factor is zero only for $T = 0$, which is irrelevant. Thus, DLTS peaks appear only at a certain value of $e_n t_i = e_n^{peak} t_i$ for each rate window and for a certain weighting function, and therefore the peak temperature is characteristic for the defect and the rate window.

The concentration is found by rewriting equation (3.18) as

$$S_i(T) = \Delta C_0 \underbrace{\frac{1}{n_i} \sum_{t_d}^{t_d + t_i} e^{-e_n(T) t_j} w(t_j)}_{\equiv F_i = F_i(t_d, t_i, e_n(T))} \tag{3.20}$$

The term labeled as F_i has the same value for all peaks in a certain rate window since $e_n(T) = e_n^{peak}$ at a peak, and F_i therefore is a numeric factor which is characteristic for each rate window of a certain weighting function. Therefore, at a DLTS peak the amplitude of the peak is simply proportional to the concentration of the defect. In other words, the concentration extracted using rate window i is,

$$N_{t,i} = \frac{2N_d}{C_{rb}(T_{peak}) \alpha(T_{peak})} \times \frac{S_{i,peak}(T_{peak})}{F_i} = \frac{N_{t,i}(\alpha = 1)}{\alpha} \tag{3.21}$$

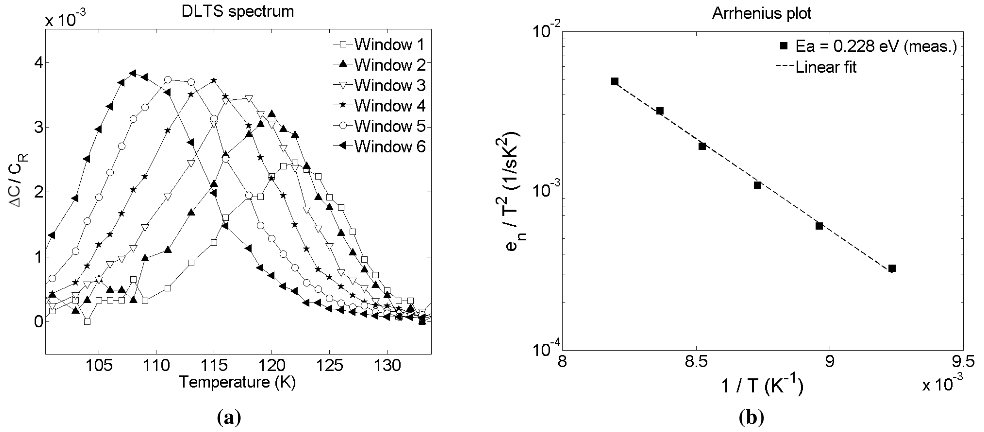

Figure 3.4: (a) The DLTS peaks for a certain trapping center generated by a lock-in weighting function, using 6 rate windows of length $20 \times 2^{i-1}$ ms, where $i = 0 \dots 5$. (b) The activation enthalpy and apparent capture cross section is extracted by plotting the emission rate, which is the same at each DLTS peak, divided by the peak temperature squared.

The activation enthalpy and apparent capture cross section can be found from a DLTS temperature scan by observing that, according to eq. (2.20),

$$\ln(e_n/T^2) = -\frac{\Delta H}{k}\frac{1}{T} + \ln(B\sigma_{na}) \tag{3.22}$$

where all T-independent factors in e_n are lumped together in the factor B;

$$v_{th,n}(T)\ N_c(T) = \sqrt{\frac{3kT}{m_n^*}}\ 2\left(\frac{2\pi m_n^* kT}{h^2}\right)^{3/2} = B\ T^2 \tag{3.23}$$

ΔH is found from the slope of an Arrhenius plot of equation (3.22) and σ_{na} is found from the extrapolated intersection with the e_n/T^2-axis as $1/T \to 0$, as seen in Fig. 3.4(b).

3.2.2 Depth profiling

The concentration vs. depth profile for a deep level can be extracted from DLTS measurements. The temperature is kept constant at the peak temperature of the deep level in question (in a given rate window) and the reverse bias is fixed, which determines the maximum depth for the measurement. The pulse bias is then increased from the reverse bias (V_p = 0), which probes the concentration at the deepest point, and towards V_p = +V_r, which probes the concentration up towards the width of the built-in depletion region. Differentiating eq. (3.15) with respect to the depletion width during the pulse bias and using eq. (3.11) to relate a voltage change δV_p to a change in depletion width δx_p, one finds

$$N_t(x_p - \lambda) = -\left(\frac{1}{1 - \lambda C_p/\epsilon A}\right)\frac{q\epsilon A^2 N^+(x_d) N^+(x_p)}{C_r^3 F_i}\frac{\partial S_i}{\partial V_p} \tag{3.24}$$

where $\epsilon = \epsilon_s \epsilon_0$, S_i/F_i has been inserted for ΔC_0 and the parallel plate formula has been used to relate depletion width to the capacitance.

3.2.3 Experimental setup

A simplified illustration of the experimental setup is shown in Fig. 3.5. Four different setups with smaller variations in the instrumentation and with different cryostats were employed in this work; a custom made high-temperature (150 - 800 K) cryostat, one custom made setup with a commercial liquid nitrogen (LN_2) cooled low-temperature cryostat (77 - 450 K) and another commercial (Semilab) setup with an identical cryostat, and finally a very low temperature closed-cycle He-cooled custom-made cryostat (20 - 350 K). The high-temperature cryostat was equipped with the HP-4280A capacitance-bridge and an Agilent 81110A pulse generator, the custom made LN_2-cooled setup had another HP-4280A and a HP8112A pulse generator, while a Boonton 7200 capacitance bridge and the Agilent 81110A pulse generator was connected with the He-cooled setup.

The HP-4280A directly samples a capacitance transient and transmits it digitally to the computer for analysis via the GPIB bus, while a data aquisition unit with an analog to digital converter is required in the case of the Boonton 7200 which only has analog transmission of data. The commercial Semilab setup uses proprietary hardware and software, while the other setups were equipped with LabVIEW for the data aquisition process and plotting.

A DLTS measurement starts out with the sample at a specified reverse bias V_r, applied by the capacitance bridge. The pulse generator (Agilent 81110A or HP8112A) receives a trigger signal from the capacitance bridge to apply a square filling pulse, V_p, of a specified amplitude and length, e.g. 10 V for 50 ms, across the sample, reducing the reverse bias to V_r - V_p for the duration of the pulse. When the filling pulse ends, the bias returns to V_r and the capacitance bridge samples the capacitance for a specified time, typically 640 ms in this case, yielding 6 lock-in rate windows. The measured data of capacitance and time, C(t), are then transmitted to the computer LabVIEW software which calculates the DLTS signal according to equation (3.18). The full capacitance transient is stored, which means that the DLTS spectrum can subsequently be calculated off-line using any weighting function. This procedure repeats continuously while the temperature is scanned in the desired range.

3.3 Thermal Dielectric Relaxation Current

The thermal dielectric relaxation current (TDRC) technique, first described by Simmons and co-workers in the 1970's [23], is derived from the older thermally stimulated current (TSC) technique [24] developed to study bulk traps on samples with pn-junctions. It is useful for extracting the density of interface and near-interfacial states of a MOS capacitor.

As schematically described in Fig. 3.6, a TDRC measurement starts with applying a charging bias on the sample at high temperature (approx. room temperature). The charging bias must be large enough to drive the MOS capacitor into accumulation to make sure that majority carriers are available for capture near the interface. The capacitor is then cooled with the charging bias applied, and the bias is switched to a discharging bias when a given low temperature is reached, T_0, which is typically around 50 K. The discharging bias shifts the capacitor into depletion, which stops all further capture processes and only emission processes need to be taken into account. Thermal emission is typically negligible at such a low temperature, but the temperature is now increased according to a fixed ramp rate, β

$$T = T_0 + \beta t$$

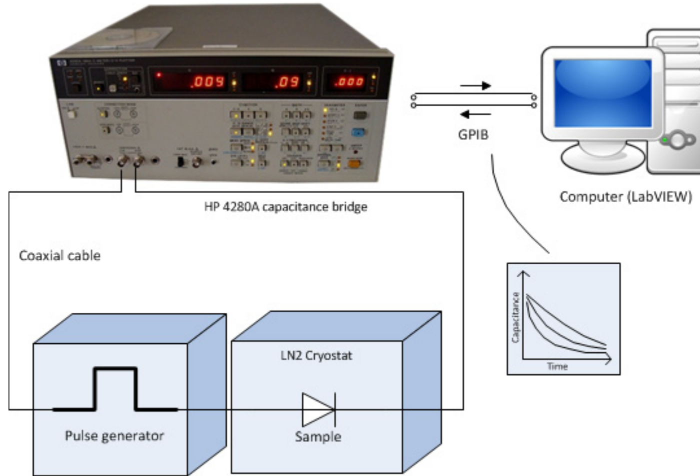

Figure 3.5: A schematic illustration of the low- and high-temperature setups for DLTS and C-V measurements. The capacitance bridge outputs C-t capacitance transients which are transformed into a DLTS temperature spectrum using several different weighting functions on the computer.

while the emission current is monitored. A simplified diagram of the necessary equipment is presented in Fig. 3.7.

3.3.1 Extracting the density of interface states

At the interface between SiO_2 and n-type SiC, a continuous distribution of electron states is assumed to exist and since $n \gg p$ the following holds for the emission of electrons from filled traps, δn_t, at energy levels between E and $E + dE$,

$$\frac{d(\delta n_t)}{dt} = -e_n n_t dE \equiv -e_n \delta n_t \tag{3.25}$$

where n_t is the number of filled traps per unit area per unit energy, or equivalently the area density of a single trapping level. This equation is analogous with eq. (2.12) for discrete deep levels. Thus, the contribution to the measured thermal emission current from this level is

$$\delta I = -qA\frac{d(\delta n_t)}{dt} \tag{3.26}$$

where $q = |e|$. The total current is found by integrating this equation over the band gap. Equation (3.25) can now be rewritten in terms of temperature, using the constant ramp rate,

$$\frac{d(\delta n_t)}{dt} = \frac{d(\delta n_t)}{dT}\beta = -e_n n_t dE \tag{3.27}$$

The general solution to this equation is,

$$\delta n_t = N_{it}(E)\exp\left\{-\frac{1}{\beta}\int_{T_0}^{T} e_n n_t dT'\right\} \tag{3.28}$$

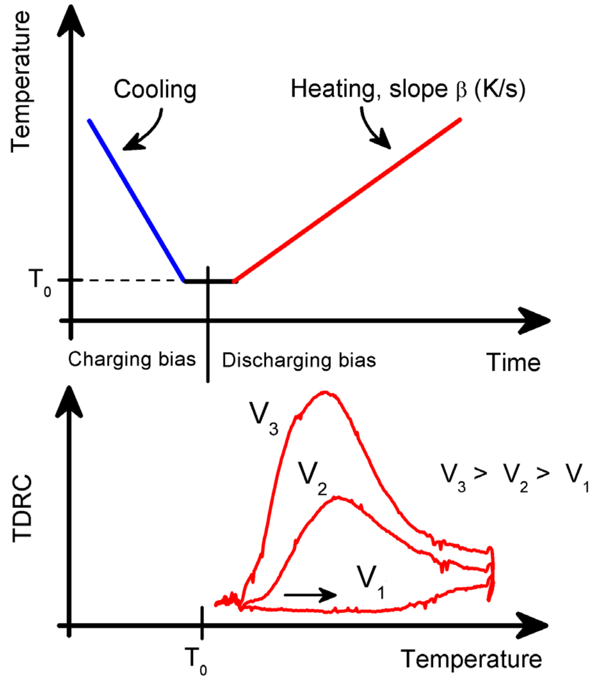

Figure 3.6: Schematic illustration of the procedure for Thermal Dielectric Relaxation Current (TDRC) measurements.

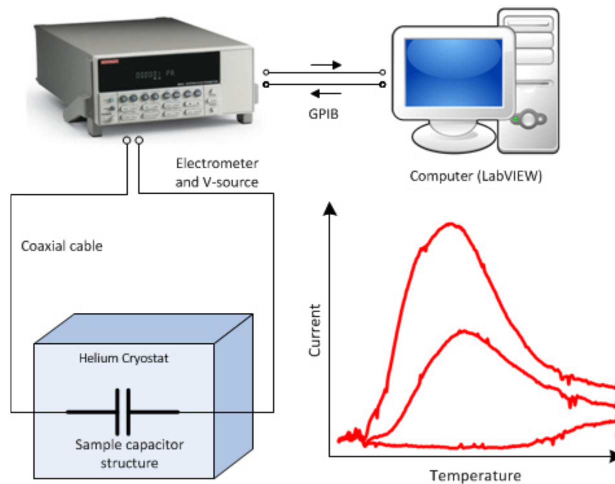

Figure 3.7: A simplified diagram of the experimental setup for TDRC measurements. In this case a closed-cycle He-cooled cryostat was used rather than the liquid/gas N_2 cryostat used for DLTS measurements, since it is essential that the heating rate is well controlled. The graph in the lower right panel shows typical I-T measurements as recorded by the electrometer (as in Fig. 3.6).

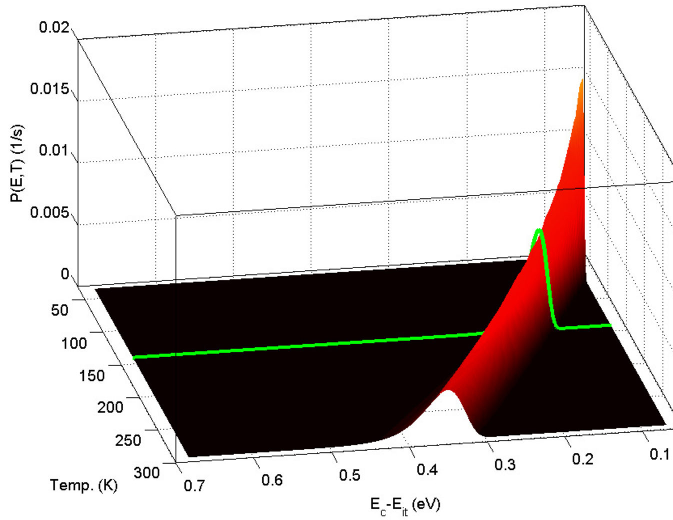

Figure 3.8: A plot of $P(E,T)$ for a temperature-independent $\sigma = 10^{-16}$ cm^2. The green line is included to better show the narrow peak-like shape of P vs. energy and for constant temperature.

where N_{it} is the density of filled traps at E at T_0. The thermal relaxation current follows

$$I(T) = qA \int_{E_v}^{E_c} N_{it} e_n \exp\left\{-\frac{1}{\beta}\int_{T_0}^{T} e_n dT'\right\} dE \equiv qA \int_{E_v}^{E_c} N_{it}\, P(E,T)\, dE \quad (3.29)$$

This equation is exact, with no approximations or assumptions apart from the fact that only emission processes are allowed to contribute to the current. The density of interface states, N_{it}, can be extracted from the measured current vs. temperature spectrum.

In order to extract $N_{it}(E)$, the complicated factor which has been labeled as $P(E,T)$ must first be evaluated,

$$P(E,T) = e_n \exp\left\{-\frac{1}{\beta}\int_{T_0}^{T} e_n dT'\right\} \quad (3.30)$$

The integral can be written out with the explicit temperature dependence of e_n,

$$\int_{T_0}^{T} e_n dT' = \gamma \int_{T_0}^{T} T'^2 \sigma_n \exp\left(-\frac{\Delta E}{kT'}\right) dT' \quad (3.31)$$

where σ_n is the capture cross section for capture of electrons and $\Delta E = E_c - E$ is the position of the trapping level below the conduction band. Hole capture is assumbed to be negligible. The factor $\gamma T'^2$ is equal to $v_{th} N_c$ in the emission rate, with the T-dependence written explicitly and other factors lumped in γ. However, knowledge of the T-dependence of σ_n must be applied, or some assumption must be invoked.

The $P(E,T)$ factor takes the shape of a sharp peak as a function of E for fixed T, with a full width at half maximum (FWHM) on the order of 0.05 eV. A plot of $P(E,T)$ is in Fig. 3.8,

for a T-independent capture cross section $\sigma = 10^{-16}$ cm^2. Because of this, Simmons argues that the approximation

$$D(T)\delta(E_m - E) \approx P(E, T) \tag{3.32}$$

is valid, where E_m is the energy position of the maximum of $P(E, T)$ at a given T and $D(T)$ (in units of eV/s) is the area under the peak at this temperature. Under this approximation, eq. (3.29) can be written as

$$I(T) = qA \int_{E_v}^{E_c} N_{it} D(T)\delta(E_m - E)dE = qAN_{it}(E_m)D = I_{E_m} \tag{3.33}$$

where I_{E_m} is the current contribution from the level at position E_m. Thus, the density of interface states is simply (renaming E_m to E for simplicity)

$$N_{it}(E) = \frac{I_E}{qAD} \qquad (\text{eV}^{-1}\ \text{cm}^{-2}) \tag{3.34}$$

D can be calculated numerically for any number of assumed temperature-dependence of σ_n, and it is found to be approximately 5×10^{-4} eV/s in all cases.

However, in order to plot N_{it} versus position in the band gap, temperature must first be translated into emission from a certain trap position. The maximum of $P(E, T)$ as a function of E is found by evaluating,

$$\frac{\partial P(E = E_m, T)}{\partial E} = 0$$

where P has a maximum at E_m. Regardless of the T-dependence of σ_n, since the differentiation is with respect to energy, the result is

$$\frac{T}{\beta} \int_{T_0}^{T} \frac{e_n}{T} dT = 1$$

At this point, an assumption must be made about the T-dependence of σ_n. However, with a physically reasonable T-dependence the solution of the above equation yields a linear relationship for $\Delta E(T)$. The difference between assuming a T-independent $\sigma_n$and e.g. $\sigma_n \propto T^{-2}$ can lead to a difference in the position of N_{it} on the energy axis of about 0.2 eV for the deepest states (0.6-0.7 eV at close to room temperature), while this distortion decreases to about 0.05 eV for shallow states at low temperature. Using Simmons' convenient original assumption of $\sigma_n \approx (4 \times 10^{-12}\ \text{cm}^2\text{K}^2) \times T^{-2}$, corresponding to $\nu \equiv \gamma T^2 \sigma_n = 10^{10}$ 1/s and $\sigma_n = 5 \times 10^{-17}$ cm^2 at RT, the energy vs. T-relationship becomes

$$\Delta E(T) = T \times 10^{-4}(1.92 \log_{10}(\nu/\beta) + 3.2)\ \text{eV/K} - 0.0155\ \text{eV}$$

3.3.2 Extracting the total number of traps

While it is somewhat complicated to extract *spectroscopic* information from eq. (3.29), the extraction of the total number of trapped electrons is very simple in contrast. The measured current is

$$I = -qA\frac{dn_t}{dt} = -qA\beta\frac{dn_t}{dT} \tag{3.35}$$

The number of single-electron trapping levels which have emitted electrons between T_0 and T is

$$N_t = n_t(T) - n_t(T_0) = -\frac{1}{qA\beta}\int_{T_0}^{T} I(T')dT' \tag{3.36}$$

The number of trapped electrons can then be compared to the accumulation charge, Q_{acc}, in the capacitor during the charging, which corresponds to the number of charge carriers available for trapping and subsequent emission and detection at a given bias,

$$Q_{acc} = (V - V_{FB})C_{ox} = \epsilon_{ox}E \tag{3.37}$$

where V_{FB} is the flatband voltage, C_{ox} is the oxide capacitance, ϵ_{ox} is the permittivity of the oxide and E is the electric field across the oxide. If the amount of emitted charge, qAN_t, at a given charging bias or field is equal to Q_{acc}, then the extracted number of trapped electrons is simply limited by the availability of electrons in the accumulation region and the number of trapping levels will be underestimated. A higher bias is then required to extract the true number of trapping levels.

3.4 Secondary Ion Mass Spectrometry

Secondary ion mass spectrometry (SIMS) is a technique for chemical characterization of solid materials, e.g. detection of impurities, by exposing the sample to an ion beam and detecting the sputtered so-called secondary ions from the sample due to collisions with the ion beam (primary ions). However, SIMS was not used for analasis in this work, but rather for proton focused beam bombardment to study the generation and behaviour of intrinsic point defects and extended defects in 4H-SiC, with a particular emphasis on the diffusion properties of said defects. An overview of the Cameca IMS 7f instrument is included in Fig. 3.9.

3.5 Ion Implantation

A 1 MV ion implanter from National Electrostatics Corp. (NEC) was employed for implantation of Si-ions, in order to generate intrinsic point defects for subsequent study using electrical characterization methods. Fig. 3.10 contains a schematic illustration of the implanter.

The ions are extracted as negative ions, but are subsequently stripped of electrons and only those with the selected charge to mass ratio are allowed to reach the target sample, thus specifying the implantation dose.

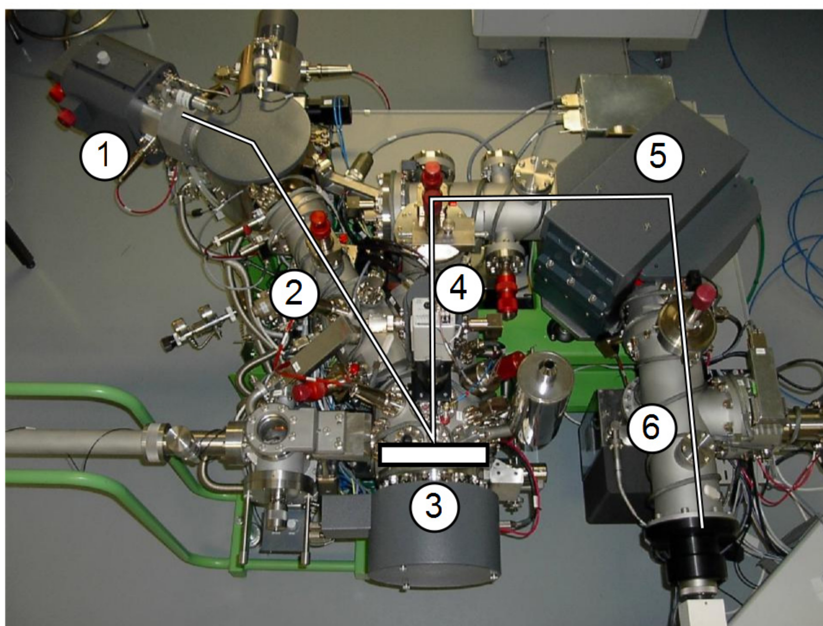

Figure 3.9: Overview of the Cameca IMS 7f SIMS instrument at UiO-MiNaLab. The DUO source which is normally used with oxygen for sputtering and analysis was used as a hydrogen ion source for proton irradiation. (1) DUO ion source, (2) primary ion pathway and electromagnetic lenses, (3) sample holder, (4) pathway for sputtered secondary ions and electrostatic analyzer, (5) magnet analyzer and (6) detectors.

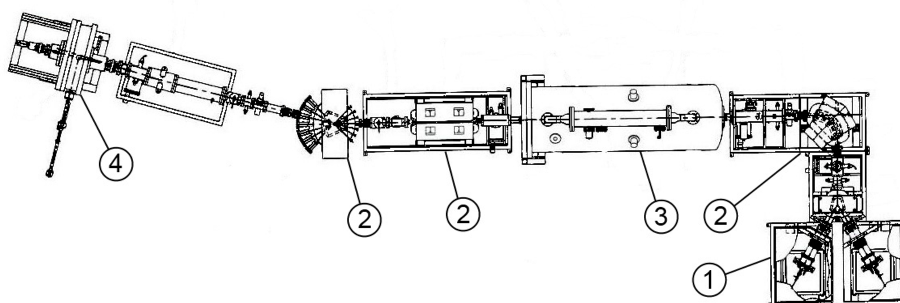

Figure 3.10: Schematic overview of the NEC 1 MV pelletron ion implanter at UiO-MiNaLab. The implanter uses solid sources, and makes it possible to implant or irradiate using a large variety of elements at energies of several MeVs (depending on the selected charge state of the stripped ions). (1) Sources and 35 kV extraction potential (negative ions), (2) magnets and electromagnetic lenses, (3) SF_6 filled pelletron pressure tank with up to 1 MV terminal potential and (4) multi-sample stage and load-lock.

Chapter 4

Previous knowledge and present contributions

4.1 Interface defects in SiO_2 / 4H–SiC structures

SiC is one of the few semiconductors with a useful native oxide, SiO_2 just as in the case of Si, which is one of the strong arguments for using SiC in the first place since this makes the "paradigm" shift from Si to SiC processing a much smaller issue than it otherwise could be for device manufacture. The process of thermal oxidation of SiC and the challenges related to SiO_2 / 4H-SiC structures will be outlined in this section.

4.1.1 Thermal oxidation of 4H-SiC

The thermal oxidation of SiC occurs according to the following reaction (with only CO included as the exhaust gas),

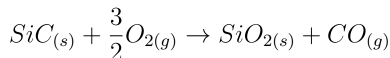

$$SiC_{(s)} + \frac{3}{2}O_{2(g)} \rightarrow SiO_{2(s)} + CO_{(g)}$$

where the input is O_2 and CO is released. As in the case of silicon, the oxidation takes place at the interface to the semiconductor. Thus, O_2 must diffuse through previously formed SiO_2 to reach virgin SiC material, and CO and CO_2 must diffuse through SiO_2 in order to escape as exhaust. The oxidation rate is much slower than in the case of silicon, and also very highly dependent on the crystal orientation and face. On hexagonal (000$\pm$1) SiC the oxidation rate is much slower on the Si-face than on the C-face. The Deal-Grove model [25] does not strictly speaking correctly describe the oxidation of SiC since it does not take the out-diffusion of CO into account, however modified theories can be derived [26] which end up taking the same general form,

$$X_{ox}^2 + AX_{ox} = B(t + \tau)$$

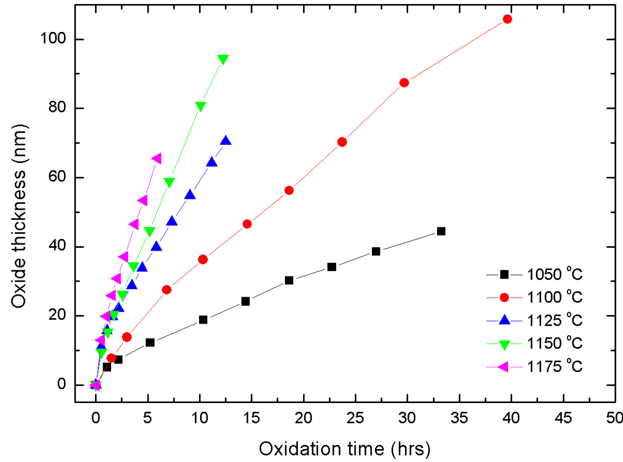

Figure 4.1: Oxide thickness vs. time for (0001) 4H-SiC at temperatures in the range 1050 - 1175 °C.

where X_{ox} is the oxide thickness, the coefficients A and B are referred to in terms of the so-called linear rate constant B/A and the parabolic rate coefficient B. τ represents an effective oxidation time which takes into account the initial oxide thickness at $t = 0$, which can be ignored in the case of SiC unless extremely thin oxides are studied. The oxide thickness vs. time on (0001) 4H-SiC, i.e. on the Si-face, at various temperatures is presented in Fig. 4.1. The oxidation was performed in a tube furnace with flowing O_2. Only this crystal orientation has been studied in this work.

4.1.2 Interface defects

Due to its large bandgap, large breakdown field and reasonably large bulk mobility (800 cm^2/Vs in the case of the 4H polytype) SiC / MOS-devices should perform very well under conditions of high power, voltage and temperature. However, the expected potential of these devices has not yet been fully realized, due to an unexpectedly low mobility (lower than about 20 cm^2/Vs) in the electrically conductive channel below the gate electrode. The low mobility is due to electronic states in the bandgap originating from electrically active defects at the interface, in the SiO_2 layer and possibly also in the channel / SiC bulk material itself below the interface. The defects themselves are structural imperfections in these areas, and a schematic outline of the density of interface states across the bandgap of 4H-SiC is shown in Fig. 4.2.

As can be seen in the figure, the density of states has distinctive peaks and valleys. In addition, the density is higher close to the conduction band than the valence band, due to a feature labeled “NIT” reaching values up to 10^{14} eV^{-1} cm^{-2} or even higher at the band edge in the case of standard dry oxidation of the Si-face. This work mainly concerns n-type 4H-SiC, i.e. the nature of the feature labeled D4 and the high-density feature related to NITs. The other features in the spectrum, as well as methods of passivating these, will only be given a cursory review.

The ground-breaking works of Afanas’ev et al. [28, 29] resulted in the so-called “carbon-cluster model” of the SiO_2 / SiC interface. This model separates the total density of interface

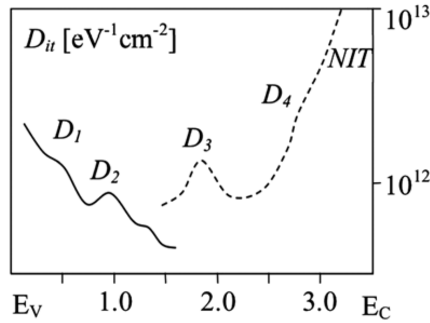

Figure 4.2: Schematic illutration of the density of interface states in the SiC bandgap of SiO_2 / 4H-SiC devices. From [27].

states in the bandgap of 3C-, 6H- and 4H-SiC MOS devices into three contributions,

- Deep states near the middle of the SiC band-gap due to graphite-like clusters of unknown size at the interface
- States near the SiC valence band edge due to sp^2-bonded carbon clusters of unknown size at the interface
- A defect in the SiO_2 layer, but near the interface, resulting in a level located at 2.8 eV below the SiO_2 conduction band edge, corresponding to E_C - 0.1 eV in 4H-SiC, and therefore slightly above E_C in 6H-SiC and far above E_C in the case of 3C-SiC

Only a very small contribution to the D_{it} was found to be due to dangling bonds at the interface. The valence bands in the SiC polytypes are very closely aligned, so the electrically active defect causing the NITs in the oxide appear at different positions relative to E_C in the various polytypes. Since 4H-SiC has the largest bandgap, these defects are also the most detrimental to the mobility in this polytype. The level at E_C - 2.8 eV in the SiO_2 bandgap was suggested to be due to oxygen deficiencies in the SiO_2. The NITs should exist some 1-2 nm from the interface and into the oxide. The D_{it} was found to be largest at the C-face, intermediate at the a-face and smallest at the Si-face, which strongly suggested that the density of carbon on the oxidized face is related to the formation of some kind of detrimental carbon clusters at the interface during oxidation. The source of the carbon clusters is the SiC material itself, which is partially consumed during oxidation and therefore releases carbon. This is part of the motivation for studying alternative dielectrics for SiC MOS-devices, such as Al_2O_3 (see ref. [30, 31] and references therein), along with the need for high-k dielectrics for very high-voltage devices where SiO_2 would undergo dielectric breakdown.

A very thorough study by Pippel et al. conclusively found that there are no large carbon clusters at the interface or in the oxide close to the semiconductor after dry thermal oxidation [32]. Thus, the NITs must be due to very small carbon clusters, such as carbon dimers, or native oxide traps. A study by Rudenko et al. [33] found spectroscopically, using TDRC, that NITs are composed of a combination of two kinds of traps, a fast trap with position E_C - 0.1 eV and a slower and broader distribution of traps with an almost continuous distribution of activation energies between 0.1 - 0.7 eV below E_C with a thermally activated capture

mechanism. The former level is very shallow in the bandgap and was argued to exist essentially at the interface, while the latter levels are at a similar energy position as the feature which is labeled D4 in Fig. 4.2 and is argued to be distributed in a O-Si-C transition layer.

Dimitrijev et al. discovered that a post-oxidation anneal in NO atmosphere reduces the density of slow interface states, while the same treatment in N_2O increases the density [34, 35]. This applies to both n- and p-type material, but is particularly effective on the latter. Results from Afanasév et al. indicated that the slow states which are reduced in density by the NO anneal are located in the oxide near the interface with SiC [36]. It was later discovered that a pre-oxidation nitrogen implantation, where the oxidation completely consumes the implanted layer, also substantially reduces the density of interface states near the conduction band edge, although in the same study the density of states near the valence band edge was reported to increase [37, 38]. However, the most effective seems to be to implant nitrogen followed by a wet oxidation in such a manner that the peak in nitrogen concentration ends up right at the interface, as reported by Poggi et al. [39]. A combined C-V and TDRC study by Pintilie et al. argued that the contributions from the various kinds of interface states — fast interface states (D_{it}), fast and slow near-interfacial oxide states N_{ox}^{fast} and N_{ox}^{slow} — can be separated, and found that in particular N_{ox}^{fast} was reduced in concentration by the pre-oxidation N-implantation procedure (paper VI).

An ab inito study by Deak et al. [27] summarizes the experimental and theoretical evidence for carbon clusters and argues that their size must be small; further electrical data suggest that the NITs are acceptor-like states which are distributed in physical position from the interface and some distance into the oxide. The study goes on to show that *at the interface* the $(Ci)_C$ type of carbon dimer, which is a so-called split interstitial where an interstitial carbon shares a carbon site with a lattice carbon atom, is amphoteric and gives rise to deep levels which fit well with the deep D_2 and D_3 features. In addition, the $C_i = C_i$ carbon dimer has a fairly shallow donor level near the valence band in SiC, which lines up well with the D_1 feature. As for defects inside the oxide, however, it is found that oxygen excess, interstitial oxygen and silicon vacancies can all be exluded, and oxygen deficiency defects can be exluded for stability reasons, contrary to the suggestions in ref. [28].

On the other hand, silicon interstitials are expected to appear in the oxide, they should be stable and have an acceptor level rougly corresponding to the broad signature typically observed by TDRC at around 130 K and which lines up with the D4 feature. This may correspond to the broad level at about E_C - 0.7 eV in TDRC measurements.

Another type of C-dimer, $C_o = C_o$, can be formed at the interface during oxidation and grow into the oxide. This is found to be the only stable C-dimer in the oxide, and both C-atoms are at oxygen-positions, hence the carbon atoms are bonded only to Si-atoms. Recently, in another theoretical study Shen and Pantelides [40] concluded that a major contributor to the low channel mobility is so-called C di-interstitials which form during oxidation from the injected C_I as established by observing oxidation-enhanced annealing (cf. section 4.3). This is supported by experimental results [41] which conclude that a record high channel mobility can be achieved by using Al_2O_3 as the dielectric and simultaneously carefully controlling the thickness of the inevitable interfacial layer of SiO_2.

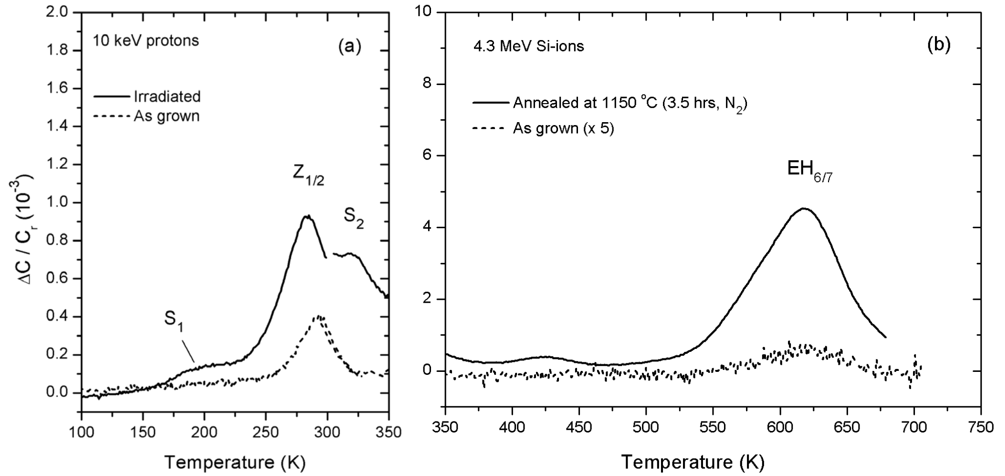

Figure 4.3: DLTS spectra of the (640 ms)$^{-1}$ lock-in rate window in the temperature range 100-750 K, illustrating (a) the S_1/S_2, $Z_{1/2}$ after 10 keV proton irradiation and (b) $EH_{6/7}$ after 4.3 MeV Si-implantation.

4.2 Prominent intrinsic defect centers

The most prominent trapping centers in as-grown, electron- and proton-irradiated and Si-implanted 4H-SiC, will be described in this section. Only deep levels in the upper half of the bandgap will be considered, since these have been the main subject of the authors studies. DLTS spectra in the temperature range 100-750 K is plotted in Fig. 4.3 with labels for the S_1/S_2, $Z_{1/2}$, and $EH_{6/7}$ levels.

4.2.1 $Z_{1/2}$

The $Z_{1/2}$ center is, together with $EH_{6/7}$, the only deep level found in significant concentration in n-type as-grown 4H-SiC [16–18, 42]. The concentrations of these two centers are both inversely correlated with the minority carrier lifetime, as well as the nitrogen donor concentration, and for a while it was uncertain which defect center was the actual culprit in limiting the lifetime [43, 44]. Klein et al. performed DLTS and lifetime measurements on a series of 4H-SiC epitaxial layers of increasing thickness, and observed that the $Z_{1/2}$ concentration was very strongly correlated with the inverse effective lifetime [45]. Moreover, this center has large, almost equal capture cross sections for both electrons and holes in the low 10^{-14} cm^2 range making it an efficient recombination center. In contrast, the concentration of the $EH_{6/7}$ center showed no such correlation. The lifetime is no longer limited by the $Z_{1/2}$ center below a concentration of $1 - 2 \times 10^{13}$cm^{-3} [46], and it has been speculated that structural defects or surface recombination may dominate in this regime.

The $Z_{1/2}$ center actually gives rise to two different centers and each yields two different DLTS peaks corresponding to two charge state transitions with closely spaced energy levels [47]. Due to their negative-U property only a direct transition from the neutral to the doubly

negatively charged states are usually observed using DLTS. However, Hemmingsson et al. [47] found that by optically emptying those traps which have captured and frozen-out two electrons before each DLTS filling pulse, and by employing a short enough filling pulse to prevent the capture of two electrons, the middle charge state may also be observed.

There is broad agreement that the $Z_{1/2}$ defect is intrinsic in nature, but its microscopic structure is still controversial. Among the speculations on its origin so far are a divacancy, $V_C V_{Si}$ [18], a silicon antisite - silicon vacancy complex, $Si_C V_{Si}$ [43], a carbon interstitial with nitrogen participation [44, 48] and a silicon-carbon antisite pair, $Si_C C_{Si}$ [43]. The involvement of nitrogen was ruled out by performing low energy electron radiation on both nitrogen and phosphorous doped material [49]. Hypotheses involving silicon vacancies or interstitials are also falsified by low energy electron irradiation since silicon vacancies and interstitials would not be generated in this case, although the antisite defects could still be generated to some extent depending on the equilibrium concentration of silicon vacancies in the material [11].

Altogether, the evidence for the involvement of carbon in $Z_{1/2}$ is by now plentifold. In fact, a majority of the implantation and radiation induced defects in n-type 4H-SiC appear to involve defects on the carbon sublattice [11], perhaps due to the lower energy required for generating carbon Frenkel pairs. The main evidence for the involvement of carbon and not silicon comes from experiments with low energy electron irradation [12, 49, 50]. It has been argued that Z_1/Z_2 may be carbon vacancy related defects situated at the two different sublattices [11, 47], due to their close energy levels and often 1:1 correspondence in electron irradiation experiments. The $Z_{1/2}$ defect is also suppressed by epitaxial growth under carbon-rich conditions, i.e., $Z_{1/2}$ decreases with increasing C/Si-ratio), favouring either Si_C or V_C [43, 51]. A recent ab initio study by Hornos et al. [52] found that the properties of V_C are very similar to those of $Z_{1/2}$ and $EH_{6/7}$.

Under normal conditions, $Z_{1/2}$ has extremely high thermal stability, persisting up to 2000 °C after partially annealing out in a multi-step process as the temperature increases, indicating that it reacts with other defects which become mobile or dissociates at certain temperatures [20]. Alfieri et al. estimated that the dissociation energy of $Z_{1/2}$ itself is about 8 eV. An argument in favor of the carbon vacancy hypothesis is that the $Z_{1/2}$ level — as well as the $EH_{6/7}$ level and several other levels — anneals out rapidly during a standard dry, thermal oxidation in the temperature range 1050 - 1300 °C (which correlates with the introduction of the so-called HK0 level in the bottom half of the bandgap) [53, 54] (papers I-III). Interstitials are expected to diffuse faster than vacancies, hence this indicates that $Z_{1/2}$ incorporates the carbon vacancy which is then annihilated in a reaction with in-diffusing interstitials during the oxidation. This phenomenon is described in more detail in section 4.3. Enhanced annealing of $Z_{1/2}$ is also observed after carbon implantation, and it was also here argued that carbon interstitials migrate from the carbon rich surface region towards the bulk and reacting with $Z_{1/2}$, causing the putative carbon vacancy component of $Z_{1/2}$ to annihilate with the migrating interstitials [55].

On the other hand, $Z_{1/2}$, $EH_{6/7}$ and other defects in n-type (0001) 4H-SiC have been observed long lateral distances — in some cases on the order of millimeters (paper V and section 4.4) — from the irradiated spot after irradation using a focused electron or proton beam [12, 56, 57]. This indicates that these defects are generated from a precursor which becomes highly mobile during irradiation, possibly due to the generation of significant amounts of minority carriers and subsequent recombination-enhanced / electronically stimulated migration. The precursor

defect(s) is then believed to migrate out from the irradiated spot and leave behind $Z_{1/2}$ and other defects in a radial lateral distribution. During such experiments employing a low energy (< 300 keV) electron beam, Steeds et al. [12] observed that photoluminscence-lines corresponding to silicon vacancies stayed within the irradiated area, while interstitial-related centres were observed to migrate outside the directly irradiated area. This, coupled with the low energy which should only generate damage on the C-sublattice, points to the carbon vacancies as the migrating defect, in contradiction to that concluded in the context of oxidation enhanced annealing of $Z_{1/2}$.

However, in paper V and section 4.4 the observation of S_1/S_2, $Z_{1/2}$and $EH_{6/7}$ at distances on the order of mm's from the irradiated area is discussed in terms of the previously established long range migration of extended defects rather than point defects.

4.2.2 $EH_{6,7}$

The $EH_{6/7}$ levels, like the $Z_{1/2}$ level, are typically found in as-grown material at concentrations of around $10^{12} - 10^{13}$ cm^{-3}, which further increases greatly due to electron and proton irradiation, and ion implantation [16–18]. They are positioned quite deeply in the band gap, about 1.65 eV below the conduction band edge, and have large electron capture cross sections estimated to approx. $10^{-13} - 10^{-14}$ cm^2 extrapolated from an Arrhenius plot, and larger than 5×10^{-15} cm^2 when measured by varying the filling pulse width during DLTS measurements [16]. The $EH_{6/7}$ levels have been argued to be acceptor-like due to the lack of observed temperature shift of the DLTS peak with different applied electric field [17,18], and a recent study has unambiguously shown that $Z_{1/2}$ is a double acceptor level while $EH_{6/7}$, or EH_7, is donor-like [58].

The DLTS peak is rather broad and consists of two closely overlapping levels, EH_6 and EH_7. Because of this, and since they usually appear together, these overlapping levels are sometimes treated together, despite having different behavior, e.g. mainly EH_7 is generated by low-energy (80-300 keV) electron irradiation, while both are generated at higher energies, indicating that EH_7 is most likely due to a elementary carbon-related point defect while EH_6 is due to a more complex cluster [11]. In fact, the EH_7 and $Z_{1/2}$ levels are now considered to be different charge states of the carbon vacancy, from a comparison of the energy levels of V_C, $Z_{1/2}$ and EH_7, and the fact that both V_C and $Z_{1/2}$ exhibit negative-U behavior [58].

The evidence for the involvement of carbon in this level is compelling and mostly based on the same arguments as for $Z_{1/2}$; its formation is suppressed by increasing the C/Si ratio during CVD growth [44], EH_7 is observed after electron irradiation at energies below the threshold for damaging the Si-sublattice [11, 50] and both EH_6 and EH_7 exhibit highly enhanced annealing following either carbon implantation [55] or thermal oxidation [53,54,59] (paper III). These results indeed support the involvement of V_C in the $EH_{6/7}$ level.

Some studies have also reported that the concentration of $Z_{1/2}$ and $EH_{6/7}$ *increases* with increasing C/Si ratio, and also with increasing nitrogen content [48,60], although most growth studies seem to agree on the opposite dependence on the C/Si ratio.

As already mentioned, the $EH_{6/7}$ levels are generated in similar concentrations (about 1:2) as the $Z_{1/2}$ center by radiation, and their annealing behavior is also very similar [11,20]. Both

have very high thermal stabilities, persisting up to 2000 °C, and anneal out in multiple stages. The final dissociation energy for $EH_{6/7}$ has been estimated as at least 7.5 eV [20].

Although the $EH_{6/7}$ levels are known to be intrinsic, they have also been observed to exhibit electric field assisted annealing following MeV ion implantation with either N or C, where the annealing changes character depending on the implanted species [61]. This manifests itself as an instability in the EH_7 level when subjected to reverse bias at 700 K, e.g. during high-temperature DLTS measurements. EH_7 irreversibly decreases in N-implanted and increases in C-implanted material, while little change is observed for the EH_6 level. The $EH_{6/7}$ levels have also been observed long distances from a point irradiation performed with protons, just like the $Z_{1/2}$ and S_1/S_2 levels (paper IV-V, section 4.4).

4.2.3 S_1/S_2

The S_1/S_2 levels consist of the S_1 level at E_C - 0.45 eV and the S_2 level at E_C - 0.71 eV, with capture cross sections 8×10^{-17} and 3×10^{-15} cm^2, respectively, measured by pulse width variation [16, 19, 20, 62]. David et al. found that they appear in a nearly 1:1 relationship following both low and high energy electron and proton irradiation, after a post-irradiation anneal at about 200 °C, both with formation energies established as about 1 eV [19]. Their decaying amplitudes also closely match during annealing, with an activation energy for the decay $E_a = 1.8$ eV and a prefactor $c_0 = 1 \times 10^{11}$ s^{-1}. No electric field dependence on the DLTS peak positions have been found, possibly indicating that the levels are acceptor-like. Due to the 1:1 correspondance both in as-irradiated material and after annealing, David et al. argued that these levels most likely correspond to different charge states of the same defect center. This is further supported by the much smaller electron capture cross section for S_1, which could indicate that the center is acceptor-like and capable of capturing two electrons since a capture of the first electron leads to a negatively charged center and therefore a much lower capture rate of the second electron due to coloumbic repulsion.

It has also been shown that these levels appear after annealing at room temperature for several months, and that the annealing is accelerated both by an applied reverse bias [19] and recombination enhanced during hole-injection either through a p^+/n-junction or by illumination with above-band gap light [63]. The recombination enhanced annealing is not entirely athermal, as the annealing rate decreased with decreasing temperature below room temperature. The fact that both the S_1 and S_2 levels display these relatively rare properties was regarded as further evidence that they do correspond to different charge states of the same defect center. The levels start to anneal out at temperatures above 250 °C.

Upon performing low-energy focused beam electron irradiation, Alfieri et al. observed the S_1/S_2 levels, along with $Z_{1/2}$, up to distances of several hundred μm away from the directly irradiated area [57]. These levels have also been observed at distances on the order of 1 mm away from the directly irradiated area after low energy focused beam proton irradiation, as explained in detail in papers IV-V and section 4.4.

4.3 Oxidation-enhanced annealing of point defects

As briefly described in section 4.2, the S_1/S_2, $Z_{1/2}$ and $EH_{6/7}$ levels all undergo enhanced annealing during heat treatments in an oxidizing ambient, i.e. thermal oxidation, as discovered

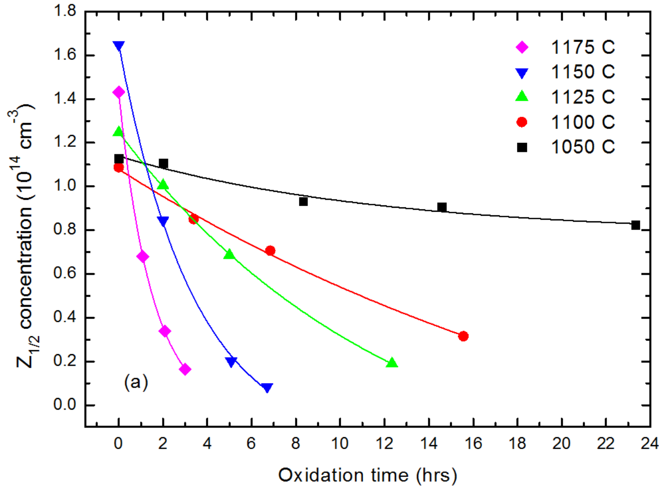

Figure 4.4: The first-order decay of $Z_{1/2}$ during thermal oxidation after 4.3 MeV Si-implantation, with the concentration recorded at a depth of 0.8 μm from the surface.

by Hiyoshi and Kimoto [53, 59]. A new level, referred to as HK0 and located at E_V + 0.78 eV, is generated in the lower half of the band gap during the oxidation, measured on p-type material. The thermal oxidation leads to an increase in minority carrier recombination lifetime of about a factor 5, while a further anneal in Ar at 1500 °C completely removes HK0 and yields a total increase in the lifetime of a factor 7. Hiyoshi et al. argued that the responsible mechanism was injection of interstitial carbon from the oxidizing interface, which migrates to and annihilates on vacancies. Hence, this hypothesis implies that the annealing defects contain V_C, as was also argued by Storasta et al. to explain the enhanced annealing of these defect centers in C-implanted material [55].

The temperature at which the $Z_{1/2}$ level starts to disappear decreases from 2000 °C [20] to temperatures yielding a reasonable oxidation rate, e.g. above 1100 °C on (0001)-face 4H-SiC (paper II), as a result of the oxidation. Thermal oxidation as a procedure for annealing out the $Z_{1/2}$ and $EH_{6/7}$ centers has been shown to be more efficient close to the surface than deeper in the material, which is a natural consequence of the higher concentration of C_I due to the migration of this defect from the interface (papers I and III). In paper II, 4.3 MeV Si-ions were implanted to a dose of 3×10^8 cm^{-2} in the profile peak, generating $Z_{1/2}$ to a concentration of about 6×10^{14} cm^{-3}, and subsequently annealing was performed in N_2 and O_2 at temperatures in the range 1050 - 1175 °C. $Z_{1/2}$ was observed to decay in a first-order reaction with an activation energy of 5.4 ± 0.3 eV as shown in Fig. 4.4. A first order decay is due to an essentially time-independent concentration of C_I in the peak region of $Z_{1/2}$, which enables the extraction of the normalized concentration of C_I.

The concentration of the $Z_{1/2}$ level and C_I can be simulated numerically by modelling the diffusion-reaction process as a set of two equations like eq. (2.10) for $[Z_{1/2}]$ and $[C_I]$ vs. oxidation time and distance from the oxidizing interface, with $Z_{1/2}$ considered immobile and the diffusivity of the carbon interstials denoted $D_{C_i} \equiv D$.

The results of two such simulations performed at 1100 and 1175 °C is shown compared to the experimental data in Fig. 4.5. The simulations show that the diffusivity of C_I is within

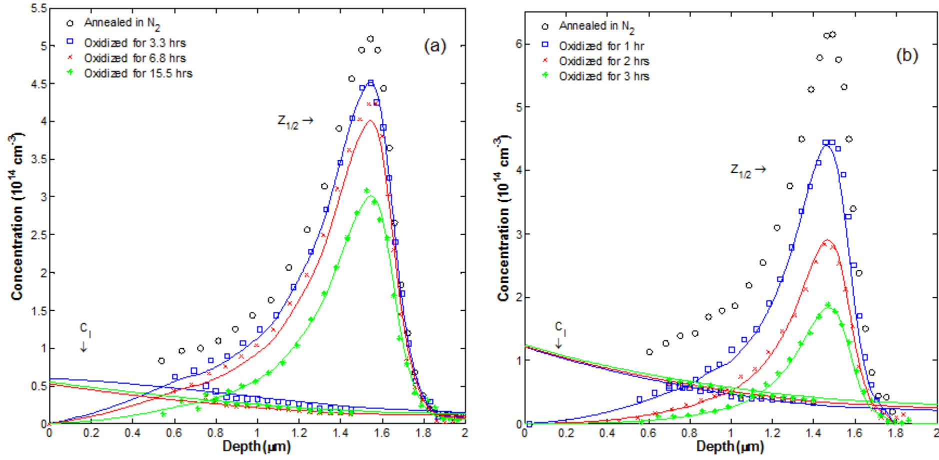

Figure 4.5: Simulated (lines) compared with experimentally measured (symbols) concentration vs. depth profiles after implantation and subsequent annealing at (a) 1100 °C and (b) 1175 °C. Clearly the solutions for C_I satisfy the demand that $[C_I]$ must be time-independent within the peak-region of the $Z_{1/2}$-distribution.

$10^{-12} - 10^{-11}$ cm^2/s, and the generation rate is within $10^{13} - 10^{14}$ cm^{-3}/ s in the investigated temperature range. The activation energy of the oxidation rate (E_a^{ox}) has been independently measured to 3.1 eV, which is corroborated by previous reports in the litterature [26]. Since the oxidizing interface directly provides the source of the injected carbon the generation rate may be expected to have the same activation energy (E_a^g), or possibly higher if other sources of carbon exist such as dissociation of carbon complexes at higher temperatures. Although no conclusive result could be obtained on the magnitude of E_a^g and E_a^D (for the diffusivity), as described in paper II, indeed the simulations show that the solution with E_a^g = 3.3 eV and E_a^D = 3 eV yields excellent agreement with the measured depth distributions of both $Z_{1/2}$ and C_I. This combined value of slightly above 6 eV for the entire diffusion-reaction process agrees reasonably well with the value of 5.4 ± 0.3 eV found experimentally.

4.4 Spatially resolved long range lateral migration of intrinsic defects[1]

The observations of long range lateral migration in 4H-SiC, i.e. in the basal plane, of intrinsic defects following proton irradiation using a focused beam, as described in papers IV and V, will be extended in this section to also include irradiation at the bottom of a pre-sputtered crater. As will be shown, this leads to a narrow and defect rich layer where the defects migrate extremely long lateral distances but are confined within a 1 μm thick layer. The directly observed point defects are the S_1/S_2 and $Z_{1/2}$ levels, although the migration phenomenon is actually ascribed to the recombination-enhanced motion of dislocations, as argued below and in paper V.

[1] Lasse Vines contributed significantly to the work described in this chapter, cf. paper V. Augustinas Galeckas is gratefully acknowledged for illuminating discussions and assistance with the laser irradiation.

4.4.1 Introduction

It has previously been found that some defects can migrate distances of several hundreds of micrometers during electron irradiation, as studied by photoluminescence (PL) [12, 56] and deep level transient spectroscopy (DLTS) [57]. Specifically, the interstitials migrate long distances, whereas the vacancies were found to largely remain confined within the directly irradiated volume. Since the defects giving rise to the S_1/S_2 and $Z_{1/2}$ levels were observed long distances from the irradiated area, it was concluded that C_I is involved in the formation of these defect centers. This may be supported by a first-principles study of the production of antisite pairs in 4H-SiC, which found that C_I (but not the carbon vacancy, V_C) can act as a catalyst in the production of antisite pairs during ionizing conditions, such as during irradiation [64].

In these studies [12, 57] it was suggested that the carbon interstitials are able to migrate long distances through a diffusion process for defects driven by successive changes in charge state, known as electronically stimulated migration (ESM) or the Bourgoin-Corbett mechanism [5]. In special cases the defect may not encounter any barriers at all in this diffusion process, and the process is then completely athermal (it will occur even at 0 K). Several examples of defects in other materials which are thought to migrate by this mechanism can be mentioned, for example the silicon self-interstitial [65]. This mechanism has also been proposed to play a key role in the formation of the substitutional boron - interstitial oxygen dimer (B_SO_{2i}) complex in silicon, which is responsible for light induced degradation in silicon solar cells [66, 67], although this hypothesis has recently been refuted [68].

In paper IV-V the samples were irradiated directly at the surface. The projected range of 10 keV protons in SiC is about 100 nm, which means that in this case the defects are generated very close to the surface. In contrast, bulk-like defect migration is studied in this chapter by irradiating with a focused beam of protons in the bottom of a sputtered crater. We report on the defect distribution as a function of both lateral and vertical distance from the irradiated areas. Very long range lateral migration is observed at room temperature (RT), extending to distances of several millimeters. Vertically the defects distribute only in comparatively thin layer of about 1μm thickness. The results are fitted to the diffusion equation, and effective lateral diffusivities are extracted for both the $Z_{1/2}$ and the S_2 defect center.

4.4.2 Experiment

Schottky barrier diodes (SBD) were formed on n-type nitrogen doped (0001) 4H-SiC (purchased from Cree, Inc.) with a 10 μm thick epitaxial layer on the Si-face by e-beam deposition of 100 nm thick circular Ni contacts with diameters of 400 μm. The effective carrier concentration in the epi-layer was about 3×10^{15} cm^{-3}, while the substrate doping was about 10^{18} cm^{-3}. The concentrations of point defects with deep trapping levels were monitored before and after the irradiations by DLTS. The measurements were made using the experimental setups described in section 3.2.3. Selected measurements were performed at high energy resolution using the GS4 weighting function [69].

In preparation for the irradiation, the crater was first sputtered using a 10 keV O_2 beam. The resulting crater had dimensions 100^2 μm^2 and a depth of 1.7 μm. The SBDs were protected

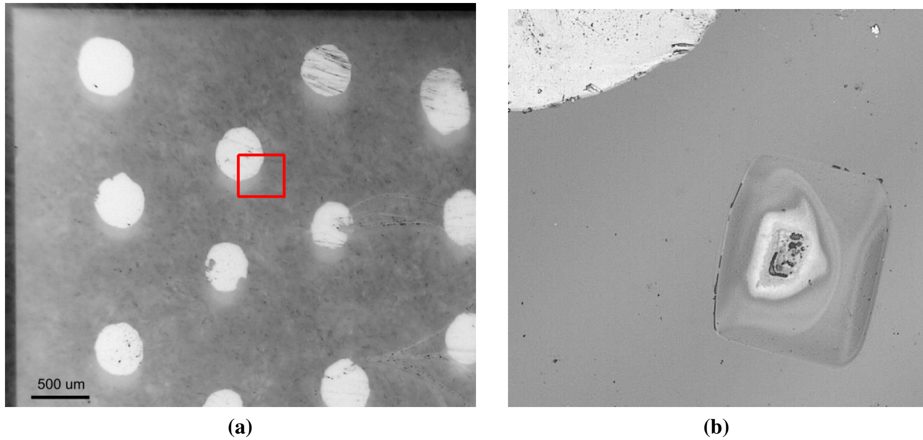

(a) **(b)**

Figure 4.6: (a) Micrograph showing the layout of SBDs in part of the sample. (b) Close-up of the area indicated by the red rectangle in (a), showing the irradiated crater and the closest contact. The crater has approx. 100 μm long edges.

by a 1.5 μm thick layer of photoresist during the sputtering and irradiation. This layer is thick enough to act as a protective mask since the projected range of 10 keV protons in photoresist is 0.25 μm. However, several separate test cases showed that the layer of photoresist is not strictly necessary since the Schottky diodes are not damaged by the sputtering and irradiation process, i.e. their electrical behavior remained identical prior to and subsequent to the sputtering and irradiation. The irradiation itself was performed with a beam diameter of 75-100 μm. The proton beam current was 10 nA and the irradiation time was 1 hr.

4.4.3 Results

A micrograph of the sputtered crater prior to the proton irradiation is shown in Fig. 4.6(a), while the crater subsequent to the irradiation is shown in Fig. 4.6(b). The irradiated area can be distinguished in the micrograph from the discoloration due to damage and strain in the irradiated region.

Fig. 4.7(a) shows the DLTS spectra measured before and after the irradiation was performed, probing the material to depths 1 - 3μm below the contacts, measured at -20 V reverse bias and pulsing to 0 V. The amplitude of the peak corresponding to the $Z_{1/2}$ level at 285 K increases by about a factor 3 due to the proton irradiation. No sign of the commonly observed S_1/S_2 levels were detected. In addition, the $Z_{1/2}$ peak is not as broad as is commonly observed directly after high-energy irradiation and prior to annealing [14], possibly indicating a more gentle defect formation in this case. A very pronounced and broad feature appeared in the temperature range 100 - 250 K in measurements on a few of the SBDs. This broad feature was highly unstable at room temperature and disappeared within a matter of hours. The broadness of the feature indicates a large number of closely spaced levels in the band gap resulting in overlapping DLTS peaks, suggesting that this feature may be due to structural defects such as dislocations. The so-called recombination-enhanced dislocation glide process in 4H-SiC leads to substantial dislocation migration velocities, with an activation energy

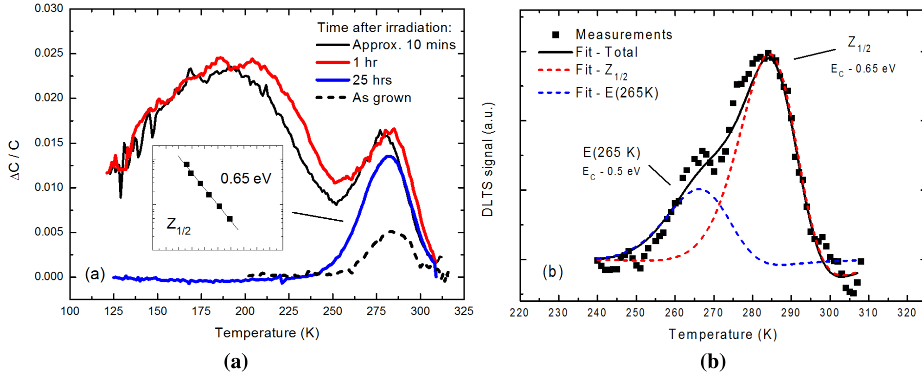

(a) (b)

Figure 4.7: (a) DLTS spectra showing the enlarged concentration of $Z_{1/2}$, including the overlapping E(265K) level on the low-temperature side, at a distance of 1.7 mm from the crater. The broad feature was thermally unstable at RT and disappeared within a few hours. Inset: Arrhenius plot yielding the band gap position of the peak. (b) The overlapping peak becomes detectable by using a high-resolution weighting function (GS4), and this is fitted with a band gap position of E_C - 0.5 eV.

of 0.27 eV, when excess electron-hole pairs are introduced by either electrical or optical injection [14, 70]. In other words, the structural defects leading to the broad feature in Fig. 4.7(a) may have been mobile and subsequently either annihilated or moved away from the SBDs in question. After about 1 day at RT the broad feature had disappeared from all SBDs. A shoulder on the low-temperature side of the $Z_{1/2}$ peak becomes detectable when using a high-resolution weighting function, Fig.4.7(b), and this is due to a level with a band gap position of E_C - 0.5 eV referred to as E(265K). It appears to be the same level as that detected previously in ion-implanted 4H-SiC [17] and it is suppressed in CVD layers grown under C-rich conditions [51]. The properties of the detected levels are summarized in Table 4.1.

Trapping center	E_C - E_t (eV)	σ_n (cm^2)
E(265K)	0.5	10^{-16}
$Z_{1/2}$	0.65	10^{-14}

Table 4.1: The band gap position and apparent capture cross section (σ_n) of the trapping centers which are detectable in Fig. 4.7.

The lateral distribution of defects following the irradiation was resolved by collecting DLTS spectra from all the 22 SBDs on the sample, which were all qualitatively similar to the one after 1 day at RT in Fig. 4.7, and plotting the concentration of $Z_{1/2}$ versus distance to the crater where the beam was positioned during the irradiation. This distribution is shown in Fig. 4.8, and the concentration of $Z_{1/2}$ strongly decreases with increasing distance to the beam. There is an increased concentration of $Z_{1/2}$ after the irradiation everywhere in the sample in this depth range (1-3 μm), even up to 5 mm laterally from the beam position. By performing a fitting routine on the DLTS peaks which include contributions from both $Z_{1/2}$ and E(265K) it is possible to separate their contributions, as shown in Fig. 4.9. They have quite similar lateral distributions, however the plot of the ratio of $Z_{1/2}$ to E(265K) in the inset indicates that the distribution for the E(265K) level decays slightly faster with distance than

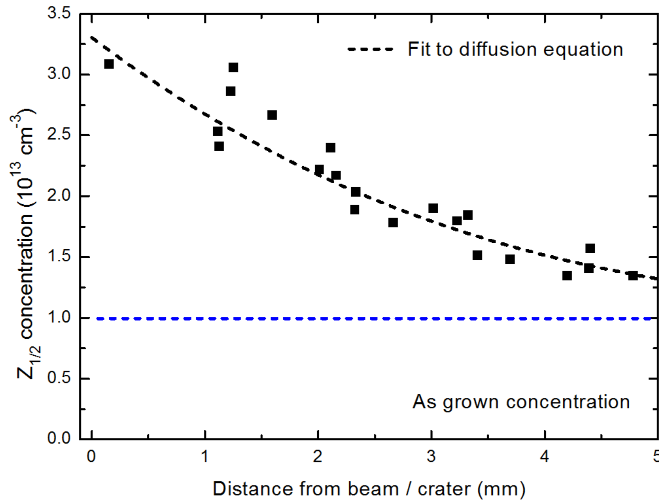

Figure 4.8: Distribution of the $Z_{1/2}$ concentration as a function of the distance from the beam position in the sputtered crater. The data have been fitted with the diffusion equation, eq. (2.1).

the distribution for $Z_{1/2}$ does.

The vertical distributions of $Z_{1/2}$, including a small overlapping contribution from E(265K), at several lateral positions from the beam have been found by performing DLTS depth profiling on the $Z_{1/2}$ peak. Fig. 4.10 clearly shows that the defects have formed at a depth of around 1.5 - 2.5 μm and spread out laterally to form a very thin layer in the sample compared with the lateral distances investigated here. This distribution is somewhat deeper than the crater depth of about 1.7 μm deep and also the peak in the distributions are apparently slightly offset to each other, but it is likely that there is some uncertainty in the depth, e.g. slight variations in the area of the SBDs.

An annealing procedure in steps of 100°C and 1 hr durations at temperatures up to 300°C in air and to 500°C in vacuum did not yield any changes in the concentrations of the defects, in strong contrast to the results from the irradiation directly at the surface of the material in paper V. The material was also exposed to UV light from a Hg-lamp with an output of approximately 40 W/cm^2 (emitting most prominently at 365 nm) and a pulsed 372 nm laser set to a peak power density of approximately 100 W/cm^2, yielding a maximum steady-state injection level of about 10^{15} electron-hole-pairs/cm^3, with no detectable change in the defect distribution.

4.4.4 Discussion

The concentration of the $Z_{1/2}$ level in Fig. 4.9 was used as input to fit the one-dimensional diffusion equation,

$$\frac{\partial N_t}{\partial t} = D_{\text{eff}} \frac{\partial^2 N_t}{\partial x^2}$$

where N_t is the concentration of the defect, D_{eff} is the effective diffusivity at RT and x is the distance from the beam. The fitting was accomplished by varying the effective diffusivity

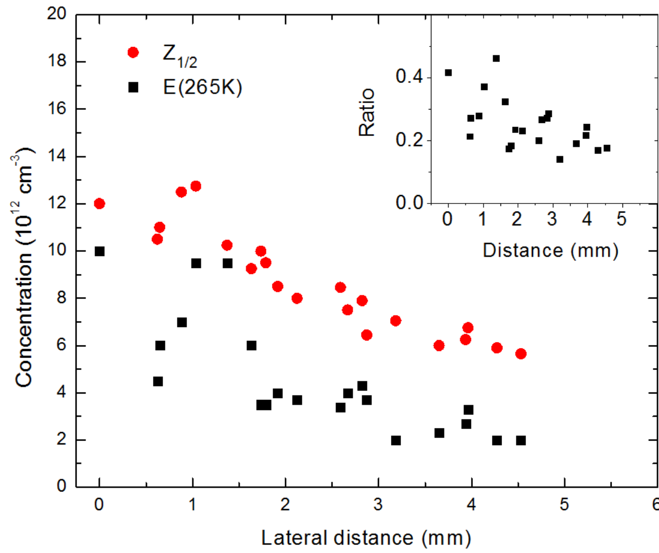

Figure 4.9: The lateral distributions of $Z_{1/2}$ and E(265K) have been separated by fitting the overlapping DLTS peaks and extracting the contributions from each defect level. Inset: The ratio of E(265K) to $Z_{1/2}$ vs. distance. Despite the significant scatter, largely in the concentration of E(265K), this indicates that the distribution of E(265K) decays faster with lateral distance than the $Z_{1/2}$ distribution.

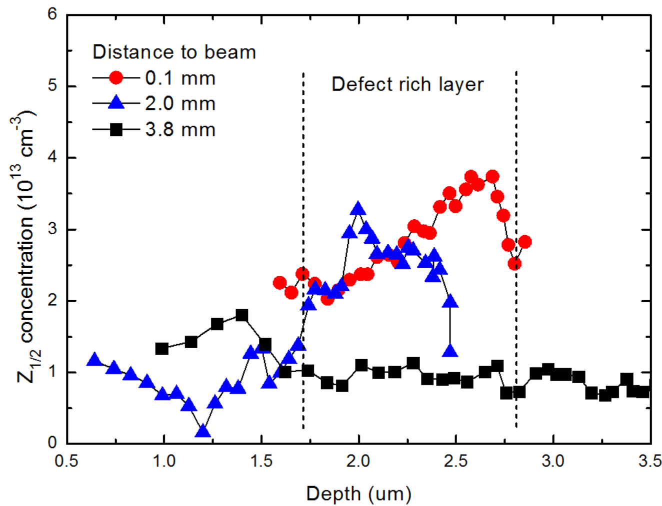

Figure 4.10: The depth distribution of $Z_{1/2}$ including the overlapping contribution from E(265K), measured at two separate lateral distances. The defects are distributed in a fairly thin layer of about 1μm thickness throughout the sample.

and the generation rate of defects, J in units of defects/cm^{2}s. The generation rate is found according to Fick's first law, which was used as the natural boundary condition at the position of the beam,

$$J(x=0,t) = -D_{\text{eff}} \frac{\partial N_t}{\partial x}\bigg|_{x=0}$$

The boundary condition for large distances from the beam is the measured as-grown concentration of $Z_{1/2}$ about 1×10^{13} cm^{-3}. The diffusion time during simulations was set equal to the irradiation time, e.g. 1 hr at room temperature. The parameters D_{eff} and J were varied across a broad range and the diffusion equation was solved numerically for each set of (D_{eff}, J) until the values yielding the least squared error were found. The best fit was achieved for the rather large effective diffusivity $D_{\text{eff}} = 2.4 \times 10^{-5}$ cm^2/s and the generation rate of defects is approx. 4×10^{12} cm^{-2}s^{-1}, where the D_{eff} value corresponds to an energy barrier for migration of approx. 0.2 eV when assuming a typical prefactor in the diffusivity of 10^{-2} – 10^{-3} cm^2/s. The lateral diffusion length is 2.8 mm, defined as the distance where the concentration has decreased by a factor e^{-1}.

TRIM simulations yield the amount of energy lost by the protons to the ionization of lattice atoms, and consequently the number of electron-hole-pairs (EHPs) which are generated by each proton during the irradiation is found to be about 2000. The average ionization energy required to generate an EHP in 4H-SiC is 5.05 eV [71]. The lifetime of the charge carriers is assumed to be quite low, e.g. 0.1 – 0.01 μs, due to the high density of defects in the irradiated area and the similar electron- and hole concentrations, and the diffusivity is likewise assumed to be low, e.g. of the order 10^{-1} cm^2/s, due to heavy scattering in the irradiated volume. This yields a diffusion length of around 1 μm. In this case the steady-state density of EHPs during the irradiation is about 10^{15} cm^{-3} in a shallow cylindrical volume with approximately the same cross section as the proton beam (since the diffusion length is negligible in comparison), and a depth corresponding to the diffusion length of the charge carriers. This concentration of EHPs is of the same order as the effective electron concentration in equilibrium, which indicates that the availability of holes is the limiting factor in this migration process. Otherwise, this long range migration might be observed also during post-irradiation or post-implantation annealing (even at room temperature) which is not the case.

The species which actually migrate may in principle be the measured defects themselves, one (or more) of their constituents, or a separate, undetected "catalyst" species may migrate from the irradiated area and react with another species, ultimately leading to the formation of the defects observed here which remain stable at room temperature. As mentioned previously, ab initio density functional calculations [64] suggest that C_I can act as a catalyst in the production of antisite pairs, C_{Si} and Si_C, and each migrating C_I may leave behind many of these pairs as it migrates long distances. This process has an activation energy of 5.9 eV for neutral defects [64], and will therefore not occur at room temperature. However, in the presence of excess holes this reaction requires only at most 0.6 eV. When taking into account the accuracy of ab initio calculations and experimental uncertainties this activation energy is comparable to the 0.1 - 0.2 eV barriers for migration which have been extracted for the $Z_{1/2}$ and E(265K) centers in this chapter. This seems to suggest that these centers consist of combinations or clusters of silicon and carbon antisite defects. On the other hand, the diffusion lengths of minority charge carriers in high quality 4H-SiC is about 10 - 100 μm.

Hence, it is problematic to assign the mechanism which is driving such long range motion to electronically stimulated migration of point defects, since the migration occurs well outside of the region where minority carriers generated by the ionizing radiation are available. In addition, the pronounced anisotropy of the defect migration along the c-plane, as seen in Fig.4.10, is not immediately accounted for by ionization-enhanced motion of C_I. This may suggest that ionization-enhanced motion of C_I plays only a limited role.

Another mechanism which might be responsible for the defect migration is the previously mentioned recombination-enhanced dislocation glide (REDG) process, where basal plane dislocations move laterally in the presence of excess charge carriers with an activation energy of 0.27 eV and a velocity of $\approx 10^{-4}$ cm/s at 300 K. This process occurs both during forward bias injection of minority charge carriers in a pn-diode structure and under UV light illumination [70, 72], and these results were obtained at injection levels in the range of 10^{16} - 10^{19} cm^{-3}. Several properties seem to indicate a connection between the defect migration observed here and REDG; (1) charge carrier recombination appears to be a requirement in both cases for the processes to occur at RT, (2) strong anisotropy along the (0001) basal plane with little movement along the c-axis, (3) comparable migration distances on the order of several millimeters after 1 h irradiation or injection at RT are observed in both cases, (4) the migration distances of both observed defect levels, $Z_{1/2}$ and E(265K), are observed to be similar regardless of their individual origins or structure and (5) the observed broad features in the DLTS spectra which anneal out in less than 25 hrs at RT are believed to be due to extended defects, such as dislocations. In other words, the hypothesis that REDG is responsible for the observation of the $Z_{1/2}$ center far from the crater and irradiated area seems to match well with the experimental evidence.

The results presented here from irradiation inside a crater proved challenging to reproduce in a systematic manner, in contrast to both earlier and recent results where the irradiation is performed directly at the surface (paper IV-V), possibly due to the large local defect generation rate during the sputtering of the crater. This may create a sufficiently large concentration of defects to efficiently getter the subsequently generated defects during the proton irradiation and hence to completely prevent their migration. A number of experiments have been performed to remedy this situation, including lowering the local defect generation rate during the sputtering by reducing the sputter rate (low ion current and/or defocused beam), subsequent heat treatments in order to anneal out sputter-related damage before performing the irradiation, thermally oxidizing the material and etching in HF after sputtering in order to completely remove some 60 - 70 nm of sputter-damaged SiC, and simultaneously irradiating the sample with an electron gun to increase the generation of electron hole pairs. However, none of these strategies proved successful in systematically reproducing the results presented here, and further work is required to identify the critical process.

4.4.5 Summary

The $Z_{1/2}$ center — along with an unidentified center at E_C - 0.5 eV — has been observed at distances of up to 5 mm from a focused low energy proton beam at RT, after irradiation in a sputtered crater. This corresponds to a lateral diffusion length of 2.8 mm, as seen by fitting the measurements to the diffusion equation, which implies an energy barrier for migration of $\sim$0.2 eV. The migration process occurs under ionizing conditions with a concentration of excess charge carriers on the order of 10^{15} cm^{-3}. Recombination of electron-hole pairs

is a necessary condition for the defect migration. The DLTS spectra contain evidence of extended defects, and the observation of the $Z_{1/2}$ center at such long distances from the directly irradiated region is most likely related to the motion of these extended defects through processes like recombination-enhanced dislocation glide rather than the migration of specific point defects, such as C_I. The defects migrate laterally from the irradiated area and form a thin layer which is only about 1 μm thick, hence their lateral diffusivity appears to be far higher than their vertical diffusivity.

Chapter 5

Summary and outlook

Defect studies have had a high degree of focus in the SiC community in the last 15 years or so. Nonetheless, from the topics of submitted papers at the annual ECSCRM / ICSCRM conferences for example, it is clear that the SiC community overall is experiencing a shift from a large focus on structural and point defect studies and towards more high-level device oriented challenges, prototyping and commercial realization of more advanced devices than relatively simple Schottky diodes. Although this is certainly positive for the prognosis of future research and development on SiC, there are still major unresolved issues of technological and fundamental interest related to defects in this material.

Oxidation-enhanced annealing is a very convenient method of removing the lifetime limiting $Z_{1/2}$ center, as well as other levels in the upper half of the band gap, and has already reportedly been included as a standard processing step for commercial device fabrication. The details of the migration and reaction of the carbon interstitials have been revealed (paper I-III), e.g. the formation and migration energy barriers are both most likely approximately 3 eV and the activation energy for the overall (first-order) reaction has been experimentally determined as 5.4 eV (paper II). More work is required to further elucidate this annealing mechanism, the annealing as a function of implantation dose and temperature above 1200 °C, among other parameters. Further investigations should reveal more regarding the hints of another process at lower temperature competing for the injected C_I from the oxidizing interface, since the loss rate of $Z_{1/2}$ appears to undergo an abrupt increase between 1125 - 1150 °C.

Very recent results indicate strongly that the DLTS peaks $Z_{1/2}$ and EH_7 arise due to the doubly negative (=/0) and singly positive (0/+) charge state transitions of V_C, respectively [58]. However, this still leaves the obvious question of what the relationship is between EH_7 and EH_6, and the structure of the latter center which appears after high energy electron and proton irradiation.

The long-range migration phenomenon, where point and structural defects are observed several hundred μm and up to mm's away from the directly irradiated area, may have large technological consequences [12, 57] (paper IV-V). These observations indicate that the minority carrier lifetime will be adversely affected over large distances near selectively doped device regions, which may potentially be crucial knowledge for device designers. However, it is not known to *which* degree this phenomenon occurs during ion implantation for doping of the material, when the incident particles are much heavier than electrons and protons.

It is now clear that the so-called interface states comprises two different kinds of trapping states within the near-interfacial oxide (NIT) with trapping levels at E_C - 0.1 eV and the broader level with a maximum at E_C - 0.7 eV in 4H-SiC (paper VI), as well as a distribution of states at the interface itself (D_{it}). NITs are of unknown origin, but have been argued to be related to oxygen deficiencies [28, 29] or silicon interstitials [27], while the D_{it} are thought to be related to small carbon clusters [27]. Interface states can be suppressed by performing either a post-oxidation anneal in NO or by pre-implanting N and subsequently doing thermal oxidation. There are indications from C-V and TDRC measurements that NIT in the oxide can be charged by tunneling from the D_{it} at the interface in non-nitridated oxides (paper VII), and this mechanism requires further study.

Chapter 6

Summary of the papers

Papers I-III concern atomistic mechanisms and the effects of oxidation-enhanced annealing on the S_1/S_2, $Z_{1/2}$ and $EH_{6/7}$ centers. Laterally resolved DLTS studies of long range migration of point and extended defects are presented in papers IV and V, while interface defects in SiO_2 / 4H-SiC structures are studied in papers VI-VIII employing TDRC and C-V characterization.

6.1 Paper I

Annealing of the prominent $Z_{1/2}$ defect in 4H-SiC has been studied after thermal treatment in N_2 and O_2 atmospheres at $1150\ ^{\circ}\mathrm{C}$ subsequent to implantation with MeV Si-ions to doses in the range of $(1-4)\times 10^{8}$ cm^{-2}. The annealing rate is found to be significantly enhanced under oxidizing conditions, while in N_2 atmosphere $Z_{1/2}$ remains stable. Hence, a substantial lowering of the annealing temperature required for defect removal in 4H-SiC doped by ion implantation may be expected using oxidizing annealing atmosphere. Concentration versus depth profiles of $Z_{1/2}$ clearly show that it is annihilated by defect species injected from the SiO_2 /4H-SiC interface during oxidation. The injection rate of the in-diffusing species is found to be about $(1.2 \pm 0.2) \times 10^{6}$ cm^{-2} s^{-1} and the concentration ratio of the injected species relative to the native atoms originally present in the oxidized volume is $\sim 1 \times 10^{-7}$. A model where the annihilating species are injected from the surface with a diffusion coefficient of about 10^{-8} cm^{2} / s yields excellent agreement with the experimental data.

My contribution: I took part in the planning, did the sample processing (except for the ion implantation), performed the electrical characterization and analysis and wrote the first draft of the manuscript for proofreading and discussion with Bengt Svensson.

6.2 Paper II

High-purity epitaxial layers of n-type 4H-SiC have been implanted with 4.3 MeV Si ions to a dose of 3×10^{8} cm^{-2} and then subjected to dry isothermal oxidation at temperatures between 1050 and $1175\ ^{\circ}\mathrm{C}$. Analysis of the samples by depth-resolved deep level transient

spectroscopy unveils a strong oxidation-enhanced annealing of the prominent $Z_{1/2}$ center, commonly ascribed to the carbon vacancy. The integrated (total) loss of $Z_{1/2}$ centers is proportional to the thickness of the silicon dioxide (SiO_2) layer grown but the proportionality constant, or annihilation efficiency, decreases with decreasing oxidation temperature. At a given depth x, the annealing of $Z_{1/2}$ obeys first-order kinetics with a rate constant c having an activation energy of $\sim$5.3 eV. The pre-exponential factor of c decreases with increasing x and a normalized concentration-versus-depth distribution of the species injected from the surface and annihilating the $Z_{1/2}$ centers has been deducted. This species is believed to be the carbon interstitial and is labelled C_I ; numerical simulations of the reaction kinetics employing a model where (i) the generation rate of C_I at the SiO_2 / SiC interface is related to the oxidation rate, (ii) the diffusion of C_I into the SiC layer is fast, and (iii) a steady-state concentration profile of C_I is rapidly established, yield excellent agreement with the experimental data for both $Z_{1/2}$ (absolute values) and C_I (relative values). The activation energy obtained for the diffusivity of C_I is $\sim$3.0 eV, presumably reflecting the migration barrier for C_I and possibly some contribution from an extra barrier to be surmounted at the SiO_2 / SiC interface.

My contribution: I took part in the planning, did the sample processing (except for the ion implantation), performed the electrical characterization and analysis and wrote a draft of the manuscript for proofreading and discussion with Bengt Svensson.

6.3 Paper III

Annealing of the $Z_{1/2}$ and $EH_{6/7}$ centers has been studied by DLTS after ion implantation of MeV Si ions and subsequent annealing in either N_2 or O_2 at $1150\ ^\circ C$, in the dose range $(1-4)\times 10^8$ Si / cm^{-2}. It is found that the annealing rate of these prominent defects is greatly enhanced after thermal oxidation, and in particular close to the surface area, due to injection of a defect species which annihilates with both $Z_{1/2}$ and $EH_{6/7}$. The migration part of the diffusion coefficient of the injected defect is established to be in the range $(1-2)\times 10^{-8}$ cm^2 / s, and the measured concentration versus depth profiles of both $Z_{1/2}$ and $EH_{6/7}$ are accurately simulated by a simple model.

My contribution: I took part in the planning, did the sample processing (except for the ion implantation), performed the electrical characterization and analysis and wrote the first draft of the manuscript for proofreading and discussion with Bengt Svensson.

6.4 Paper IV

4H-SiC has been irradiated with 10 keV protons and a laterally resolved DLTS study is performed to investigate the diffusion of irradiation induced intrinsic point defects. It is found that the defects migrate on the order of hundreds of μm laterally and carbon interstitials (C_I) are believed to be involved in the defect formation. However, the vertical diffusion lengths are revealed to be several orders of magnitude shorter, on the order of hundreds of nm. Specifically, the $Z_{1/2}$, S_1/S_2 and $EH_{6/7}$ levels are found to be generated large distances away from the directly irradiated area, suggesting that C_I or another highly mobile species are involved in the formation of these defects.

My contribution: I took part in the planning, did the sample preparation (proton irradiation performed by Lasse Vines), performed the electrical characterization and analysis and wrote a draft of the manuscript for proofreading and discussion with both co-authors.

6.5 Paper V

The lateral distributions of intrinsic point defects in n-type (0001) 4H-SiC have been investigated following room temperature irradiation with a focused beam of 10 keV protons. Laterally resolved DLTS measurements reveal that the well-known and prominent $Z_{1/2}$ and S_1/S_2 centers display lateral diffusion lenghts on the order of one millimeter with negligible (if any) motion parallel to the direction of the c-axis. The migration occurs only in the presence of excess charge carriers generated during the proton irradiation and no further motion takes place even under subsequent optical excitation of high intensity. Assuming one-dimensional geometry, an effective defect diffusivity in excess of 10^{-6} cm^2/s is deduced by numerical modelling of the experimental data, corresponding to an energy barrier for migration of $\sim$0.2 eV. Possible mechanisms for the rapid migration, invoking charge carrier recombination as a necessary condition, are discussed, and especially, an association with the glide of partial dislocations along the (0001) basal plane is scrutinized in some detail.

My contribution: I took part in the planning, did the sample preparation (proton irradiation performed by Lasse Vines), performed the electrical characterization and analysis and wrote a draft of the manuscript for proofreading and discussion with both co-authors.

6.6 Paper VI

Electron states at the SiO_2 / 4H-SiC interface have been investigated using capacitor structures and especially, the influence of excess nitrogen, introduced by ion implantation, at the interface is studied in detail. Implanted and non-implanted n-type samples with an interfacial concentration of nitrogen of $\sim 10^{19}$ and 10^{16} cm^{-3}, respectively, were analyzed by C-V measurements, performed at different temperatures and probe frequencies, and TDRC measurements performed in the temperature range of 35-295 K. Three main categories of electron states are disclosed, true interface states (D_{it}), fast near interface states (NIT_{ox}^{fast}) and slow near interface states (NIT_{ox}^{slow}). The density versus energy distributions of D_{it} and NIT_{ox}^{fast} have been deduced from the TDRC data and they are shown to give a close quantitative agreement with the shape and frequency dependence of the C-V curves. Further, the amount of NIT_{ox}^{slow} extracted from TDRC is demonstrated to be responsible for the parallel shifts and hysterezis effects occurring in the C-V characteristics. All three categories of electron states are reduced in concentration in the implanted samples. This holds particularly for NIT_{ox}^{fast} with a peak at $\sim$0.1 eV below the conduction band edge of 4H-SiC that is suppressed by at least two orders of magnitude relative to the non-implanted samples. The decrease in D_{it} is also substantial (a factor of $\sim$10) while the loss of NIT_{ox}^{slow} is considerably smaller (only $\sim$30%). The results provide firm evidence that NIT_{ox}^{fast} and NIT_{ox}^{slow} do not originate from the same kind of defect center.

My contribution: In cooperation with the first author (Ioana Pintilie), I performed the electrical

characterization and analysis, and took part in the discussion of the results and manuscript. The first draft was written by the first author.

6.7 Paper VII

Comparative studies of gate oxides on a N^+ pre-implanted area ($N_{interface} \sim 1 \times 10^{19}$ cm^{-3}) have been undertaken by means of Capacitance-Voltage (C-V) characteristics, performed at different temperatures and frequencies, and Thermal Dielectric Relaxation Current (TDRC) technique. In the non-implanted samples the stretch out of the C-V curves get larger as the temperature is lowered to 150 K, while for even lower temperatures the C-V characteristics become steeper and some discontinuities occur. These discontinuities are specific for the non-implanted sample and are associated with charging of the fast near interface states (NIT_{ox}^{fast}) via a tunneling from the shallow interface states (D_{it}). The tunneling from the shallow D_{it} to NIT_{ox}^{fast} suppress the AC response of D_{it}, which is recovered only after most of the NIT_{ox}^{fast} are charged with electrons.

My contribution: In cooperation with the first author (Ioana Pintilie), I performed the electrical characterization and analysis, and took part in the discussion of the results and manuscript. The first draft was written by the first author.

6.8 Paper VIII

The purpose of this work is to compare the density of shallow interface states (D_{it}) at the interface of SiO_2 / SiC MOS capacitors as deducted by the conductance spectroscopy (CS) and thermally dielectric relaxation current (TDRC) techniques. Both capacitors of 4H- and 6H-SiC (n-type) are investigated, and both ordinary dry oxidation and an improved classified procedure have been employed. The two techniques are found to give rather good agreement for interface states located $\geq$0.3 eV below the conduction band edge (E_C) while for more shallow states vastly different distributions of D_{it} are obtained. Different reasons for these contradictory results are discussed, such as strong temperature and energy dependence of the capture cross section of the shallow interface states.

My contribution: I took part in the planning, did the sample preparation on behalf of UiO (there were also samples from the University of Nürnberg-Erlangen), performed the electrical characterization and analysis on behalf of UiO and wrote a first draft of the manuscript for proofreading and discussion with the co-authors.

References

[1] J. B. Casady, J. W. Johnson. *Solid-State Electronics.* 1996;39:1409–1422.

[2] G. Pensl, R. Helbig. Silicon Carbide (SiC) - Recent Results in Physics and in Technology in *Advances in Solid State Physics*;30:133–156Springer 1990.

[3] Y. M. Tairov, V. F. Tsvetkov. *Journal of Crystal Growth.* 1978;43:209–212.

[4] D. J. Larkin, P. G. Neudeck, J. A. Powell, L. G. Matus. *Applied Physics Letters.* 1994;65:1659.

[5] J. C. Bourgoin, J. W. Corbett. *Physics Letters.* 1972;38:135–137.

[6] T. R. Waite. *Physical Review.* 1957;107:463–470.

[7] A. Hallen, E. al.. *Nuclear Instruments and Methods in Physics Research Section B: Beam Interactions with Materials and Atoms.* 2002;186:186–194.

[8] J. Ziegler. SRIM 2010.

[9] S. Seshadri, G. W. Eldridge, a. K. Agarwal. *Applied Physics Letters.* 1998;72:2026.

[10] H. J. Bardeleben, J. L. Cantin, L. Henry, M. F. Barthe. *Physical Review B.* 2000;62:10841–10846.

[11] L. Storasta, J. P. Bergman, E. Janzén, A. Henry. *Journal of Applied Physics.* 2004;96:4909.

[12] J. Steeds, G. A. Evans, L. R. Danks, et al. *Diamond and Related Materials.* 2002;11:1923–1945.

[13] A. A. Rempel, W. Sprengel, K. Blaurock, K. J. Reichle, J. Major, H.-E. Schaefer. *Physical Review Letters.* 2002;89:3–6.

[14] J. P. Doyle, M. K. Linnarsson, P. Pellegrino, et al. *Journal of Applied Physics.* 1998;84:1354.

[15] C. Persson, U. Lindefelt. *Journal of Applied Physics.* 1997;82:5496.

[16] C. Hemmingsson, N. T. Son, O. Kordina, et al. *Journal of Applied Physics.* 1997;81:6155.

[17] T. Dalibor, G. Pensl, T. Kimoto, et al. *Diamond and Related Materials.* 1997;6:1333–1337.

[18] T. Dalibor, G. Pensl, H. Matsunami, et al. *Phys. Status Solidi A.* 1997;162:199.

[19] M. L. David, G. Alfieri, E. V. Monakhov, et al. *Journal of Applied Physics.* 2004;95:4728.

[20] G. Alfieri, E. V. Monakhov, B. G. Svensson, M. K. Linnarsson. *Journal of Applied Physics.* 2005;98:43518.

[21] L. C. Kimerling. *Journal of Applied Physics.* 1974;45:1839.

[22] D. V. Lang. *1Journal of Applied Physics.* 1974;45:3023.

[23] J. Simmons, G. Taylor. *Solid-State Electronics.* 1974;17:125–130.

[24] L. R. Weisberg, H. Schade. *Journal of Applied Physics.* 1968;39:5149.

[25] B. E. Deal, A. S. Grove. *Journal of Applied Physics.* 1965;36:3770.

[26] Y. Song, S. Dhar, L. C. Feldman, G. Chung, J. R. Williams. *Journal of Applied Physics.* 2004;95:4953.

[27] P. Deak, J. M. Knaup, T. Hornos, C. Thill, A. Gali, T. Frauenheim. *Journal of Physics D: Applied Physics.* 2007;40:6242–6253.

[28] V. V. Afanas'ev, M. Bassler, G. Pensl, M. Schulz. *Phys. Status Solidi A.* 1997;162:321.

[29] V. Afanas'ev, a. Stesmans. *Physical Review Letters.* 1997;78:2437–2440.

[30] M. Avice, U. Grossner, I. Pintilie, B. G. Svensson, O. Nilsen, H. Fjellvag. *Applied Physics Letters.* 2006;89:222103.

[31] M. Avice, U. Grossner, I. Pintilie, et al. *Journal of Applied Physics.* 2007;102:054513.

[32] E. Pippel, J. Woltersdorf, H. Olafsson, E. Sveinbjörnsson. *Journal of Applied Physics.* 2005;97:034302.

[33] T. Rudenko, I. Osiyuk, I. Tyagulski, H. Olafsson, E. Sveinbjornsson. *Solid-State Electronics.* 2005;49:545–553.

[34] S. Dimitrijev, H. Harrison, D. Sweatman. *IEEE Electron Device Letters.* 1997;18:175–177.

[35] S. Dimitrijev, P. Tanner, H. B. Harrison. *Microelectronics Reliability.* 1999;39:441–449.

[36] V. V. Afanas'ev, A. Stesmans, F. Ciobanu, G. Pensl, K. Y. Cheong, S. Dimitrijev. *Applied Physics Letters.* 2003;82:568.

[37] F. Ciobanu, G. Pensl, V. Afanas'ev, A. Schoner. *Materials Science Forum.* 2005;483-485:693.

[38] G. Pensl, F. Ciobanu, T. Frank, et al. *Microelectronic Engineering.* 2006;83:146–149.

[39] A. Poggi, F. Moscatelli, Y. Hijikata, S. Solmi, R. Nipoti. *Microelectronic Engineering.* 2007;84:2804–2809.

[40] X. Shen, S. T. Pantelides. *Applied Physics Letters.* 2011;98:053507.

[41] T. Hatayama, S. Hino, N. Miura, T. Oomori, E. Tokumitsu. *IEEE transactions on electron devices.* 2008;55:2041–2045.

[42] T. Kimoto, A. Itoh, H. Matsunami, et al. Nitrogen donors and deep levels in high quality 4H-SiC epilayers grown by chemical vapor deposition 1995.

[43] J. Zhang, L. Storasta, J. P. Bergman, N. T. Son, E. Janzen. *Journal of Applied Physics.* 2003;93:4708.

[44] T. Kimoto, K. Hashimoto, H. Matsunami. *Japanese Journal of Applied Physics.* 2003;42:7294–7295.

[45] P. B. Klein, B. V. Shanabrook, S. W. Huh, et al. *Applied Physics Letters.* 2006;88:52110.

[46] K. Danno, D. Nakamura, T. Kimoto. *Applied Physics Letters.* 2007;90:202109.

[47] C. G. Hemmingsson, N. T. Son, A. Ellison, J. Zhang, E. Janzén. *Physical Review B.* 1998;58:R10 119.

[48] I. Pintilie, L. Pintilie, K. Irmscher, B. Thomas. *Applied Physics Letters.* 2002;81:4841.

[49] L. Storasta, A. Henry, J. P. Bergman, E. Janzen. *Materials Science Forum.* 2004;457-460:469–472.

[50] K. Danno, T. Kimoto. *Journal of Applied Physics.* 2006;100:113728.

[51] T. Kimoto, S. Nakazawa, K. Hashimoto, H. Matsunami. *Applied Physics Letters.* 2001;79:2761.

[52] T. Hornos, A. Gali, B. G. Svensson. *Materials Science Forum.* 2011;679-680:261–264.

[53] T. Hiyoshi, T. Kimoto. *Applied Physics Express.* 2009;2:91101.

[54] K. Kawahara, J. Suda, G. Pensl, T. Kimoto. *Journal of Applied Physics.* 2010;108:033706.

[55] L. Storasta, H. Tsuchida. *Applied Physics Letters.* 2007;90:062116.

[56] J. W. Steeds, W. Sullivan, A. Wotherspoon, J. M. Hayes. *Journal of Physics: Condensed Matter.* 2009;21:364219.

[57] G. Alfieri, U. Grossner, E. V. Monakhov, B. G. Svensson, J. W. Steeds, W. Sullivan. *Materials Science Forum.* 2006;527-529:485–488.

[58] N. T. Son, X. T. Trinh, L. S. Løvlie, et al. *To be published.* 2012.

[59] T. Hiyoshi, T. Kimoto. *Applied Physics Express.* 2009;2:41101.

[60] I. Pintilie, U. Grossner, K. Irmscher, B. Thomas, B. G. Svensson. *Applied Physics Letters.* 2007;90:62113.

[61] J. Wong-Leung, B. G. Svensson. *Applied Physics Letters.* 2008;92:142105.

[62] G. Alfieri, E. V. Monakhov, B. G. Svensson, A. Hallen. *Journal of Applied Physics.* 2005;98:113524.

[63] L. Storasta, F. H. C. Carlsson, J. P. Bergman, E. Janzen. *Applied Physics Letters.* 2005;86:091903.

[64] T. Eberlein, C. Fall, R. Jones, P. Briddon, S. Öberg. *Physical Review B.* 2002;65:1–4.

[65] Y. Bar-Yam, J. D. Joannopoulos. *Physics Review Letters.* 1984;52:1129–1132.

[66] J. Adey, R. Jones, D. Palmer, P. Briddon, S. Öberg. *Physical Review Letters.* 2004;93:1–4.

[67] J. Schmidt, K. Bothe, D. Macdonald, J. Adey, R. Jones, D. W. Palmer. *Journal of Materials Research.* 2006;21:5–12.

[68] L. I. Murin, E. a. Tolkacheva, V. P. Markevich, et al. *Applied Physics Letters.* 2011;98:182101.

[69] A. A. Istratov. *Journal of Applied Physics.* 1997;82:2965.

[70] A. Galeckas, J. Linnros, P. Pirouz. *Applied Physics Letters.* 2002;81:883.

[71] M. V. S. Chandrashekhar, C. I. Thomas, M. G. Spencer. *Applied Physics Letters.* 2006;89:042113.

[72] A. Galeckas, J. Linnros, P. Pirouz. *Physical Review Letters.* 2006;96:1–4.

Paper I

Enhanced annealing of implantation-induced defects in 4H-SiC by thermal oxidation

L. S. Løvlie[a] and B. G. Svensson
Department of Physics, Center for Materials Science and Nanotechnology, University of Oslo, P.O. Box 1048 Blindern, N-0316 Oslo, Norway

(Received 22 August 2010; accepted 6 December 2010; published online 3 February 2011)

Annealing of the prominent $Z_{1/2}$ defect in 4H-SiC has been studied after thermal treatment in N_2 and O_2 atmospheres at 1150 °C subsequent to implantation with MeV Si-ions to doses in the range of $(1-4)\times 10^8$ cm^{-2}. The annealing rate is found to be significantly enhanced under oxidizing conditions, while in N_2 atmosphere $Z_{1/2}$ remains stable. Hence, a substantial lowering of the annealing temperature required for defect removal in 4H-SiC doped by ion-implantation may be expected using oxidizing annealing atmosphere. Concentration versus depth profiles of $Z_{1/2}$ clearly show that it is annihilated by defect species injected from the SiO_2/4H-SiC interface during oxidation. The injection rate of the in-diffusing species is found to be about $(1.2\pm 0.2)\times 10^6$ cm^{-2} s^{-1}, and the concentration ratio of the injected species relative to the native atoms originally present in the oxidized volume is $\sim 1\times 10^{-7}$. A model where the annihilating species are injected from the surface with a diffusion coefficient of about 10^{-8} cm^2/s yields excellent agreement with the experimental data. © *2011 American Institute of Physics*. [doi:10.1063/1.3531755]

Silicon carbide (SiC) is a rapidly maturing material for, in particular, high voltage, high temperature, and high frequency electronic devices, of which the most common polytypes are 3C-SiC, 4H-SiC, and 6H-SiC. However, dopant diffusivities in SiC are too low to accommodate doping by in-diffusion; hence, ion-implantation for selective area doping is a crucial technique for the realization of SiC devices. However, ion-implantation introduces substantial amounts of damage in the form of electrically active point defects which are detrimental to device performance and need to be removed by postimplant annealing. In particular, this holds for the prominent so-called $Z_{1/2}$ defect,[1,2] exhibiting an acceptor-like level at 0.7 eV below the conduction band (E_C) in 4H-SiC, which has been shown to be a lifetime limiting defect for charge carriers.[3] This defect is typically present in concentrations on the order of $10^{12}-10^{13}$ cm^{-3} in as-grown 4H-SiC and is considered to be of intrinsic nature.

$Z_{1/2}$ is known to have an extreme thermal stability, persisting up to 2000 °C, making thermal annealing difficult.[4] In addition, high temperature treatments cause surface roughness and incompatibility with other materials and preceding device process steps. Recently, Hiyoshi and Kimoto[5,6] reported that thermal oxidation at temperatures in the range of 1150–1300 °C reduces the concentration of $Z_{1/2}$ in as-grown 4H-SiC to below the detection limit of deep level transient spectroscopy (DLTS), i.e., about 10^{11} cm^{-3} in 10^{15} cm^{-3} doped layers. Hiyoshi and Kimoto[5,6] attributed the annealing of $Z_{1/2}$ to annihilation by carbon interstitials (I_C) diffusing in from the oxidizing interface under the assumption that $Z_{1/2}$ invokes the carbon vacancy (V_C).[7–9]

In this contribution, a dramatically increased annealing rate of $Z_{1/2}$ is found in Si-implanted samples subjected to thermal dry oxidation relative to that for treatment in inert conditions. Two sets of identical n-type (nitrogen doped) 4H-SiC samples, purchased from Cree Inc., grown 4° off the c-axis and featuring a 10 μm thick epitaxial layer on the Si-face of a highly doped bulk substrate ($\sim 10^{18}$ cm^{-3}), were implanted with 4.3 MeV Si-ions at room temperature (RT) to doses between $(1-4)\times 10^8$ cm^{-2}. The implants were performed in a direction close to the sample normal to minimize channeling.[10] The effective carrier concentrations, as determined by capacitance-voltage measurements at RT, were $(2-3)\times 10^{15}$ cm^{-3} in the epitaxial layer. Subsequent to the implantation one set of samples was treated in flowing nitrogen (N_2) at 1150 °C for 3.5 h, whereas the other set was treated in dry oxygen at 1150 °C for 3.5 h, resulting in a SiO_2 surface layer with a thickness of 35 nm as measured by ellipsometry. The oxidized samples were then etched in diluted hydrofluoric acid, and after standard cleaning, Schottky barrier diodes were formed by electron beam evaporation of nickel on both sets of samples. Except for converting less stable implantation related defects into $Z_{1/2}$ (Ref. 11) and causing a slight increase of the $E_C-0.7$ eV level amplitude, no effects were found on the concentration of $Z_{1/2}$ after the annealing in N_2. The concentration of $Z_{1/2}$ in the as-grown material was uniform and determined to be about 3×10^{12} cm^{-3}.

Figure 1 shows concentration versus depth profiles of $Z_{1/2}$, as deduced by monitoring the $E_C-0.7$ eV level using a refined version of the DLTS setup described in Ref. 12 and taking into account the so-called λ-effect, for oxidized samples and samples annealed in N_2. Data are included for two different doses (1×10^8 and 2×10^8 cm^{-2}), and the $Z_{1/2}$ concentration has decreased dramatically during the oxidation. In Fig. 2 the relative amount of annihilated $Z_{1/2}$ centers is plotted together with the original depth profiles for samples implanted with 3×10^8 cm^{-2} and annealed in N_2 or O_2. The fraction of annihilated $Z_{1/2}$ centers decreases from approximately 1 close to the surface and approaches 0 toward the bulk, clearly illustrating that the disappearance of $Z_{1/2}$ is due to annihilation by defect species injected from the

[a]Electronic mail: l.s.lovlie@smn.uio.no.

 © 2011 American Institute of Physics

Downloaded 03 Apr 2011 to 193.157.207.210. Redistribution subject to AIP license or copyright; see http://apl.aip.org/about/rights_and_permissions

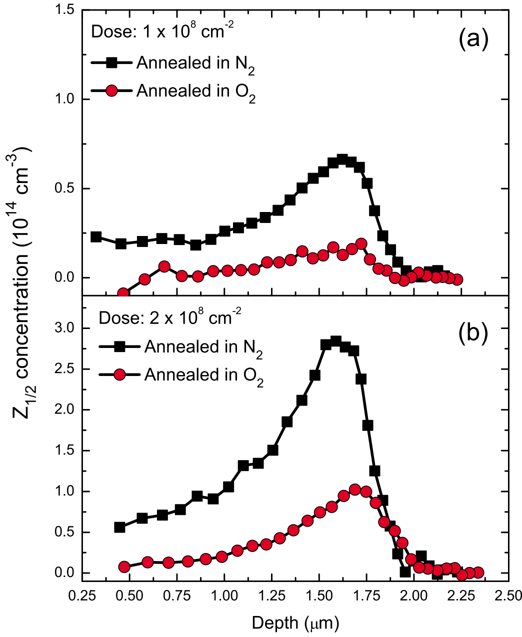

FIG. 1. (Color online) Concentration vs depth profiles of the $Z_{1/2}$ level at $E_C-0.7$ eV in n-type 4H-SiC epitaxial layers implanted with 4.3 MeV Si-ions to doses of (a) 1×10^8 and (b) 2×10^8 cm^{-2} and subsequently annealed in N_2 and O_2 atmospheres. Both of the annealings were performed at 1150 °C for 3.5 h. The depth profiles were measured at a sample temperature of 289 K with a lock-in rate window of $(640\ \mathrm{ms})^{-1}$.

oxidizing interface. Figure 3 displays the $Z_{1/2}$ concentration versus ion dose in the implantation peak for the N_2- and O_2-annealed samples. In both cases, the slopes are linear, but the introduction rate is about half in the latter samples relative to that in the former ones. This difference becomes even more pronounced when considering depths up to 1 μm only, where the integrated amount of $Z_{1/2}$ centers is only 12% in the O_2-annealed samples relative to that in the N_2-annealed ones. Depths up to 1 μm are highly relevant for device processing, so this illustrates that the oxidation enhanced annealing procedure may have great potential for device fabrication.

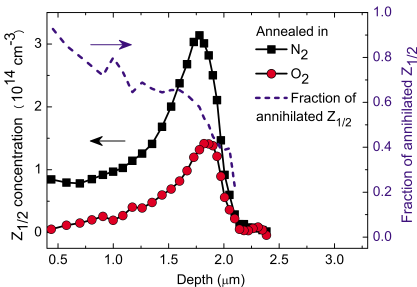

FIG. 2. (Color online) Concentration vs depth profiles of $Z_{1/2}$ in samples implanted with a dose of 3×10^8 Si/cm^2 and then annealed in N_2 or O_2 atmosphere. Also shown is the difference between the two depth profiles normalized to the content of $Z_{1/2}$ in the N_2-annealed sample.

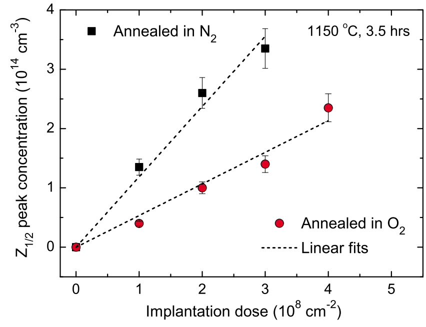

FIG. 3. (Color online) Concentration vs depth profiles of $Z_{1/2}$ in the implantation peak region vs ion dose for samples implanted with 4.3 MeV Si-ions and then annealed in N_2 or O_2 atmosphere. There is a linear dependence in both cases, indicating that $Z_{1/2}$ is directly generated during the implantation. The error bars give an estimate of the measurement uncertainty.

Based on the evidence that $Z_{1/2}$ is annihilated by reaction with some species injected from the oxidizing interface, which is labeled X, the following system of coupled partial differential equations can be derived to describe the defect evolution:[13]

$$\frac{\partial[Z_{1/2}]}{\partial t} = -4\pi R D_X[Z_{1/2}][X], \qquad (1)$$

$$\frac{\partial[X]}{\partial t} = D_X\frac{\partial^2[X]}{\partial x^2} - 4\pi R D_X[Z_{1/2}][X]. \qquad (2)$$

Here $[\cdot]$ denotes the concentration of a defect species, x is the sample depth, and t is the annealing time. R is the capture radius of the reaction between $Z_{1/2}$ and X. D_X is the diffusion coefficient of X while $Z_{1/2}$ is considered as immobile at 1150 °C. The original depth profile of $Z_{1/2}$ is taken from the N_2-annealed samples, while X is assumed to originate from the SiO_2/SiC interface. The initial depth distribution of [X] is treated as uniform with a width on the order of 1 nm (the results are found to be fairly insensitive to the width of [X] at t=0).

If every injected X defect contributes to the annihilation of $Z_{1/2}$, a lower limit for the time-integrated flux of X injected from the oxidizing interface is found by taking the difference between the integrated concentration versus depth profiles of $Z_{1/2}$ after annealing in N_2 and O_2. Using the values for all doses, this yields an average value of

$$N_{inj} = (1.5\pm0.3)\times10^{10} \quad \text{injected X/cm}^2. \qquad (3)$$

The inward flux of X, J_X, decreases with increasing thickness of the grown oxide, but in a first approximation the average injection rate after 3.5 h oxidation is put as

$$J_X = \frac{N_{inj}}{t_{ox}} = (1.2\pm0.2)\times10^6 \quad \text{injected X/cm}^2\,\text{s}. \qquad (4)$$

Taking into account the oxide thickness and the fraction of SiC consumed during the oxidation (0.44), the ratio of the number of injected X to the total number of Si and C atoms in the oxidized volume becomes approximately 1×10^{-7}. The boundary conditions for X are

$$J_X(x=0) = D_X\frac{\partial[X]}{\partial x} = (1.2\pm0.2)\times10^6 \ \text{X/cm}^2\,\text{s}, \qquad (5)$$

Downloaded 03 Apr 2011 to 193.157.207.210. Redistribution subject to AIP license or copyright; see http://apl.aip.org/about/rights_and_permissions

TABLE I. An overview of the model parameters and their values.

Parameter	Value
R	5 Å (based on geometrical considerations)
D_X	Free parameter
$[X]_{x=0}$	5×10^{15} cm^{-3}
J_X	$(1.2\pm0.2)\times10^{-6}$ cm^{-2} s^{-1}

$$[X](x\to\infty)=0. \quad (6)$$

The parameter values used in the calculations are listed in Table I where D_X is taken as a free parameter in the simulations of $[Z_{1/2}](x)$. Using the parameter values given in Table I, the experimental depth profiles of $Z_{1/2}$ after oxidation can be simulated with excellent accuracy for all the implantation doses employed in this work, as illustrated in Fig. 4, for the dose of 2×10^8 cm^{-2}. Irrespective of the dose, the extracted values of D_X are found to be in the range of $(0.9-1.3)\times10^{-8}$ cm^2/s. By variation of D_X and J_X correspondingly, the simulated $Z_{1/2}$ concentration versus depth profile can be kept constant at the measured amplitude, and also the concentration tail toward the surface follows the measured one. Thus, the extracted values for D_X and J_X, with an oxide thickness of 35 nm, can be regarded as a lower limit yielding agreement with the shape as well as the absolute values of the whole depth profile.

It is generally agreed upon that $Z_{1/2}$ is a fundamental intrinsic defect related to carbon, but the atomic configuration is still controversial; evidence exists in the literature for the involvement of the carbon vacancy[7–9] as well as of the carbon interstitial.[14,15] The results in our study are consistent with both these models and cannot be used for a distinction. However, the present data show unambiguously that $Z_{1/2}$ is annihilated by migrating species injected from the surface during dry thermal oxidation, most likely the carbon interstitial which may favor an assignment of $Z_{1/2}$ to the carbon vacancy.[5,6] In such a scenario, the extracted values for D_X ($\sim10^{-8}$ cm^2/s at 1150 °C) correspond to the migration of carbon interstitials, and if a pre-exponential factor of typically $\sim10^{-2}-10^{-3}$ cm^2/s is assumed, a migration energy of 1.5–2 eV is deduced, which is fully consistent with *ab initio* predictions based on density functional theory.[16]

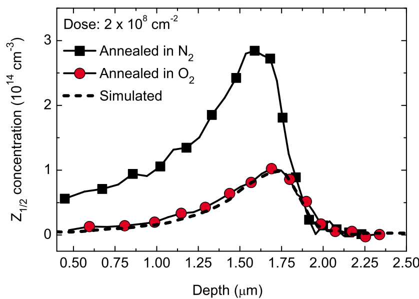

FIG. 4. (Color online) Comparison between experimental and simulated concentrations vs depth profiles of $Z_{1/2}$ in 4H-SiC implanted with 2×10^8 Si/cm^2 (4.3 MeV) and then annealed in O_2 atmosphere (1150 °C, 3.5 h). The experimental profile obtained after annealing in N_2 atmosphere is also included and used for input for the simulations at t=0.

In summary, the present results obtained for annealing in O_2 atmosphere show great promise to reduce the heat treatment temperatures required for annihilation of implantation-induced defects in 4H-SiC. Further work is in progress to explore this concept for high doses of both n-type dopants (like N) and p-type dopants (like Al).

Financial support from the Norwegian Research Council (FRINAT program) is gratefully acknowledged.

[1] C. G. Hemmingsson, N. T. Son, A. Ellison, J. Zhang, and E. Janzén, Phys. Rev. B 58, R10119 (1998).
[2] T. Dalibor, G. Pensl, T. Kimoto, H. Matsunami, S. Sridhara, R. T. Devaty, and W. J. Choyke, Diamond Relat. Mater. 6, 1333 (1997).
[3] P. B. Klein, B. V. Shanabrook, S. W. Huh, A. Y. Polyakov, M. Skowronski, J. J. Sumakeris, and M. J. O'Loughlin, Appl. Phys. Lett. 88, 052110 (2006).
[4] G. Alfieri, E. V. Monakhov, B. G. Svensson, and M. K. Linnarsson, J. Appl. Phys. 98, 043518 (2005).
[5] T. Hiyoshi and T. Kimoto, Appl. Phys. Express 2, 041101 (2009).
[6] T. Hiyoshi and T. Kimoto, Appl. Phys. Express 2, 091101 (2009).
[7] L. Storasta, J. P. Bergman, E. Janzén, and A. Henry, J. Appl. Phys. 96, 4909 (2004).
[8] T. Kimoto, S. Nakazawa, K. Hashimoto, and H. Matsunami, Appl. Phys. Lett. 79, 2761 (2001).
[9] K. Fujihira, T. Kimoto, and H. Matsunami, Appl. Phys. Lett. 80, 1586 (2002).
[10] J. Wong-Leung, M. Janson, and B. G. Svensson, J. Appl. Phys. 93, 8914 (2003).
[11] J. P. Doyle, M. K. Linnarsson, P. Pellegrino, N. Keskitalo, B. G. Svensson, A. Schöner, N. Nordell, and J. L. Lindström, J. Appl. Phys. 84, 1354 (1998).
[12] B. G. Svensson, K.-H. Rydén, and B. M. S. Lewerentz, J. Appl. Phys. 66, 1699 (1989).
[13] T. R. Waite, Phys. Rev. 107, 463 (1957).
[14] I. Pintilie, U. Grossner, K. Irmscher, B. Thomas, and B. G. Svensson, Appl. Phys. Lett. 90, 062113 (2007).
[15] A. Gali, N. T. Son, and E. Janzén, Phys. Rev. B 73, 033204 (2006).
[16] M. Bockstedte, A. Mattausch, and O. Pankratov, Phys. Rev. B 68, 205201 (2003).

Downloaded 03 Apr 2011 to 193.157.207.210. Redistribution subject to AIP license or copyright; see http://apl.aip.org/about/rights_and_permissions

Paper II

Kinetics of oxidation-enhanced annealing of implantation-induced $Z_{1/2}$ centers in 4H-SiC

L. S. Løvlie and B. G. Svensson

University of Oslo, Department of Physics / Center for Materials Science and Nanotechnology, P.O. Box 1048 Blindern, N-0316 Oslo, Norway

Abstract

High-purity epitaxial layers of n-type 4H-SiC have been implanted with 4.3 MeV Si ions to a dose of 3×10^8 cm^{-2} and then subjected to dry isothermal oxidation at temperatures between 1050 and 1175 °C. Analysis of the samples by depth-resolved deep level transient spectroscopy unveils a strong oxidation-enhanced annealing of the prominent $Z_{1/2}$ center, commonly ascribed to the carbon vacancy. The integrated (total) loss of $Z_{1/2}$ centers is proportional to the thickness of the silicon dioxide (SiO_2) layer grown but the proportionality constant, or annihilation efficiency, decreases with decreasing oxidation temperature. At a given depth x, the annealing of $Z_{1/2}$ obeys first-order kinetics with a rate constant c having an activation energy of ~5.3 eV. The pre-exponential factor of c decreases with increasing x and a normalized concentration-versus-depth distribution of the species injected from the surface and annihilating the $Z_{1/2}$ centers has been deducted. This species is believed to be the carbon interstitial and is labelled C_I ; numerical simulations of the reaction kinetics employing a model where (i) the generation rate of C_I at the SiO_2 / SiC interface is related to the oxidation rate, (ii) the diffusion of C_I into the SiC layer is fast, and (iii) a steady-state concentration profile of C_I is rapidly established, yield excellent agreement with the experimental data for both $Z_{1/2}$ (absolute values) and C_I (relative values). The activation energy obtained for the diffusivity of C_I is ~3.0 eV, presumably reflecting the migration barrier for C_I and possibly some contribution from an extra barrier to be surmounted at the SiO_2 / SiC interface.

I. Introduction

The most common polytypes of silicon carbide (SiC), 3C, 4H and 6H, are gradually becoming attractive electronic materials in terms of high quality bulk and epitaxially grown layers and also in terms of dopant and defect control. However, unlike most other semiconductors, the available methods for selective area doping of SiC are almost inherently restricted to ion implantation, due to the low diffusivity of most dopant elements [1–3]. This makes a genuine understanding

of implantation-induced defects of paramount importance, in order to gain acceptable dopant activation and tailoring of the charge carrier lifetime in active parts of SiC devices.

In particular, the prominent $Z_{1/2}$ center, which exhibits an acceptor-like level at about E_C - 0.65 eV in 4H-SiC (E_C denotes the conduction band edge) [4,5], has been shown to have a detrimental effect on the minority charge carrier lifetime [6]. $Z_{1/2}$ is typically present in concentrations on the order of 10^{12} - 10^{13} cm^{-3} in as-grown material and is considered to be of intrinsic nature. $Z_{1/2}$ can be reduced in concentration by annealing but a complete removal is challenging since it has been shown to remain or even reform at temperatures approaching 2000 °C [7, 8]. Recently, however, several reports have shown that [$Z_{1/2}$] (brackets denote concentration values) can be reduced below the detection limit ($\leq 10^{10}$ cm^{-3}) in a surface layer by either a shallow carbon implantation followed by annealing at 1600 °C [9] or, perhaps more conveniently, thermal oxidation performed on the Si-face at comparatively low temperature (~1100 °C) [10–12]. Effectively, a 'defect free' layer with an extension of several tens of micrometers in thickness can be formed. In both cases, the removal of $Z_{1/2}$ was attributed to the in-diffusion of a defect species, presumably the carbon interstitial (C_I), which reacts with and annihilates $Z_{1/2}$. Accordingly, the atomic structure of $Z_{1/2}$ involves most likely a carbon vacancy (V_C) [13–17].

Convincing evidence exists in the literature, obtained by different types of experiments, that $Z_{1/2}$ is, indeed, carbon related [10, 14, 17–19]. This is also corroborated by modeling results based on density-functional-theory (DFT) where V_C and Si-C antisite pairs have been put forward as possible candidates [20–22].

Thermal oxidation of SiC resembles that of silicon but with the additional role of carbon; carbon can be (i) released in the form of CO and CO2, (ii) incorporated and trapped in the growing layer of SiO_2, and/or (iii) accumulated at the SiO_2 SiC interface and injected into the bulk of SiC as C_I. In addition to the removal of $Z_{1/2}$, thermal oxidation leads also, via process (iii), to the formation of a donor-like defect with a level in the lower half of the band gap, detected in p-type material. For both low and high dose implantations, this center can be annealed out at 1400 - 1500 °C under inert ambient conditions [23].

In this work, we have studied the effect of thermal oxidation on $Z_{1/2}$ during isothermal treatment at temperatures in the range 1050 - 1175 °C. The relative depth distribution of the migrating/injected C_I's is determined together with the kinetics and activation energy of the annihilation process of $Z_{1/2}$. A first-order reaction is revealed with a decreasing rate constant as a function of depth, implying an almost time-independent (steady-state) concentration profile of C_I at a given temperature. The experimental data are compared with simulations of the defect kinetics, assuming a 'simple' reaction model, and quantitative values for the generation rate and diffusion of C_I are deduced.

II. Experiment

The material studied was n-type (0001) 4H-SiC, purchased from Cree Inc., with a 4° off-cut angle and a 10 μm thick epitaxial layer grown by Chemical Vapor Deposition (CVD) on a highly n-doped substrate ($\sim 10^{18}$ cm^{-3}). The epitaxial layer was doped with nitrogen to an effective carrier concentration of $\sim 2.5 \times 10^{15}$ cm^{-3}. The samples were implanted with 4.3 MeV Si ions to a dose of 3×10^{8} cm^{-2}, yielding a defect distribution peaking at about 1.5 μm. The concentration of $Z_{1/2}$ centers before implantation was 3×10^{12} cm^{-3} and uniformly distributed as a function of depth, as measured by deep level transient spectroscopy (DLTS). Subsequently, the implanted samples were annealed in dry O_2 atmosphere at temperatures between 1050 - 1175 °C, and circular Schottky contacts with diameter of 800 μm were formed by thermal evaporation of Ni after oxide removal in diluted hydrofluoric acid. In parallel, control samples were prepared under identical conditions except for annealing in dry N_2 (and not O_2) atmosphere. DLTS and capacitance - voltage (C-V) measurements were then used to determine the concentration-versus-depth profiles of $Z_{1/2}$ and the charge carriers, respectively. For the measurements, an upgraded version of a custom made setup, described in detail elsewhere [24], was employed. Especially, the concentration-versus-depth profiles of $Z_{1/2}$ were obtained by selecting one rate window and holding the temperature constant at the maximum of the peak. The steady-state reverse bias voltage was kept constant, while gradually increasing the amplitude of the filling pulse (50 ms duration). The depth profiles were then extracted from the dependence of the recorded DLTS signal on the pulse amplitude, where the voltages used were converted into depth according to the conventional relations for a Schottky contacts and accounting for the so-called λ-effect.

III. Defect kinetics; some basic considerations

A defect species A, with concentration [A]=[A](T,x,t), anneals according to a first-order process if the decay rate is proportional to [A],

$$\frac{\partial [A]}{\partial t} = -c(T,x)[A] \tag{1}$$

where c(T,x) is the decay constant, T is the absolute temperature, x is the sample depth and t is the annealing time. This gives an exponential time dependence with the solution,

$$[A](T,x,t) = [A]_0 e^{-c(T,x)t} \tag{2}$$

where $[A]_0$ is the concentration at t=0 and [A] is assumed to vanish at t=∞. The decay constant c(T,x) is typically represented on an Arrhenius form,

$$c(T,x) = c_0(x) e^{-E_a/kT} \tag{3}$$

where c_0 is the frequency factor and E_a is the activation energy for the decay process.

In principle, there are three kinds of reaction processes giving rise to first-order kinetics (see ref. [25] and references therein); (i) dissociation where A disintegrates into its constituents while back reactions (association) are negligible, (ii) a reaction between A and a species B with a much larger concentration than A, and (iii) a reaction between A and a species B which is continuously replenished by a source such that [B] remains constant as a function of time.

The rate of change in the concentration of defects involved in diffusion-limited reactions can be described by coupled partial differential equations [26], and assuming the case (ii) or (iii) one obtains for A:

$$\frac{\partial [A]}{\partial t} = -4\pi R(D_A + D_B)[B][A] + D_A \frac{\partial^2 [A]}{\partial x^2} \tag{4}$$

where R is referred to as the capture radius of the reaction with B, and D_A and D_B are the diffusivities of A and B, respectively. The first term on the right hand side of Eq. (4) describes the reaction rate between A and B, while the second one accounts for diffusion of A if a concentration gradient exists. Typically, one of the species is much more mobile than the other at a given temperature. Assuming $D_B \gg D_A$ and that [B] remains essentially constant as a function of time, Eq. (4) becomes identical to Eq. (1) with $c(T, x) = 4\pi R D_B [B]$. Case (ii) ($[A] \ll [B]$) is commonly encountered by irradiation-induced defects interacting with oxygen in Czochralski-grown silicon, where $[O_I] \approx 10^{18}$ cm^{-3} while the defect concentrations are typically at least one order of magnitude lower [25]. Case (iii) is more exotic, since it requires a continuous supply of B in order to maintain a constant concentration as a function of time ($[B](t = 0) \approx [B](t = \infty)$ in spite of [A] being comparable to [B]).

For case (ii), the temperature dependence of c(T,x) is given by that of D_B,

$$D_B = D_\infty \exp(-E_d/kT) \tag{5}$$

where D_∞ is the diffusivity at infinite temperature and E_d is the activation energy for diffusion. In case (iii), also a possible variation of [B] with temperature needs to be accounted for and the deduced activation energy of c does not necessarily equal E_d.

IV. Experimental results

Figure 1 shows a representative selection of concentration-versus-depth profiles for the $Z_{1/2}$ level at $\sim E_C$- 0.70 eV after annealing at 1150 °C in O_2 and N_2 atmospheres. The concentration in the peak region is about 6×10^{14} cm^{-3} for the control samples (N_2 anneal) regardless of the annealing temperature and duration used, while in the oxidized sample [$Z_{1/2}$] decreases with increasing time. The profiles peak at a depth of $\sim$1.5 μm and exhibit a pronounced tail towards the surface, as anticipated after MeV ion implantation [7]. In addition to the decrease in absolute values also the shape of the profiles is altered during the oxidation showing a larger relative reduction in the surface tail than in the peak region.

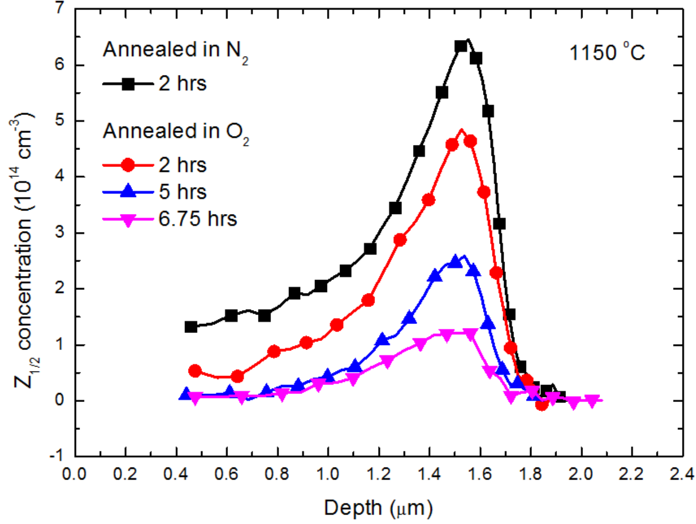

Figure 1: Concentration versus depth profiles of the $Z_{1/2}$ level, after annealing in O_2 and N_2 atmospheres at 1150 °C.

In Figure 2, the concentration of $Z_{1/2}$ at x=0.8 μm is plotted as a function of the oxidation time at 1050, 1100, 1125, 1150 and 1175 °C. In each case, the decay of [$Z_{1/2}$] exhibits an exponential dependence and the rate constant, c(T,x), increases strongly with temperature, cf. Eq. (2) with A = $Z_{1/2}$. Hence, the annihilation process of $Z_{1/2}$ obeys first-order kinetics and c(T,x) has been extracted at four different depths, x = 0.8, 1.0, 1.2 and 1.4 μm. The results are shown in Figure 2(b) as an Arrhenius plot with c(T,x) depicted versus the reciprocal absolute temperature; within the experimental accuracy, E_a stays constant as a function of x and a value of 5.4 $\pm$ 0.3 eV is obtained. However, the pre-factor, $c_0(x)$, decreases with increasing x and is reduced by a factor of two between x = 0.8 and 1.4 μm. The absolute values of c_0, i.e., the intercept with the ordinate when T approaches infinity, carry a significant uncertainty, but are in the range of 10^{13} - 10^{16} s^{-1}. Without oxidation, $Z_{1/2}$ persists up to temperatures of $\sim$2000 °C in irradiated samples [27] and it may even be thermally generated above $\sim$1700 °C [8] . An activation energy of $\sim$8 eV has been estimated for the annealing of $Z_{1/2}$ assuming dissociation [27]. Thus, during the oxidation E_a is lowered by $\sim$3 eV and dissociation can be ruled out as the controlling process. This conclusion is also substantiated by the variation of c(T,x) with x; for a first-order dissociation process c(T,x) depends only on T and not on x. Accordingly, the annihilation process of $Z_{1/2}$ is either of the type (ii) or (iii) discussed in section III. .

Figure 3 shows the total loss of $Z_{1/2}$ centers, determined by integration of the depth profiles, as a function of the thickness of the SiO_2 layer grown at 1050, 1100, 1125, 1150 and 1175 °C. The oxidation takes place in the parabolic time domain but for the temperatures and durations used the non-linearity is weak and a linear dependence holds with a high degree of accuracy [28].

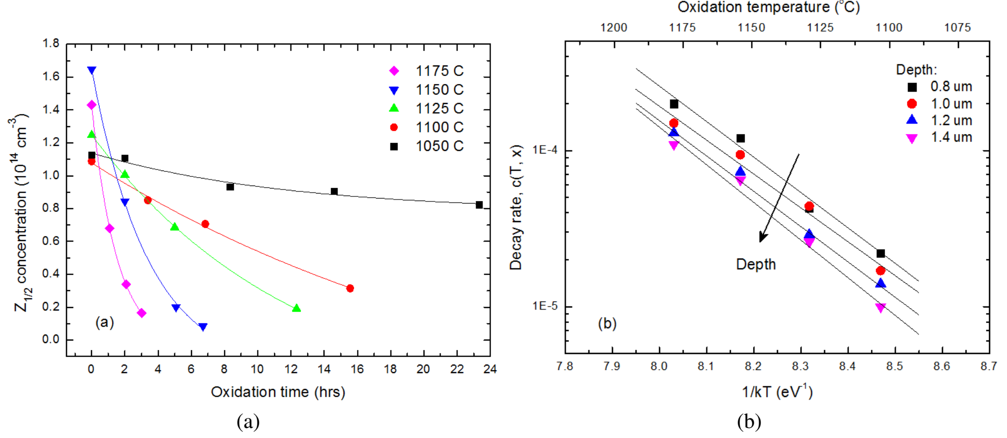

(a) (b)

Figure 2: a) The concentration of $Z_{1/2}$ at x=0.8 μm as a function of the oxidation time. The lines are exponential fits of the measured values and show a close agreement. (b) The exponential decay rate of $[Z_{1/2}]$ at x=0.8, 1.0, 1.2 and 1.4 μm versus the reciprocal absolute temperature. The decay rate decreases with x but the average activation energy stays constant at 5.4 $\pm$ 0.3 eV.

Figure 3 unveils a close proportionality with a slope having a tendency to increase with T, especially between 1125 and 1150 °C where the difference is a factor $\sim$2. These data demonstrate quantitatively the direct relation between the amount of oxidized Si atoms and the amount of annihilated $Z_{1/2}$ centers but also that the annihilation efficiency depends on T, i.e., it is not sufficient to consider only the thickness of the grown SiO_2 layer when estimating the amount of annihilated $Z_{1/2}$ centers.

V. Discussion

A. Model assumed in the simulations

The decreasing annihilation rate of $Z_{1/2}$ with increasing depth (Figs. 1 and 2) implies in-diffusion of an annihilating species from the surface, in accordance with previous findings in the literature [11, 12]. Hereafter, this species will be referred to as C_I and it is generated during the oxidation process. However, injection into the SiC bulk is not the only alternative for C_I competing reactions exist and their relative importance increases with decreasing temperature (Figure 3). These reactions include trapping of C_I in the SiO_2 layer and at the SiO_2 / SiC interface resulting in the formation of a Si-C-O interlayer and/or clusters of C [29]. Also out-diffusion of C_I through the surface may be considered but it is anticipated to decrease with t and no correspond-

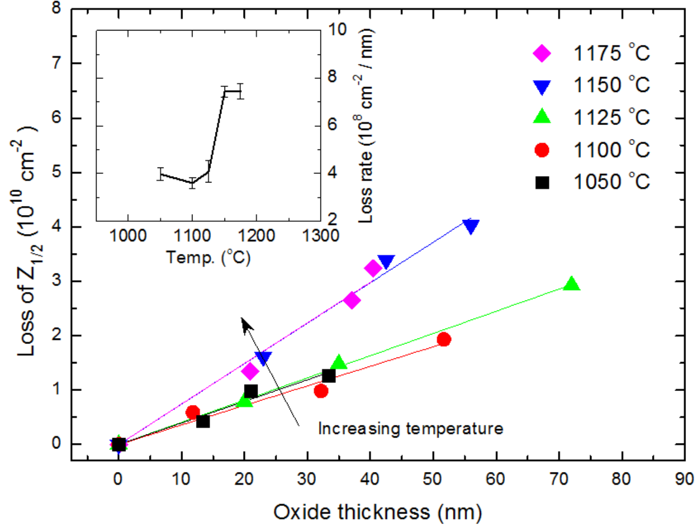

Figure 3: The loss of $Z_{1/2}$ per cm^2 as a function of the thickness of the grown SiO_2 layer. The inset shows the loss of $Z_{1/2}$ per nm of grown SiO_2 versus temperature.

ing increase in the annihilation efficiency of $Z_{1/2}$ is observed. Hence, as a first approximation the following reaction model has been assumed

$$C_i + Z_{1/2} \rightarrow \emptyset \tag{6}$$

$$C_I + C_I \rightarrow C_2 \tag{7}$$

where the latter reaction accounts for the trapping of C_I via formation of immobile carbon dimers (C_2), primarily at the SiC/SiO_2 interface but also in the SiO_2 and SiC layers. Further, $Z_{1/2}$ is regarded as immobile and applying Eq. (4), the differential rate equations for $Z_{1/2}$ and C_I become

$$\frac{\partial [Z_{1/2}]}{\partial t} = - 4\pi R D_{C_I} [C_I][Z_{1/2}] \tag{8}$$

$$\frac{\partial [C_I]}{\partial t} = g - D_{C_I} \frac{\partial^2 [C_I]}{\partial x^2} - 4\pi R D_{C_I} [C_I] \left([Z_{1/2}] + [C_I] \right) \tag{9}$$

g is the generation rate of C_I close the interface and put as,

$$g \begin{cases} > 0 & \text{for } 0 < x < 10 \text{ nm} \\ = 0 & \text{for } x > 10 \text{ nm} \end{cases} \tag{10}$$

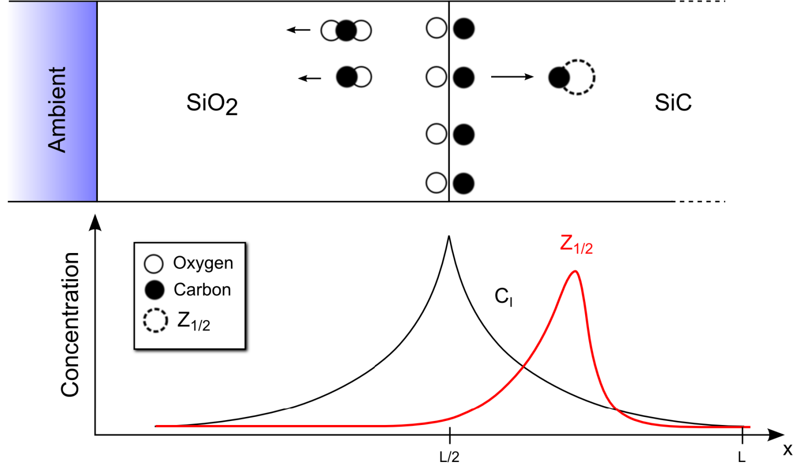

Figure 4: Schematic illustration of the model and sample structure assumed in the simulations.

The width of 10 nm reflects the extension of the Si-C-O transition layer and g has a time evolution in accordance with that of the growth rate of the SiO_2 layer [28]. D_{C_I} is given by

$$D_{C_I} = \begin{cases} 16 \times 10^{-12}\text{cm}^2/s & \text{(in SiO}_2\text{)} \\ \text{fitting parameter} & \text{(in SiC)} \end{cases} \tag{11}$$

where the value in SiO_2 is taken from Ref. [30]. For $[Z_{1/2}]$(T,x,t=0) the measured concentration-versus-depth profile in the control sample is used while $[C_I]$(T,x,t=0) is put equal to zero. The model is schematically illustrated by Figure 4 for an arbitrary time t. The SiO_2 / SiC interface is regarded as a reference plane at x=L/2 and the SiO_2 layer is held constant with a sufficient thickness (40 μm) to set $[C_I]$(T,x=0,t)=0 as a boundary condition. Further, both $[Z_{1/2}]$ and $[C_I]$ are vanishing in the SiC bulk (large x values).

B. Ultimate annihilation efficiency

In the ultimate limit of annihilation efficiency, every injected C_I contributes to the loss of $Z_{1/2}$, as assumed by the present authors in [12], and then the flux of C_I being emitted from the SiO_2 / SiC interface at a given T can be deduced from the total loss of $[Z_{1/2}]$ versus t, Figure 3. Such a treatment has been applied to all the experimental data for $[Z_{1/2}]$(T,x,t) and the extracted values of the flux were used as input to the simulations. D_{C_I} was treated as a fitting parameter and varied until an optimum agreement with the measured depth profiles of $[Z_{1/2}]$ was obtained. The values deduced for D_{C_I} are given in Figure 5 and similar to that found in [12], where only one temperature was studied (1150 °C), they suggest a rapid diffusivity on the order of 10^{-8} cm^2/s.

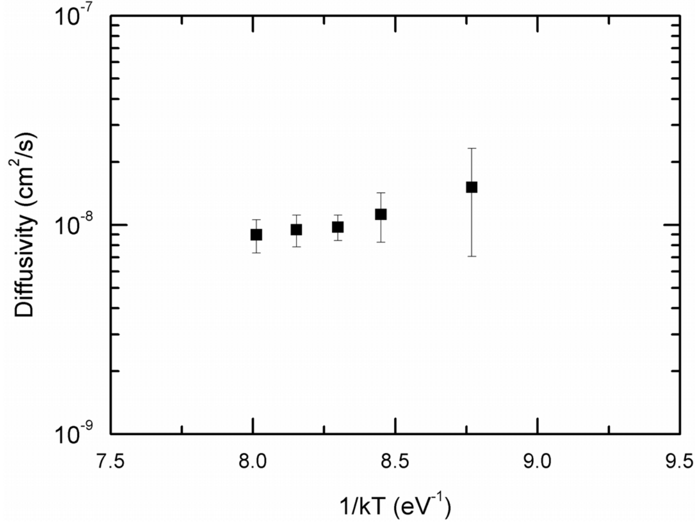

Figure 5: The diffusivity of C_I versus the reciprocal absolute temperature deduced under the assumption that every injected C_I contributes to the loss of $Z_{1/2}$.

The variation with T is weak and in fact, opposite to that anticipated for a thermally activated process, i.e., D_{C_I} decreases with increasing T. This suggests strongly that the basic assumption of an ultimate efficiency of the injected C_I's to annihilate $Z_{1/2}$ centers is not valid and a different approach with less efficient annihilation must be taken.

C. Extraction of relative C_I profiles and modelling of both $Z_{1/2}$(T, x, t) and C_I(T, x, t)

As shown by the experimental data, the annihilation of $Z_{1/2}$ exhibits first-order kinetics and the reaction process is either of type (ii) or (iii) (section III). Accordingly, from Eq. 8 the following relationship can be derived for c(x) at a given temperature,

$$c(x) = 4\pi R \mathrm{D}_{C_I}[C_I](x, t) \tag{12}$$

where the time dependence of $[C_I]$ is negligible (the explicit temperature dependence of the quantities in Eq. (12) has been omitted for ease of reading). C_I is injected from the oxidizing surface and the depth dependence of the decay rate of $Z_{1/2}$, i.e., c(T,x) in Figure 2(b), is due to the variation of $[C_I]$ with x. A large $[C_I]$ gives fast decay of $Z_{1/2}$ which therefore is maximal at the surface and decreases towards the bulk. The relative depth profile of $[C_I]$ ($[C_I]'$), e.g.,

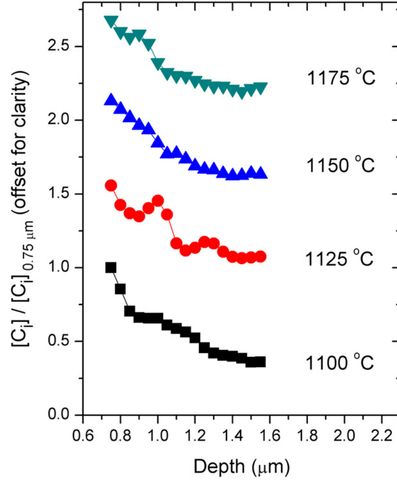

Figure 6: Depth profiles of $[C_I]$' extracted from Eq. (13) for oxidation at 1100, 1125, 1150 and 1175 °C. The profiles are offset along the y-axis to improve the readability.

normalized to $[C_I]$ at (or close to) the surface, can be extracted from Eq. (12) by realizing that:

$$[C_I]' = \frac{[C_I](x)}{[C_I](x_{surf}} = \frac{c(x)}{c(x_{surf}} \tag{13}$$

We have used x_{surf} = 0.75 μm which is the most shallow depth where $[Z_{1/2}]$ is sufficiently large for an accurate determination of c(x). The extracted distributions of $[C_I]$' are shown in Figure 6 and a clear decrease with x is revealed at all the oxidation temperatures employed. The distributions extend up to x=1.6 μm, i.e., just beyond the peak position of $[Z_{1/2}]$, whilst at larger depths the rapid decrease of $[Z_{1/2}]$ prevents an accurate extraction. The profiles of C_I' in Figure 6, and their negligible variation with t, imply one more criteria to be fulfilled by the simulations, in addition to the evolution of $[Z_{1/2}]$ with T, t and x. For each oxidation temperature and duration, g and D_{C_I} have been varied independently to fit both $[Z_{1/2}](x)$ and $[C_I]'(x)$ by solving Eqs. (8) and (9). The results of such a fitting procedure are illustrated in Figure 7 for oxidation at 1100 °C, where the squared sum of the difference between simulated and experimental data is depicted in D_{C_I}-versus-g plots for C_I' (Figure 7(a)) and $Z_{1/2}$ (Figure 7(b)). Corresponding results have also been obtained for the other temperatures (not shown). In the fitting, D_{C_I} was held constant as a function of t while g exhibited a weak decrease during the initial stages of t, in accordance with a parabolic time domain of the oxidation process. Further, in the SiO_2 layer D_{C_I} has been taken from Hijikata et al. [30] and is anticipated to have a low activation energy (∼0.5 - 0.6 eV), i.e., it stays almost constant in the temperature range studied. The absolute value of D_{C_I} in the SiO_2 layer carries, however, an uncertainty by a few orders of magnitude [31] and especially, higher values than that used in the simulations (16×10^{-12} cm^2/s), as suggested by Krafcsik et al. [32], shift the plots in Figure 7 to higher g values but with minor effects on their topology.

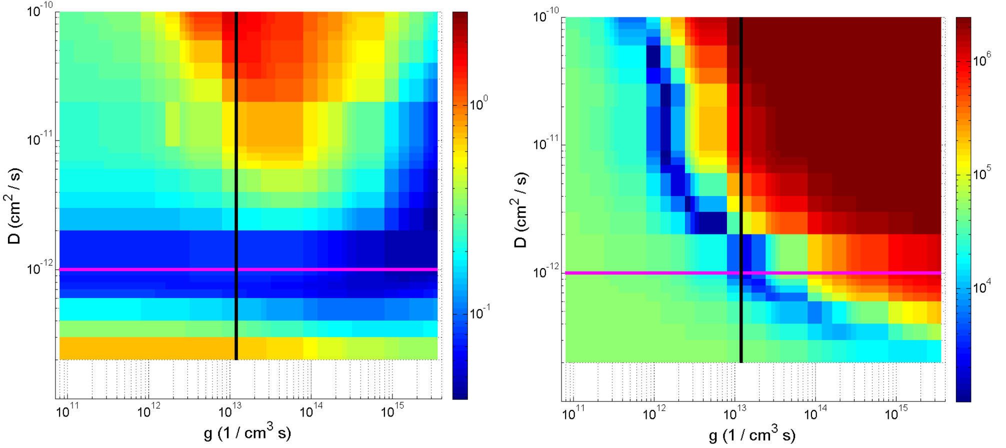

Figure 7: The squared deviation of the simulated data compared with the experimentally determined depth profiles of (a) C_I' and (b) $Z_{1/2}$. The intersection of the pink and black lines represents the best combination of D_{C_I} and g.

As unveiled by Figure 7(a), the solutions for C_I' are rather selective with respect to D_{C_I} but not to g. However, the solutions for $Z_{1/2}$ are selective to both g and D_{C_I}, Figure 7(b), and combining the results for C_I' and $Z_{1/2}$ one obtains $D_{C_I} \approx 1.0 \times 10^{-12}$ cm^2/s and g $\approx 1 - 2 \times 10^{13}$ $cm^{-3}s^{-1}$ as the optimum values at 1100 °C. These values are not fully unique but are estimated to be valid within a factor of two for D_{C_I} and less than a factor of 10 for g (albeit subject to change depending on D_{C_I} in SiO_2 as discussed above). Figure 8 shows an Arrhenius plot of the g and D_{C_I} values determined at 1100, 1125, 1150 and 1175 °C where also the physical condition of an activation energy (E_a) of g equal to, or above, that of the oxidation process has been imposed. Indeed, E_a(g) equals ∼3.3 eV which is slightly higher than the value of ∼3.1 eV obtained for the oxidation rate; the latter value is also corroborated by previous reports in the literature [28]. The values in Figure 8 give excellent agreement between the simulations and the experimental data of [$Z_{1/2}$](T,x,t) and [C_I]'(T,x,t), as demonstrated in Figure 9(a) and 9(b) for 1100 and 1150 °C, respectively.

E_a(g) ≈ 3.3 eV implies a lowering by at least 4 eV for the generation of 'free' C_I's at the SiO_2 / SiC interface compared to the formation energy estimated for C_I in bulk SiC under equilibrium conditions [33] and it illustrates the strong 'catalytic effect' of the oxidation process. $E_a(D_{C_I})$ ≈ 3.0 eV is ascribed to the migration energy of the 'free' C_I's injected to the SiC layer; this value is ∼2.0 eV higher than the migration barrier predicted by Bockstedte et al. [33] for C_I in the energetically favorable split-interstitial configuration. The calculations in Ref. [33] were performed for the 3C-polytype but are expected to provide a first insight also into the diffusion processes in other polytypes, like 4H. The difference of ∼2.0 eV may indicate that the 'free' C_I's have to surmount an additional energy barrier at the SiC/SiO_2 interface before migrating rapidly

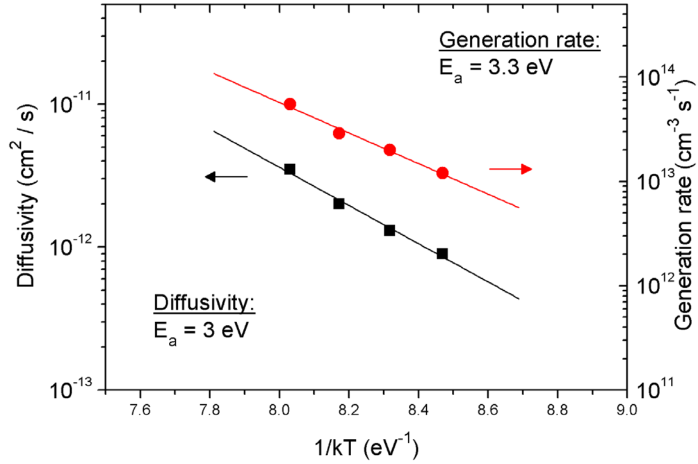

Figure 8: The values of D_{C_I} and g extracted from the simulations versus the absolute reciprocal oxidation temperature.

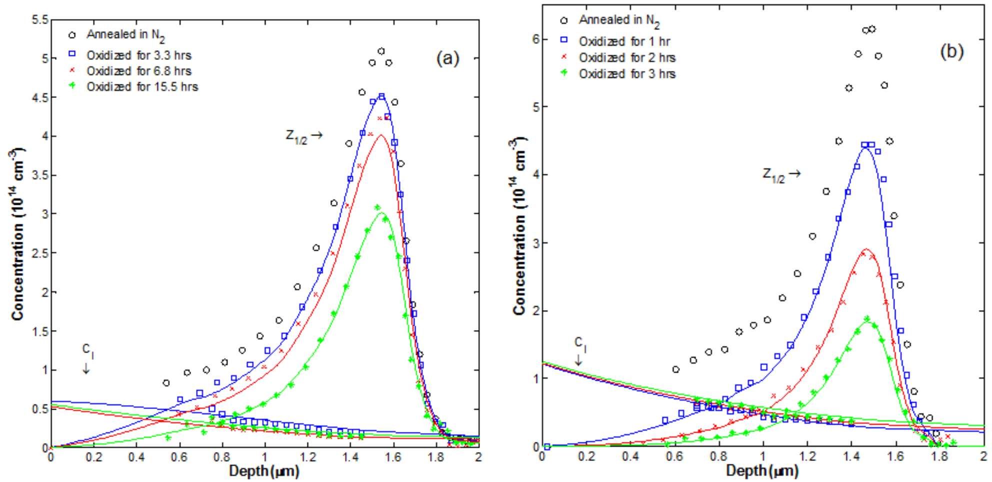

Figure 9: The temporal evolution of the $Z_{1/2}$ and C_I concentration-versus-depth profiles at (a) 1100 °C and (b) 1175 °C, with activation energies of 3.0 eV for D_{C_I} and 3.3 eV for g. [C_I] stays nearly time-independent through-out the $Z_{1/2}$ profiles, yielding first-order annealing kinetics of $Z_{1/2}$ at a given depth.

into the SiC layer. On the other hand, it can also be noted that self-diffusion experiments of ^{12}C and ^{13}C in intrinsic 4H-SiC yielded an activation energy for the diffusion of C which as ∼1.5-2.0 eV higher than that obtained in Ref. [33] for C_I.

The sum of E_a(g) and E_a(D_{C_I}) equals ∼6.3 eV which is ∼0.9 eV higher than the value extracted for the decay rate c of $Z_{1/2}$ Figure 2(b). This shows a weaker increase of [C_I] with temperature (lower E_a) than of g, as c is directly proportional to [C_I] for a given D_{C_I}, Eq. (12). However, the shape of the [C_I]-versus-depth profiles stays approximately the same for the different T's, in accordance with the [C_I]' profiles in Figure 6. In spite of the annihilation with $Z_{1/2}$, [C_I](T,x,t) remains almost constant as a function of t, i.e., the flux of C_I from the oxidizing surface is sufficiently high to main a steady-state concentration. In fact, the weak time dependence of [C_I](T,x,t) is a main reason for the apparent first-order annealing kinetics of $Z_{1/2}$ at a given depth, and referring to section III, the 'exotic' case (iii) applies. The implantation-induced distribution of [$Z_{1/2}$] can be regarded as a trapping (or barrier) layer for C_I to penetrate before reaching the bulk and the evolution of [$Z_{1/2}$](T,x,t) is a monitor of the flux of C_I's.

Finally, it should be emphasized that g is minute relative to the rate of oxidized Si atoms (or equivalently, the generation rate of C atoms without bonds to Si) at the SiO_2 / SiC interface with a difference of 5-6 orders of magnitude. Hence, oxidation-induced injection of C_I is a process with crucial impact on bulk defects but not the prevailing one at the SiO_2 / SiC interface. Moreover, on the basis of the fitted g values a few percent of the injected C_I's are estimated to annihilate with $Z_{1/2}$, which is substantially lower than the ultimate limit of 100 % discussed, and ruled out, in section V.A.

VI. Conclusions

At a given depth x, oxidation-induced annihilation of $Z_{1/2}$ centers in the parabolic time regime obeys first-order kinetics with a rate constant c(T,x) having an activation energy of ∼5.4 eV. The pre-exponential factor of c(T,x) decreases with increasing x, which is ascribed to a decreasing steady-state concentration of the annihilating species, C_I, injected from the SiO_2 / SiC interface. The experimental data for $Z_{1/2}$(T,x,t) and [C_I]'(T,x,t) can be quantitatively and accurately described by a kinetic model where g is essentially proportional to the oxidation rate and the diffusion of C_I is fast while $Z_{1/2}$ is immobile, as corroborated by experimental data for control samples annealed in N_2 atmosphere. D_{C_I} has an activation energy of ∼3.0 eV, presumably reflecting the migration barrier of C_I and possibly some addition from a barrier to be surmounted at (or in the vicinity of) the SiO_2 / SiC interface before reaching the SiC layer. The steady-state concentration-versus-depth profiles of C_I are rapidly established and this is a major reason for the apparent first-order annealing kinetics of $Z_{1/2}$ at a given x. Moreover, the total loss of $Z_{1/2}$ centers is proportional to the thickness of the SiO_2 layer grown. However, the proportionality constant (annihilation efficiency) decreases with decreasing temperature due to a lower D_{C_I}. Hence, when estimating the amount of annihilated $Z_{1/2}$ centers it is not sufficient to consider the

SiO_2 layer thickness only but also D_{C_I} must be taken into account.

Acknowledgments

Fruitful discussions with Dr Hijikata are highly appreciated and financial support from the Norwegian Research Council (FRINAT program) is gratefully acknowledged.

References

[1] M. S. Janson, M. K. Linnarsson, A. Hallén, B. G. Svensson, N. Nordell. *Applied Physics Letters.* 2000;76:1434.

[2] L. J. Kroko, A. G. Milnes. *Solid-State Electronics.* 1966;9:1125–1134.

[3] R. J. Trew, J.-b. Yan, P. M. Mock. *Proceedings of the IEEE.* 1991;79.

[4] C. Hemmingsson, N. T. Son, O. Kordina, et al. *Journal of Applied Physics.* 1997;81:6155.

[5] T. Dalibor, G. Pensl, T. Kimoto, et al. *Diamond and Related Materials.* 1997;6:1333–1337.

[6] P. B. Klein, B. V. Shanabrook, S. W. Huh, et al. *Applied Physics Letters.* 2006;88:52110.

[7] G. Alfieri, E. V. Monakhov, B. G. Svensson, A. Hallen. *Journal of Applied Physics.* 2005;98:113524.

[8] B. Zippelius, A. Glas, H. B. Weber, G. Pensl, T. Kimoto, M. Krieger. *Mat. Sci. Forum, in press (2012).* .

[9] L. Storasta, H. Tsuchida. *Applied Physics Letters.* 2007;90:062116.

[10] T. Hiyoshi, T. Kimoto. *Applied Physics Express.* 2009;2:41101.

[11] T. Hiyoshi, T. Kimoto. *Applied Physics Express.* 2009;2:91101.

[12] L. S. Lovlie, B. G. Svensson. *Applied Physics Letters.* 2011;98:052108.

[13] N. T. Son, X. T. Trinh, L. S. Lø vlie, et al. *To be published.* 2012.

[14] L. Storasta, J. P. Bergman, E. Janzén, A. Henry. *Journal of Applied Physics.* 2004;96:4909.

[15] J. Zhang, L. Storasta, J. P. Bergman, N. T. Son, E. Janzen. *Journal of Applied Physics.* 2003;93:4708.

[16] C. G. Hemmingsson, N. T. Son, A. Ellison, J. Zhang, E. Janzén. *Physical Review B.* 1998;58:R10 119.

[17] T. Kimoto, S. Nakazawa, K. Hashimoto, H. Matsunami. *Applied Physics Letters.* 2001;79:2761.

[18] K. Danno, T. Kimoto. *Journal of Applied Physics.* 2006;100:113728.

[19] T. Kimoto, K. Hashimoto, H. Matsunami. *Japanese Journal of Applied Physics.* 2003;42:7294–7295.

[20] T. Eberlein, C. Fall, R. Jones, P. Briddon, S. Öberg. *Physical Review B.* 2002;65:1–4.

[21] T. Hornos, A. Gali, B. G. Svensson. *Materials Science Forum.* 2011;679-680:261–264.

[22] L. Torpo, M. Marlo, T. E. M. Staab, R. M. Nieminen. *Journal of Physics: Condensed Matter.* 2001;13:6203–6231.

[23] K. Kawahara, J. Suda, G. Pensl, T. Kimoto. *Journal of Applied Physics.* 2010;108:033706.

[24] B. G. Svensson, K.-H. Ryden, B. M. S. Lewerentz. *Journal of Applied Physics.* 1989;66:1699.

[25] B. G. Svensson, J. L. Lindström. *Physical Review B1.* 1986;34:8709.

[26] T. R. Waite. *Physical Review.* 1957;107:463–470.

[27] G. Alfieri, E. V. Monakhov, B. G. Svensson, M. K. Linnarsson. *Journal of Applied Physics.* 2005;98:43518.

[28] Y. Song, S. Dhar, L. C. Feldman, G. Chung, J. R. Williams. *Journal of Applied Physics.* 2004;95:4953.

[29] S. T. Pantelides, S. Wang, A. Franceschetti, et al. *Materials Science Forum.* 2006;527-529:935–948.

[30] Y. Hijikata, H. Yaguchi, S. Yoshida. *Applied Physics Express.* 2009;2:021203.

[31] Y. Hijikata. *Private communication.* .

[32] O. H. Krafcsik, G. Vida, I. PÓcsik, K. V. Josepovits, P. Deák. *Japanese Journal of Applied Physics.* 2001;40:2197–2200.

[33] M. Bockstedte, A. Mattausch, O. Pankratov. *Physical Review B.* 2003;68:205201.

Paper III

Paper IV

Paper V

Long range lateral migration of intrinsic point defects in n-type 4H-SiC

L. S. Løvlie, L. Vines and B. G. Svensson
Department of Physics/Centre for Materials Science and Nanotechnology
P.O. Box 1048 Blindern, University of Oslo, N-0316 Oslo, Norway

Abstract

The lateral distributions of intrinsic point defects in n-type (0001) 4H-SiC have been investigated following room temperature irradiation with a focused beam of 10 keV protons. Laterally resolved deep level transient spectroscopy (DLTS) measurements reveal that the well-known and prominent $Z_{1/2}$ and $S_{1/2}$ centers display lateral diffusion lenghts on the order of one millimeter with negligible (if any) motion parallel to the direction of the c-axis. The migration occurs only in the presence of excess charge carriers generated during the proton irradiation and no further motion takes place even under subsequent optical excitation of high intensity. Assuming one-dimensional geometry, an effective defect diffusivity in excess of 10^{-6} cm^2/s is deduced by numerical modelling of the experimental data, corresponding to an energy barrier for migration of ~0.2 eV. Possible mechanisms for the rapid migration, invoking charge carrier recombination as a necessary condition, are discussed, and especially, an association with the glide of partial dislocations along the (0001) basal plane is scrutinized in some detail.

Introduction

Knowledge about defect evolution and diffusion in conjunction with activation of dopants and carrier lifetime control is among the most important reasons for studying intrinsic point defects in SiC. Several of the defects have, indeed, a detrimental effect on the concentration and lifetime of the charge carriers. In particular, the omnipresent $Z_{1/2}$ defect in 4H-SiC, exhibiting an acceptor level at ~0.7 eV below the conduction band edge (E_C) [1,2], has been identified to limit the bulk minority carrier lifetime in 4H-SiC bipolar devices [3]. $Z_{1/2}$ anneals out through multiple stages over a broad temperature range, and it persists up to temperatures as high as ~2000 °C [4]. The multi-stage annealing implies reactions with other defects/impurities of limited concentration and which become mobile as the temperature

increases until ultimately $Z_{1/2}$ itself becomes unstable. Moreover, it has previously been reported that certain point defects can migrate distances of several hundreds of micrometers during electron irradiation, as studied by photoluminescence (PL) [5,6] and deep level transient spectroscopy (DLTS) [7]. The migration occurs laterally and an adverse effect on the use of implantation/irradiation for selective area doping and life-time control is anticipated. Specifically, carbon interstitials (C_I) were considered to migrate long distances, whereas Si vacancies largely remained confined within the directly irradiated volume[5,6]. Since the so-called $S_{1/2}$ levels at E_c – 0.45 eV and E_c – 0.72 eV [8] and the $Z_{1/2}$ level were observed far away from the directly irradiated area [7], it was suggested that C_I is involved in the formation of these centers. This was further supported by first-principles studies of antisite pairs in 4H-SiC, which unveiled that C_I (but not the carbon vacancy, V_C) can act as a catalyst for their formation during ionizing conditions, such as irradiation with energetic electrons and ions[9].

In Refs.[6,7]**,** it was speculated that the C_I's are able to migrate long distances through a diffusion process driven by successive changes in charge state, known as the Bourgoin-Corbett mechanism if no thermal activation is required (athermal process)[10] while a more normal ionization-enhanced (electronically stimulated) mechanism yields a lowering of the thermal energy required for motion. In the latter case, the ionization changes C_I from a rather immobile charge state with high energy barrier for migration to one which is relatively mobile with low migration barrier, i.e., the process remains thermally activated but with a reduced energy and the potential minimum position of C_i in the lattice is the same for the different charge states. In the former case, the potential minimum position of one charge state occurs at the saddle-point position for migration of the other charge state and vice versa; thus, by cycling between the charge states the defect can move through the lattice without any thermal energy required. Several defects in other semiconductor materials have been considered to exhibit ionization-enhanced motion, like the self-interstitial in silicon[10], the zinc interstitial in ZnSe [11,12] and the oxygen dimer in silicon[13,14]. Especially, the latter one has been investigated extensively during the past decade since it is proposed to play a key role for light induced degradation of the minority carrier lifetime in silicon solar cells through formation of a substitutional boron – interstitial oxygen dimer complex, although this hypothesis has very recently been refuted[15].

In the present work, we have studied in detail the lateral distribution of the $Z_{1/2}$ and $S_{1/2}$ defects in 4H-SiC following focused proton beam irradiation at room temperature (RT). Dramatic effects are observed with lateral migration distances on the order of millimeters. The experimental data are modelled assuming one-dimensional Fickian diffusion and effective diffusivity values are extracted. Possible mechanisms for the long distance migration, which is highly anisotropic along the (0001) basal

plane, are discussed. In particular, ionization-enhanced diffusion of the $Z_{1/2}$ and $S_{1/2}$ centers is ruled out as the only cause and arguments for the involvement of recombination-enhanced migration of extended defects, like gliding of partial dislocations along the basal plane, are put forward.

Experiment

Schottky barrier diodes (SBDs) were formed by electron-beam deposition of 100 nm thick circular Ni contacts (diameter = 400 µm) on n-type nitrogen doped (0001) 4H-SiC samples (purchased from Cree, Inc.) having a 10 µm thick epitaxial layer grown on the Si-face. The effective carrier concentration in the epitaxial layer was about 3×10^{15} cm^{-3}, while the substrate doping was about 10^{18} cm^{-3}. The concentrations of the $Z_{1/2}$ and $S_{1/2}$ defects were monitored by deep level transient spectroscopy (DLTS). The measurements were performed using an improved version of a custom made setup equipped with a HP 4280A capacitance bridge, described in detail elsewhere [16], and a Semilab DLS83 setup, both having liquid nitrogen cryostats. Some selected measurements with high energy resolution were performed using a Boonton 7200 capacitance bridge and a closed-cycle helium cryostat.

Prior to the formation of SBDs and proton irradiation, the samples were thermally oxidized in dry O_2

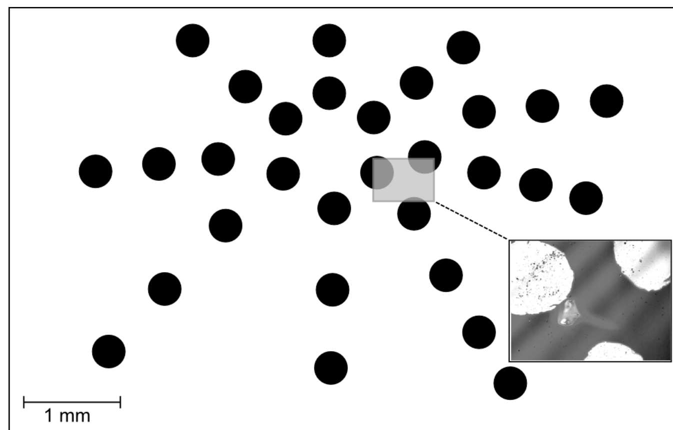

Fig. 1: An illustration of the layout of SBDs on a sample. (inset) Close-up of the area indicated by the small rectangle, displaying the irradiated area and the closest contacts. The beam had an approximate diameter of 100 µm, with a tail towards the right in the image.

at 1150 °C for 5 hrs and the resulting oxide layer was then removed in diluted HF. This procedure efficiently removes all deep-level defects with states in the upper half of the band gap [17,18], thereby enhancing the sensitivity of the $Z_{1/2}$ and $S_{1/2}$ levels formed during the proton irradiation. This holds especially for the $Z_{1/2}$ level which is already present with a concentration of ~10^{12} cm^{-3} in the as-grown material. The oxidation resulted in a 50 nm thick layer of SiO_2, indicating that a so-called trap eliminated depth of about 6 μm was obtained [18]. Except for enhancing the sensitivity, the oxidation has no influence on the observed long distance defect migration[19]. The proton irradiations were performed in a Cameca IMS 7f micro-analyzer, enabling positioning of the beam spot with an accuracy of less than 20 μm, using an energy of 10 keV and a focused beam with a diameter of ~100 μm. The proton dose was about 4 × 10^{18} cm^{-2}, corresponding to an irradiation time of 1 h for a beam current of 10 nA, and the beam was positioned ~50 μm away from the periphery of the nearest SBD. The irradiations were conducted at nominal room temperature with no significant heating of the samples.

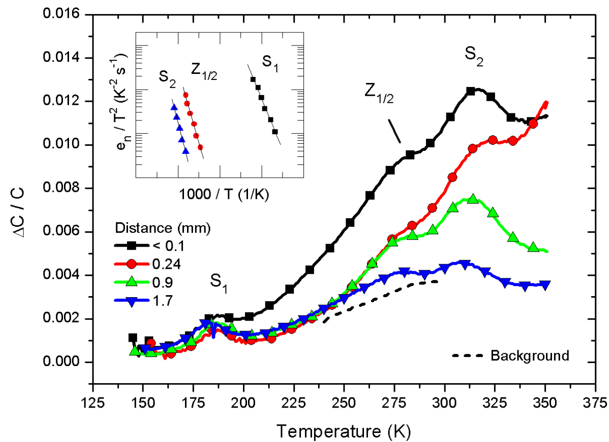

Fig. 2: DLTS spectra recorded before and after irradiation, showing the decrease in peak amplitudes with increasing distance from the irradiated area. Inset: Arrhenius plots for the DLTS peaks, showing that their emission rates (e_n), corrected for the temperature dependence of the electron velocity and of the density of states in the conduction band, depend exponentially on temperature, despite being rather broad. The DLTS spectra have a rate window of $(640\ ms)^{-1}$ and are deduced using a weighting function of lock-in type.

Results

A schematic illustration of the layout of SBDs on a sample is shown in Fig. 1. The contacts are arranged in a radial pattern, such that any possible dependency on the crystal orientation in the basal plane could be revealed. The beam was positioned in the region with the shortest distance between the 3 closest contacts to maximize the resolution for short migration distances, where the concentration is expected to change most rapidly. The irradiated area is visible due to discoloration caused by damage and strain in the irradiated region, illustrating the shape of the beam spot. The lateral distance from the position of the beam to the center of each SBD varied from ~250 µm up to 3.5 mm.

DLTS spectra were measured in the temperature range 150 – 350 K before and after irradiation, as shown in Fig. 2 for SBDs with increasing distance to the irradiated area. The DLTS peaks are broad but exhibit single-exponential Arrhenius behavior as shown in the inset, indicating that they are due to overlapping (discrete) energy levels. The properties of the detected peaks are summarized in Table I. The projected range of the 10 keV protons is ~100 nm according to simulations using the TRIM software [20] whilst the depletion region at zero-bias voltage extends almost 1 µm below the Ni/SiC interface. Accordingly, a forward bias of +1.5 V was used during the DLTS pulsing (duration 50 ms), with a quiescent reverse bias of -1.0 V, in order to probe the proton-induced defects in the vicinity of the surface. No DLTS signals were detected using a pulsing bias of 0 V, showing that all of the detected defects occur no deeper than 1 µm below the surface. As illustrated in Fig. 2, a broad and featureless background signal exists prior to the irradiation originating from near-surface defects with rather deep states responding primarily at temperatures above 200 K.

Trapping center	**$E_C - E_t$ (eV)**	**σ_a (cm^2)**
S_1	0.44 ± 0.01	3×10^{-14}
$Z_{1/2}$	0.65 ± 0.03	10^{-14}
S_2	0.77 ± 0.05	10^{-14}

Table I: The band gap position (± 1 standard deviation) and apparent capture cross section (σ_a) of the trapping centers which are detectable in Fig. 2.

Three levels are clearly discernible in Fig. 2; the S_1 level with a band gap position of E_C – 0.44 eV, $Z_{1/2}$ at E_C – 0.65 eV and the S_2 level at approximately E_C – 0.77 eV. Employing a weighting function of GS4 type [21] with higher energy-resolution (but also more noise) than the one of lock-in type used in Fig. 2, the

overlap between the three DLTS peaks becomes negligible (not shown). There is also at least one more level present just outside the measurement range ending at 350 K; this level was, however, not fully recorded in order to avoid unintentional annealing during the measurements. The DLTS peaks are quite broad, which is usually the case when monitoring the directly irradiated area immediately after bombardment with energetic electrons and ions at RT and before any annealing [22]. The identity of the $Z_{1/2}$ level has been discussed extensively in the literature for almost 15 years [2,23–30] and it is generally agreed to be C-related, but no full consensus has been reached on the atomic structure. The S_1 and S_2 levels are considered to be due to different charge states of the same defect center, since they frequently appear with similar concentrations after MeV electron and ion irradiation, anneal out in a close to 1:1 correspondence, and the shallowest level, S_1, exhibits a considerably smaller electron capture cross section than S_2[8]. The fact that the apparent capture cross section, σ_a, has comparable values for S_1 and S_2, Table I, implies a substantial entropy term (~4x10^{-4} eV/K) for the S_1 charge state transition[8].

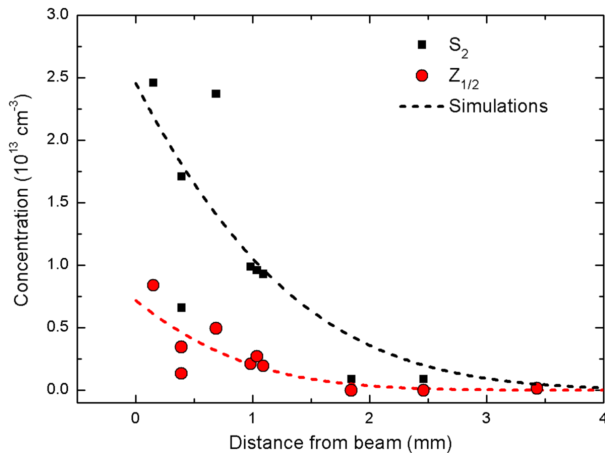

Fig. 3: Concentration versus distance from the irradiated area for the $Z_{1/2}$ and S_2 levels (revealed in Fig. 2). The DLTS background signal has been subtracted and one-dimensional diffusion has been assumed to fit the experimental data.

The lateral distributions of the concentration of the $Z_{1/2}$ and S levels were mapped using 10 SBDs with increasing distance to the directly irradiated area and the results, corrected for the background contribution prior to irradiation, are depicted in Fig. 3. The distance is determined from the center of

each SBD, and the data show that the average concentration of $Z_{1/2}$ and $S_{1/2}$, in the monitored depth interval, decrease with increasing distance. Although the spacing and size of the contacts in comparison to the observed diffusion lengths allow only limited resolution in a given direction, no dependence on the crystal orientation could be detected. The decrease takes place over distances of ≤2 mm before reaching the detection limit of ~$1x10^{12}$ cm^{-3}. Annealing for 1h at 250 °C in dry air reduces the absolute concentration values by ~50 %, without affecting the shape of the lateral distribution, and after 2 hrs they are below the detection limit. Results reported in Ref. [19] from an independent experiment, where the $Z_{1/2}$ concentration was monitored at a fixed distance from the irradiated area, agree closely with the corresponding values in Fig. 3 demonstrating a high reproducibility of the experiments.

The data for the $Z_{1/2}$ and S_2 levels in Fig. 3 have been modelled assuming one-dimensional diffusion with a constant diffusivity, as described in detail in the following discussion section. The lateral diffusion length, defined as the distance from the irradiated area where the concentration is reduced to 1/e, becomes approximately 0.8 mm for $Z_{1/2}$ and 1.1 mm for S_2.

Discussion

The experimental data in Fig. 3 are compared with simulations employing the diffusion equation,

$$\frac{\partial N_t}{\partial t} = D_{eff} \frac{\partial^2 N_t}{\partial x^2} \qquad (1)$$

where N_t is the defect concentration, D_{eff} is the effective diffusivity at RT (considered to be constant as a function of time and distance) and x is the lateral distance from the irradiated area. The fitting was accomplished by varying D_{eff} and the generation rate of defects, J (in units of defects/cm^2s). The generation rate J is estimated according to Fick's first law, which was used as the natural boundary condition at the area irradiated directly by the beam,

$$J(x = 0, t) = -D_{eff} \left(\frac{\partial N_t}{\partial x}\right)_{x=0}. \qquad (2)$$

The boundary condition at large distances from the directly irradiated area is a vanishing defect concentration ($N_t(x=\infty,t) = 0$), in accordance with the experimental data showing no defect concentration above the detection limit after oxidation and prior to irradiation.

The time of diffusion was put equal to the irradiation time (1 h), as substantiated by the fact that no further migration was observed after termination of the irradiation; the measured defect distributions remained constant for >6 months after irradiation keeping the samples at RT. D_{eff} and J were varied over a broad range and Eq. (1) was solved numerically for each set of (D_{eff}, J) until the values yielding the least squared error were found. In the case of $Z_{1/2}$, the best fit was obtained for $D_{eff} = 2 \times 10^{-6}$ cm^2/s and J ≈ 3 × 10^{10} cm^{-2} s^{-1}, while for S_2 the corresponding values were $D_{eff} = 4 \times 10^{-6}$ cm^2/s and J ≈ 2.9 × 10^{11} cm^{-2} s^{-1}. These diffusivities correspond to an energy barrier for migration on the order of 0.2 eV assuming a pre-exponential factor with a typical value of 10^{-2} – 10^{-3} cm^2/s. The migration parameter values extracted from the simulations are summarized in Table II.

Defect	D_{eff} (10^{-6} cm^2/s)	J (10^{11} cm^{-2} s^{-1})	Migration length (mm)
$Z_{1/2}$	2	0.3	0.8
S_2	4	2.9	1.1

Table II: Survey of the parameters for defect migration as extracted from solving Eq. (1) and fitting the experimental data for $Z_{1/2}$, and S_2.

Here, it should be emphasized that the extracted values for J do not account for defects trapped within the directly irradiated volume but do account for dynamic annealing (self-recombination); assuming a threshold energy of 20 eV for displacement of C and Si atoms and neglecting dynamic annealing, the total generation rate of V_C, C_I, V_{Si}, and Si_I, becomes ~10^{16} cm^{-2}s^{-1} for the experimental conditions used, according to an estimate based on TRIM calculations [20]. If ~1-3 % of the defects survive dynamic annealing [31], this estimate implies that <1 % of the surviving defects escape the directly irradiated volume and display long distance migration. This can perhaps be regarded as a small fraction but for sufficiently high doses of ion implantation (equivalent to >10^{16} H/cm^2 in terms of damage formation), detrimental effects may be expected on the minority carrier lifetime in areas located several hundreds of µm away from the directly implanted one.

The values deduced for D_{eff} are high and imply rapid migration of the species involved. The process is highly anisotropic with respect to the c-plane and only a very minor (if any) migration takes place along the direction parallel to the c-axis. Further, simultaneous irradiation is a necessary condition for the migration to occur and as discussed in Refs. [6,7,19], it is tempting to invoke ionization-enhanced motion of point defects as a possible cause for the observed effect. According to results from TRIM calculations

[20], one 10-keV-proton gives on average rise to ~2000 electron-hole pairs (EHP), assuming an average ionization energy of ~5.0 eV to generate an EHP in 4H-SiC [32]. If the minority carrier life time is put equal to 0.1 μs in the irradiated volume, i.e., about a factor 10 lower than that in as-grown high-purity epitaxial layers, and the carrier diffusivity is taken as ~1 cm^2/s (also about a factor 10 lower than in undamaged epitaxial layers), one obtains a carrier diffusion length of a few μm and a steady-state-density of ~10^{15} EHP/cm^3 during the irradiation. This density is of the same order of magnitude as the free electron concentration in the epitaxial layer suggesting that the availability of holes is a limiting factor for the migration process.

In principle, the migrating species may be the $Z_{1/2}$ and $S_{1/2}$ defects themselves, one (or more) of their constituents or a 'catalyst' species emerging from the directly irradiated volume and reacting with C/Si atoms in the unirradiated volume. The $Z_{1/2}$ center is commonly agreed on to be C-related [24–27,29], and an obvious candidate for the rapidly migrating species is C_I [6,7]; in fact, first-principles density calculations by Eberlein et al., [9] show that the atomic structure of C_I, as well as of Si_I, is charge state dependent and migration can be enhanced by ionizing radiation. In particular, a mechanism for the production of antisite defects in 4H-SiC has been predicted where the supply of excess holes during irradiation of n-type material is decisive. If a C_I is generated and migrates to a Si site, the reaction $(C_I)_{Si} \rightarrow C_{Si} + Si_I$ is endothermic by ~5.9 eV for neutral defects and will not occur. However, if two holes are trapped by $(C_I)_{Si}$ the reaction becomes endothermic by only 0.6 eV, according to defect formation energies, and will take place with a substantial rate at RT assuming negligible additional reaction barriers. After rapid neutralization of the ejected Si_I^{2+} by capturing of two electrons, it can migrate to a C site and by capturing of one hole the reaction $(Si_I)_C \rightarrow Si_C + C_I$ is endothermic by only ~0.2 eV relative to 1.8 eV for neutral defects.

Interestingly, the reaction enthalpies estimated by Eberlein et al.[9] are rather close to the migration barrier values extracted from the present experiment and may be regarded as an argument in favour of ionization-enhanced motion of C_I. On the other hand, the diffusion lengths of ~1 mm for $Z_{1/2}$ and $S_{1/2}$ in Fig. 3 are at least one order of magnitude higher than the average charge carrier diffusion length anticipated in epitaxial 4H-layers, suggesting that ionization-enhanced motion of C_I plays a limited role. Furthermore, exposure of the proton-irradiated samples to UV-irradiation, from a pulsed laser operating at 372 nm wavelength or a Hg lamp (output power centered around 365 nm wavelength), for a duration of 24 h and a steady-state injection of 10^{15} EHP/cm^3 did not cause any measurable diffusion of $Z_{1/2}$ and $S_{1/2}$. In addition, the pronounced anisotropy of the defect migration along the c-plane is not readily accounted for by ionization-enhanced motion of C_I.

The DLTS peaks in Fig. 2 are broad and do not originate from well-defined (unperturbed) but rather distorted $Z_{1/2}$ and $S_{1/2}$ centers. Similar spectra are also commonly found after irradiation with MeV ions or electrons at RT when monitoring the directly irradiated area[22], and the broadening has been attributed to a dense local elastic energy deposition by these projectiles (and their recoils) causing a distorted crystal structure in the vicinity of $Z_{1/2}$ and $S_{1/2}$. Such an origin of the distortion is not likely to hold for the present experiment where the defects are located several hundreds of μm away from the directly irradiated area and the shape of the peaks does not exhibit any variation with the migration distance. Here, it can also be noted that the peak amplitudes of S_1 and S_2 in Fig. 2 display a large deviation from a one-to-one correspondence, in contrast to that found in Ref. [8] and contradicting the main argument for assigning the two levels to different charge states of the same defect center. However, in analogy with the deviation from a one-to-one relation between the DLTS peak amplitudes of the singly and doubly negatively charged divacancy center in ion-bombarded silicon crystals [31,33,34], the present results for S_1 and S_2 imply a high local concentration of defects leading to volumes with partial compensation and depletion of free electrons, preventing complete filling of the shallow S_1 level during DLTS pulsing. In fact, the collected amount of information from the DLTS data, e.g., the broad $Z_{1/2}$ and $S_{1/2}$ peaks relative to those of isolated point defects, that the $Z_{1/2}$ and $S_{1/2}$ peaks remain broad several hundreds of μm away from the irradiation volume, the strong deviation from a one-to-one relation between the S_1 and S_2 peak amplitudes, and the highly anisotropic motion of $Z_{1/2}$ and $S_{1/2}$ along the (0001) basal plane with negligible migration parallel to the c-axis, provide compelling evidence for the involvement of extended defects (distorted crystal structure) in the long-distance migration of $Z_{1/2}$ and $S_{1/2}$, and a possible scenario is outlined below.

About 10 years ago, 4H-SiC PiN diodes were found to degrade during forward-bias operation when an electron-hole plasma was generated in the n-base [35,36]. The degradation was associated with formation of stacking faults in the active region of the diode and the properties of the partial dislocations responsible for the stacking fault formation were studied in detail by Galeckas et al. [37,38] employing optical emission microscopy. In particular, the velocity and activation energy for the glide of partials on the basal c-plane were determined and found to be up to ~10^{-4} cm/s at RT and ~0.27 eV, respectively, in the presence of charge carrier recombination. The glide process is strongly enhanced by the recombination; in the dark, i.e., without any recombination, the activation energy is ~2.5 eV and the dislocations are practically immobile at RT. Indeed, there are several striking features corroborating an association of the long-distance migration of $Z_{1/2}$ and $S_{1/2}$ with the glide of partials: (i) charge carrier recombination is a necessary condition for both processes to take place at RT, (ii) a strong degree of

anisotropy along the (0001) basal plane is found in both cases, (iii) comparable absolute distances are obtained, 1 h at RT yields a migration length on the order of 1 mm in both cases, (iv) the DLTS signatures are broad and suggest that the $Z_{1/2}$ and $S_{1/2}$ centers appear in a distorted cystal structure (e.g., in the vicinity of an extended defect), (v) the migration lengths of $Z_{1/2}$ and $S_{1/2}$ are about the same despite their different origin/identity, possibly indicating that the diffusion is promoted by an independent process not linked to a specific point defect like C_I, and (vi) the partials anneal out at temperatures above 200 °C [39] consistent with the disappearance of the $Z_{1/2}$ and $S_{1/2}$ signals after 2h at 250 °C.

An exact mechanism of interaction between the partial dislocations and the $Z_{1/2}$ and $S_{1/2}$ centers cannot be elucidated from the present data but a distinct possibility may be that $Z_{1/2}$ and $S_{1/2}$ bind to some site in the core of the partials. However, in spite of the features (i) – (vi), one should also point out that the association of the long distance migration of $Z_{1/2}$ and $S_{1/2}$ with the glide of partial dislocations is still to be regarded as tentative and further work needs to be pursued for an unambiguous conclusion.

Summary

At RT, the prominent $Z_{1/2}$ and $S_{1/2}$ centers in 4H-SiC exhibit long distance lateral migration on the order of 1 mm outside the volume irradiated directly by a focused beam of 10 keV protons. The migration is rapid with an energy barrier of ~0.2 eV and it is strongly anisotropic along the (0001) basal plane. The presence of electron-hole pair recombination is a necessary condition and the DLTS spectra provide strong evidence of a distorted crystal structure in the vicinity of the $Z_{1/2}$ and $S_{1/2}$ centers. Ionization-enhanced defect motion plays a decisive role but is possibly driven by extended defects, like gliding of partial dislocations on the basal plane, with $Z_{1/2}$ and $S_{1/2}$ as accompanying complexes rather than by specific point defects, like C_I. Despite a rather limited fraction of defects escaping from the directly irradiated volume (≤1 %), the results imply that the minority charge carrier lifetime is adversely affected over distances of several hundreds of µm in conjunction with selective area doping by ion implantation.

Acknowledgements

The authors acknowledge gratefully financial support from the Norwegian Research Council under the FRINAT program (CAPSiC project), and are thankful to Dr. Augustinas Galeckas for the laser irradiations and for fruitful discussions.

References

[1] C. G. Hemmingsson, N. T. Son, A. Ellison, J. Zhang, and E. Janzén, Physical Review B **58**, R10 119 (1998).

[2] T. Dalibor, G. Pensl, T. Kimoto, H. Matsunami, S. Sridhara, R. P. Devaty, and W. J. Choyke, Diamond and Related Materials **6**, 1333- 1337 (1997).

[3] P B Klein, B V Shanabrook, S W Huh, A Y Polyakov, M Skowronski, J J Sumakeris, and M J O'Loughlin, Applied Physics Letters **88**, 52110 (2006).

[4] G Alfieri, E V Monakhov, B G Svensson, and M K Linnarsson, Journal of Applied Physics **98**, 43518 (2005).

[5] J W Steeds, W Sullivan, A Wotherspoon, and J M Hayes, Journal of Physics: Condensed Matter **21**, 364219 (2009).

[6] J Steeds, G A Evans, L R Danks, S Furkert, W Voegeli, M M Ismail, and F Carosella, Diamond and Related Materials **11**, 1923-1945 (2002).

[7] G Alfieri, U Grossner, E V Monakhov, B G Svensson, J W Steeds, and W Sullivan, Materials Science Forum **527-529**, 485-488 (2006).

[8] M. L. David, G Alfieri, E V Monakhov, A Hallen, C Blanchard, B G Svensson, and J F Barbot, Journal of Applied Physics **95**, 4728 (2004).

[9] T. Eberlein, C. Fall, R. Jones, P. Briddon, and S. Öberg, Physical Review B **65**, 1-4 (2002).

[10] J. C. Bourgoin and J. W. Corbett, Physics Letters **38**, 135-137 (1972).

[11] W. T. Stacy and B. J. Fitzpatrick, Journal of Applied Physics **49**, 4765 (1978).

[12] G Watkins, Journal of Crystal Growth **159**, 338-344 (1996).

[13] J. Adey, R. Jones, D. Palmer, P. Briddon, and S. Öberg, Physical Review Letters **93**, 1-4 (2004).

[14] J Schmidt, K Bothe, D Macdonald, J Adey, R Jones, and D W Palmer, Journal of Materials Research **21**, 5-12 (2006).

[15] L. I. Murin, E. a. Tolkacheva, V. P. Markevich, a. R. Peaker, B. Hamilton, E. Monakhov, B. G. Svensson, J. L. Lindstrom, P. Santos, J. Coutinho, and A. Carvalho, Applied Physics Letters **98**, 182101 (2011).

[16] B. G. Svensson, K.-H. Ryden, and B. M. S. Lewerentz, Journal of Applied Physics **66**, 1699 (1989).

[17] T. Hiyoshi and T. Kimoto, Applied Physics Express **2**, 91101 (2009).

[18] T. Hiyoshi and T. Kimoto, Applied Physics Express **2**, 41101 (2009).

[19] L. S. Løvlie, L. Vines, and B. G. Svensson, Materials Science Forum **645-648**, 431-434 (2010).

[20] J Ziegler, (2010).

[21] A. A. Istratov, Journal of Applied Physics **82**, 2965 (1997).

[22] J. P. Doyle, M. K. Linnarsson, P. Pellegrino, N. Keskitalo, B. G. Svensson, A. Schöner, N. Nordell, and J. L. Lindström, Journal of Applied Physics **84**, 1354 (1998).

[23] C. Hemmingsson, N. T. Son, O. Kordina, J. P. Bergman, E. Janzen, J. L. Lindstrom, S. Savage, and N. Nordell, Journal of Applied Physics **81**, 6155 (1997).

[24] Katsunori Danno and Tsunenobu Kimoto, Journal of Applied Physics **100**, 113728 (2006).

[25] K Fujihira, T Kimoto, and H Matsunami, Applied Physics Letters **80**, (2002).

[26] Tsunenobu Kimoto, Kouichi Hashimoto, and Hiroyuki Matsunami, Japanese Journal of Applied Physics **42**, 7294-7295 (2003).

[27] Tsunenobu Kimoto, Satoshi Nakazawa, Koichi Hashimoto, and Hiroyuki Matsunami, Applied Physics Letters **79**, 2761 (2001).

[28] I. Pintilie, L. Pintilie, K. Irmscher, and B. Thomas, Applied Physics Letters **81**, 4841 (2002).

[29] S. Sasaki, K. Kawahara, G. Feng, G. Alfieri, and T. Kimoto, Journal of Applied Physics **109**, 013705 (2011).

[30] Liutauras Storasta and Hidekazu Tsuchida, Applied Physics Letters **90**, 062116 (2007).

[31] B. G. Svensson, C. Jagadish, A. Hallén, and J. Lalita, Physical Review B **55**, 10498-10507 (1997).

[32] M. V. S. Chandrashekhar, Christopher I. Thomas, and Michael G. Spencer, Applied Physics Letters **89**, 042113 (2006).

[33] B. G. Svensson, B. Mohadjeri, A. Hallen, J. H. Svensson, and W. Corbett, Physical Review B **43**, 2292-2298 (1991).

[34] P. Pellegrino, P. Lévêque, J. Lalita, a. Hallén, C. Jagadish, and B. Svensson, Physical Review B **64**, 1-10 (2001).

[35] H. Lendenmann, Fanny Dahlquist, N. Johansson, R. Söderholm, Per Åke Nilsson, Peder Bergman, and P. Skytt, Materials Science Forum **353-356**, 727-730 (2001).

[36] Peder Bergman, H. Lendenmann, Per Åke Nilsson, Ulf Lindefelt, and P. Skytt, Materials Science Forum **353-356**, 299-302 (2001).

[37] A. Galeckas, J. Linnros, and P. Pirouz, Applied Physics Letters **81**, 883 (2002).

[38] A. Galeckas, J. Linnros, and P. Pirouz, Physical Review Letters **96**, 1-4 (2006).

[39] Joshua D. Caldwell, Kendrick X. Liu, Marko J. Tadjer, Orest J. Glembocki, Robert E. Stahlbush, Karl D. Hobart, and Fritz Kub, Journal of Electronic Materials **36**, 318-323 (2007).

Paper VI

JOURNAL OF APPLIED PHYSICS **108**, 024503 (2010)

Analysis of electron traps at the 4H–SiC/SiO_2 interface; influence by nitrogen implantation prior to wet oxidation

I. Pintilie,[1] C. M. Teodorescu,[1] F. Moscatelli,[2] R. Nipoti,[2] A. Poggi,[2] S. Solmi,[2] L. S. Løvlie,[3] and B. G. Svensson[3]
[1]*National Institute of Materials Physics, P.O. Box MG-7, Bucharest-Magurele 077125, Romania*
[2]*CNR-IMM of Bologna, via Gobetti 101, 40129 Bologna, Italy*
[3]*Department of Physics, Center for Materials Science and Nanotechnology, Oslo University, P.B. 1048 Blindern, N-0316 Oslo, Norway*

(Received 8 April 2010; accepted 3 June 2010; published online 19 July 2010)

Electron states at the SiO_2/4H–SiC interface have been investigated using capacitor structures and especially, the influence of excess nitrogen, introduced by ion implantation, at the interface is studied in detail. Implanted and nonimplanted n-type samples with an interfacial concentration of nitrogen of $\sim 10^{19}$ cm^{-3} and 10^{16} cm^{-3}, respectively, were analyzed by capacitance-voltage (C-V) measurements, performed at different temperatures and probe frequencies, and thermal dielectric relaxation current (TDRC) measurements performed in the temperature range of 35–295 K. Three main categories of electron states are disclosed, true interface states (D_{it}), fast near interface states (NIT_{ox}^{fast}) and slow near interface states (NIT_{ox}^{slow}). The density versus energy distributions of D_{it} and NIT_{ox}^{fast} have been deduced from the TDRC data and they are shown to give a close quantitative agreement with the shape and frequency dependence of the C-V curves. Further, the amount of NIT_{ox}^{slow} extracted from TDRC is demonstrated to be responsible for the parallel shifts and hysterezis effects occurring in the C-V characteristics. All three categories of electron states are reduced in concentration in the implanted samples. This holds particularly for NIT_{ox}^{fast} with a peak at ~ 0.1 eV below the conduction band edge of 4H–SiC that is suppressed by at least two orders of magnitude relative to the nonimplanted samples. The decrease for D_{it} is also substantial (a factor of ~ 10) while the loss for NIT_{ox}^{slow} is considerably smaller (only $\sim 30\%$). The results provide firm evidence that NIT_{ox}^{fast} and NIT_{ox}^{slow} do not originate from the same kind of defect center. © *2010 American Institute of Physics*. [doi:10.1063/1.3457906]

I. INTRODUCTION

Exploitation of silicon carbide (SiC) based metal-oxide-semiconductor field-effect transistors (MOSFETs) seems more feasible after the discovery of the passivating action of nitrogen (N) on the interface states of SiO_2/SiC for (0001) 4H–SiC.[1] Characterization of the SiO_2/4H–SiC interface shows that a reduction in the electron trap concentration and an increase in the electron channel mobility in the MOSFET are linked to accumulation of N at the SiO_2/SiC interface.[2–4] Recently, various N^+ implantation processes of gate areas before wet oxidation treatments have been compared for the realization of Si face 4H–SiC n-MOSFETs.[5–9] The devices with the highest N concentration at the interface ($\sim 1 \times 10^{19}$ cm^{-3}) present the highest channel mobility (22 cm^2/V s), the lowest threshold voltage (2.4 V), and the smallest subthreshold swing (310 mV/decade at drain current of 10^{-11} A). High-low frequency capacitance-voltage (C-V) measurements performed on n-MOS capacitors at room temperature reveal[9,10] a strong reduction in the electron interface trap density near the conduction band in the samples with a high N concentration at the SiO_2/SiC interface. In this work we have employed comparative studies of gate oxides that have been grown on a N^+ preimplanted area and on a virgin Si face 4H–SiC material by means of C-V characteristics, performed at different temperatures and frequencies, and thermal dielectric relaxation current (TDRC)[11,12] technique. The aim is to identify those defect states that are reduced by the N implantation. In MOS structures with no oxide traps, the density of interface states, D_{it}, can be readily extracted from TDRC measurements. However, when oxide traps are present, the TDRC spectra include also signals from these defects and a distinction between fixed oxide traps (N_{ox}), near interface oxide traps (NIT_{ox}) and pure interface states (D_{it}) is not straight forward. Previous TDRC studies of 4H–SiC n-MOS structures have revealed the existence of two groups of NIT_{ox} that can exchange charge with the underlying SiC substrate and both groups were attributed to acceptor like intrinsic defects extending from the interface into the oxide.[13–18] The composition and structure of these near interface states are not yet clarified. Possible candidates suggested by theory and/or experiments are carbon clusters, silicon suboxide states and/or silicon interstitials.[17,19,20] These NIT_{ox} have mainly been associated with a parallel shift in the C-V curves at low temperatures[14] while the defect states responsible for other features of the C-V curves (the shape and the frequency dependence) have received less attention so far. Here, we present quantitative information about the density and energy distributions of these other defect states and discuss their origin.

 © 2010 American Institute of Physics

Author complimentary copy. Redistribution subject to AIP license or copyright, see http://jap.aip.org/jap/copyright.jsp

II. EXPERIMENTAL

A. Sample preparation

MOS capacitors were fabricated on a homoepilayer grown on the Si face of an 8° off-axis 4H–SiC wafer of n-type. The n-type epilayer, obtained by N doping, was 6 μm thick and had a net donor density of 1×10^{16} cm^{-3}. A 0.6 μm thick field oxide was deposited by chemical vapor deposition and patterned to open circular gate geometry of 750 μm in diameter ($\sim$0.44 mm^2 gate contact area). Sample no. 1 received dual implantations by N ions at 2.5 and 5 keV with a total dose of 1.0×10^{15} cm^{-2} (5.0×10^{14} $+5.0\times10^{14}$ cm^{-2}) in order to obtain an amorphous layer just below the sample surface. The sample was then subjected to a low temperature (850 °C for 30 min) wet oxidation in order to oxidize the amorphous layer without any recrystallization, followed by a "standard" wet oxidation at 1100 °C for 6 h. MOS structures on sample no. 2 were obtained without any N implantation by performing a standard wet oxidation at 1100 °C for 8 h. Sputtered Al was used for the metal gates, whereas Ni was deposited for the back contact. Post metallization annealing was undertaken in forming gas at 400 °C for 30 min. The oxide thickness, evaluated from the high frequency *C*-*V* measurements on the MOS capacitors, was 58 nm and 60 nm for samples no. 1 and no. 2, respectively. Considering the as-implanted N distribution measured by secondary ion mass spectrometry on sample no. 1 and taking into account the 27 nm thick SiC layer consumed by the growth of the gate oxide, the N concentration at the SiO_2/SiC interface ($N_{interface}$) is estimated to be of the order of $\sim1\times10^{19}$ cm^{-3}.[9] This estimate assumes that the N atoms residing in SiC are immobile during the oxidation at 1100 °C. However, a partial segregation at the SiO_2/SiC interface of the N present in the SiC layer consumed by the oxidation cannot be excluded[21,22] but as a first approximation we have correlated the electrical measurements with the N concentration determined from implanted profiles at the depth consumed by the oxidation process. For sample no. 2, the N concentration at the SiO_2/SiC interface is considered as the n-epilayer doping concentration, i.e., $N_{interface}\sim1\times10^{16}$ cm^{-3}. Hence, comparing the interface properties evaluated for the MOS capacitors of samples no. 1 and no. 2, the effect of a high concentration of N, introduced by ion implantation, at the SiO_2/SiC interface can be directly elucidated.

B. Characterization details

The methods of investigations used in this work are:

(i) *C*-*V* characteristics obtained for different probe frequencies (from 1 kHz to 1 MHz) and at different temperatures (from 294 to 80 K). The *C*-*V* characteristics were measured with a small signal amplitude of 30 mV and with delay times of 0.1–30 s using a voltage step of 20 mV.

(ii) TDRC technique for determining the energy distribution and density of D_{it} and NIT_{ox}. The employed measurement procedure was to cool down the sample to 35 K, charging the defect states either at low temperature or during cooling down. Then, a reverse (discharge) bias was applied and the sample was heated to room temperature with a constant rate, β=0.2 K/s, while recording the current (signal) of trapped charge being released. The TDRC measurements were performed under different bias conditions in order to distinguish between the defect states that influence the shape and frequency dependence of the *C*-*V* curves (the fast responding states at or near the interface) and the ones that determine the parallel shift in the characteristics and the hysterezis effects (the slow responding states in the oxide).

The TDRC spectrum, i.e., the released current versus temperature, can be used to extract the energy distribution and the density of interface and oxide traps. For this purpose we adopted the procedure proposed by Simmons and co-workers.[11,12] Thus, in an n-type MOS structure, the relation between the temperature in a TDRC scan and the energy position of traps (E_t) with respect to the conduction band of the semiconductor (E_c) is described by the following relation:

$$E_c - E_t = T \times \left[1.92 \times \log_{10}\left(\frac{\nu}{\beta}\right) + 3.2\right] \times 10^{-4}\ \text{eV/K} - 0.0155\ \text{eV}, \quad (1)$$

where ν is given by

$$\nu = N_c \times v_{\text{th}} \times \sigma_n, \quad (2)$$

where σ_n—the capture cross section for electrons, assumed to have a T^{-2} temperature dependence;[11,12] v_{th}—the average thermal velocity of electrons, and N_c—the density of states in the conduction band of the semiconductor.

The density of states giving rise to the TDRC signal, $S(T)$, is deduced from

$$D(E_t) = \frac{S(T)}{q \times A \times \beta \times \left[1.92 \times \log_{10}\left(\frac{\nu}{\beta}\right) + 3.2\right] \times 10^{-4}\ \text{eV/K}}, \quad (3)$$

where q is the elementary charge and A is the area of the gate electrode.

The corresponding total charge that is trapped in the device during injection and then emitted during the TDRC temperature scan is

$$\Delta Q = \pm q \times A \times \int_0^{E_g} D(E_t)dE_t, \quad (4)$$

where E_g is the energy band gap of the material (layer) in which the charge emission takes place.

The same charge can be determined directly from the $S(T)$ signal measured between T_0 and T_f, without knowing $D(E_t)$ (e.g., when the frequency factor ν is not known) according to

Author complimentary copy. Redistribution subject to AIP license or copyright, see http://jap.aip.org/jap/copyright.jsp

$$\Delta Q = \frac{1}{\beta} \times \int_{T_0}^{T_f} S(T)dT. \tag{5}$$

Equations (1)–(5) apply to interface states (D_{it}) as well as to traps in the oxide (NIT_{ox}).

(iii) Modeling of the measured *C-V* characteristics using the following relations:[23]

- the relation between applied gate bias and band bending

$$V_G(\Psi_s) = \Psi_s - \frac{Q_{ox}}{C_{ox}} - \frac{Q_{SiC}(\Psi_s)}{C_{ox}} - \frac{Q_{it}(\Psi_s)}{C_{ox}}, \tag{6}$$

- the dependence of the total capacitance on band bending and angular frequency ω

$$C(\Psi_s,\omega) = C_{ox} \times \frac{C_{it}(\Psi_s,\omega) + C_{SiC}(\Psi_s)}{C_{ox} + C_{it}(\Psi_s,\omega) + C_{SiC}(\Psi_s)}, \tag{7}$$

where (i) C and V_G are the structure capacitance and the applied gate bias, respectively; (ii) Ψ_s is the band bending (i.e., difference between the surface and bulk potential in the semiconductor); (iii) C_{ox} and C_{SiC} are the oxide and the semiconductor capacitances, respectively; (iv) C_{it} is the real part of the interface capacitance $\tilde{C}_{it}$; (v) Q_{ox}, Q_{it}, and Q_{SiC} are the steady state values of charges in the oxide, at the interface and at the semiconductor surface, respectively.

In order to compute the *C-V* characteristics all the terms in Eqs. (6) and (7) must be determined. The oxide capacitance is given by

$$C_{ox} = \varepsilon_0 \times A/d_{ox}, \tag{8}$$

with ε_{ox} and d_{ox} being the dielectric constant and the thickness of the oxide layer, respectively.

The dependence of Q_{SiC} and C_{SiC} on the band banding Ψ_s can be calculated in a similar way as Nicollian and Brews[23] described for the case of Si based MOS structures but omitting the existence of an inversion layer

$$Q_{SiC}(\Psi_s) = \varepsilon_{SiC} \times k \times \frac{-\Psi_s \times \sqrt{N_d/N_i}\sqrt{\left(-1-\frac{q\times\Psi_s}{k\times T}\right) + e^{q\times\Psi_s/k\times T}}}{|\Psi_s| \times \sqrt{\varepsilon_{SiC} \times q \times \frac{k\times T}{2\times q^2 \times N_i}}}, \tag{9}$$

$$C_{SiC}(\Psi_s) = \frac{\frac{\varepsilon_{SiC}\times A}{\sqrt{\frac{k\times T\times\varepsilon_{SiC}}{q^2\times N_d}}} \times \frac{\Psi_s}{|\Psi_s|}\left(e^{q\times\Psi_s/k\times T} - 1\right)}{\sqrt{2\times\left(-\frac{q\times\Psi_s}{k\times T} - 1 + e^{q\times\Psi_s/k\times T}\right)}}, \tag{10}$$

where: (i) k is the Boltzmann constant; (ii) N_d and N_i are the doping and the intrinsic carrier concentrations, respectively; (iii) ε_{SiC} is the 4H–SiC dielectric constant.

Q_{ox} accounts for all mobile, fixed, and trapped charges in the oxide and produces a parallel shift of the *C-V* curves compared with the case of no charges in the oxide. The corresponding shift in the flat band voltage becomes

$$\Delta V_G = Q_{ox}/C_{ox}. \tag{11}$$

In steady state (without ac small signal) the net charge accummulated by the interface states for a certain band bending is given by the sum of charges stored by ionized donor (Q_{it}^D) and acceptor (Q_{it}^A) like states:

$$Q_{it}(\Psi_s) = Q_{it}^D(\Psi_s) + Q_{it}^A(\Psi_s), \tag{12}$$

where the probability of a trap being occupied with an electron in steady state condition (that is, equlibrium for the MOS structure), f_t^0, can be calculated using Shockley–Read–Hall statistics. Assuming that each trap exchanges carriers with only one band (E_c in our case), one obtains

$$f_t^0(\Psi_s) = \frac{1}{1 + e^{(-\Delta E_t - q\times\psi_s - q\times\eta)/k\times T}}, \tag{13}$$

where $\Delta E_t = E_c - E_t$ and $\eta = (k\times T/q)\ln(N_d/N_c)$ is the semiconductor bulk potential.

In the presence of small ac signal $\delta V_g \sim Ve^{i\omega t}$ the trap level occupation probability becomes

$$f_t = f_t^0 + \delta f_t, \tag{14}$$

where δf_t is the deviation from equilibrium given by

$$\delta f_t = \frac{q}{k\times T}\frac{f_t^0\times(1-f_t^0)}{(1+i\times\omega\times\tau)}\delta\psi_s \quad \text{with} \quad \tau = \frac{1}{\sigma_n\times v_{th}\times N_d}\frac{1}{\left(e^{q\times\Psi_s/k\times T} + e^{(-\Delta E_t - q\times\eta)/k\times T}\right)}. \tag{15}$$

The small variations in the interface charge are

$$\delta Q_{it}(\Psi_s,\omega) = -q\times A\times\int_0^{E_g} D_{it}(E_t)\times\delta f_t(E_t,\Psi_s,\omega)dE_t. \tag{16}$$

The interface capacitance is a complex quantity given by

$$\tilde{C}_{it}(\Psi_s,\omega) = \frac{-\delta Q_{it}(\Psi_s,\omega)}{\delta\Psi_s}. \tag{17}$$

The real part of $\tilde{C}_{it}(\Psi_s,\omega)$ enters in Eq. (7) and becomes

$$C_{it}(\Psi_s) = \frac{q^2}{k\times T}\times A\times\int_0^{E_g} D_{it}(E_t)\times\frac{f_t^0\times(1-f_t^0)}{(1+\omega^2\times\tau^2)}dE_t. \tag{18}$$

III. RESULTS AND DISCUSSION

A. *C-V* characteristics

Figure 1 shows examples of 1 MHz *C-V* curves measured from depletion to accumulation (D to A) and from accumulation to depletion (A to D) at different temperatures for both types of samples. The samples were kept under a depletion bias while cooling to a certain temperature and then the first measurement was performed from D to A. The

Author complimentary copy. Redistribution subject to AIP license or copyright, see http://jap.aip.org/jap/copyright.jsp

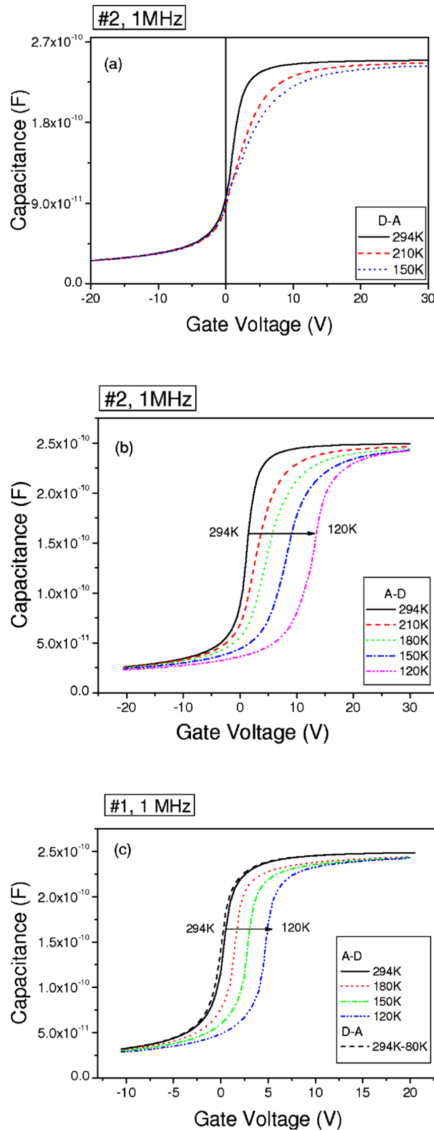

FIG. 1. (Color online) 1 MHz C-V curves measured at different temperatures on: (a) sample no. 2 from depletion to accumulation (D-A) (for clarity, results are only shown for three temperatures); (b) sample no. 2 from accumulation to depletion (A-D); and (c) sample no. 1, from depletion to accumulation (D-A) and from accumulation to depletion (A-D).

second C-V measurement at a certain temperature was performed from A to D. Before measuring at another temperature the samples were heated back to room temperature under a depletion bias. In the case of the nonimplanted sample (no. 2), both a significant change in the C-V slope and a large parallel shift are observed when lowering the temperature. Results of the first C-V scans from D to A and the subsequent ones obtained from A to D are given in Figs. 1(a) and 1(b),

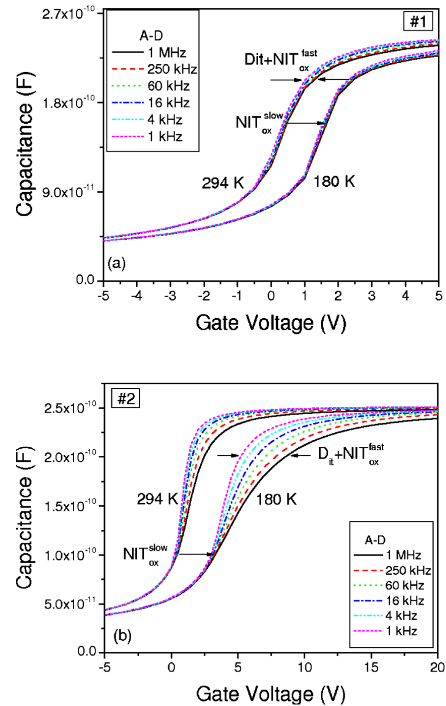

FIG. 2. (Color online) C-V characteristics measured from accumulation to depletion for frequencies between 1 kHz and 1 MHz at 180 K and room temperature on: (a) sample no. 1 and (b) sample no. 2.

respectively. For the N implanted sample (no. 1) almost no change with temperature of the C-V curves measured from D to A is observed which indicates a low density of fast states communicating with the conduction band of SiC (D_{it} and/or NIT_{ox}^{fast}). However, when measuring from A to D a parallel shift in the C-V characteristics toward more positive gate voltages occurs, Fig. 1(c), but the shift is substantially smaller than for sample no. 2. Thus, compared with sample no. 2, smaller concentrations of both NIT_{ox}^{slow}, responsible for the parallel shift in the C-V curves and fast defects states (D_{it} and/or NIT_{ox}^{fast}), are present in sample no. 1. Also the probe frequency dependence of the C-V curves for sample no. 1 confirms a strong suppression of the fast defect states (D_{it} and/or NIT_{ox}^{fast}) after the N implantation process, Fig. 2(a). In contrast, a significant spread with the frequency occurs for the C-V curves of the nonimplanted sample (no. 2) and the spread increases at low temperatures, Fig. 2(b).

For both types of samples, the amount of negative charge stored at NIT_{ox}^{slow} during the C-V scans increases with the maximum accumulation bias applied and no saturation is reached before the sample structures break. Figure 3 displays consecutive C-V curves [labeled from (1) to (5) in the figure] measured from D to A at 150 K on sample no. 2. Increasing the maximum accumulation bias, the C-V curves shift (in parallel) toward more positive gate voltages, showing that more NIT_{ox}^{slow} states become filled with electrons. The largest

Author complimentary copy. Redistribution subject to AIP license or copyright, see http://jap.aip.org/jap/copyright.jsp

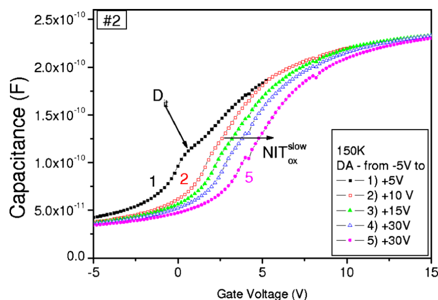

FIG. 3. (Color online) Consecutive *C-V* curves, labelled from (1) to (5), measured from D to A at 150 K for sample no. 2.

accumulation biases applied were 20 V and 30 V for samples no. 1 and no. 2, respectively, before failure occurred.

Consecutive D to A and A to D scans at low temperatures unveil two contributions to the hysteresis effect observed in Fig. 1. These become larger with lowering the temperature as well as with increasing the range of the bias applied during the measurements, as illustrated in Fig. 4 for a temperature of 150 K. The first D to A back and A to D sequence, performed up to an accumulation bias of +20 V for sample no. 1 and +30 V for sample no. 2, exhibits a large hysteresis, see, curves (1) and (2) in Fig. 4. However,

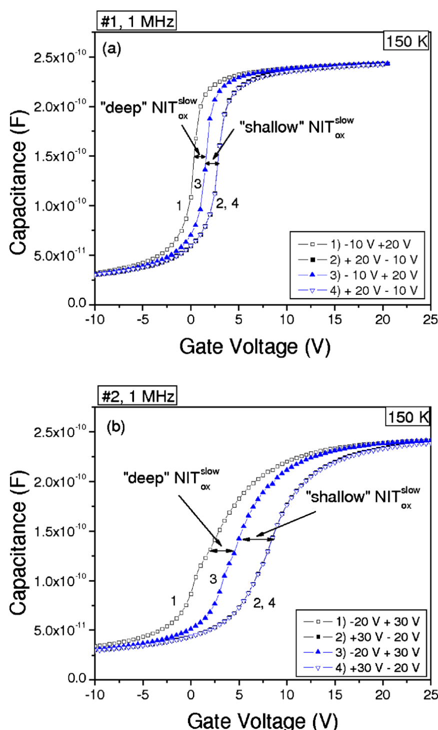

FIG. 4. (Color online) Consecutive *C-V* hysteresis measurements performed with 1 MHz at 150 K on: (a) sample no. 1 and (b) sample no. 2.

this is significantly reduced for the next D to A and A to D sequence using the same bias range, see, curves (3) and (4). The difference between the first and the third scan is due to the "frozen" charge at NIT_{ox}^{slow} that does not discharge when bringing the sample back to depletion. These traps are denoted in Fig. 4 as "deep" NIT_{ox}^{slow}. The hysteresis between the third and fourth scan remains the same as that between the second and third scan and is attributed to electrons trapped at "shallow" NIT_{ox}^{slow} that can be released during the depletion. The amount of deep and shallow NIT_{ox}^{slow} affecting the *C-V* characteristics exhibit a temperature dependence reflecting their density versus energy distributions and the associated electron capture and emission processes, as will be further discussed in Sec. III B. Here, it should be emphasized that the *C-V* characteristics display no dependence on the sweep rate used (0.67 to 200 mV/s) implying that the capture and emission processes have reached a "dynamic equilibrium," especially, the filling of deep and shallow NIT_{ox}^{slow} appears not to be limited by direct tunneling or strongly thermally activated processes but rather by "ordinary" capture processes (possibly involving the true interface states, D_{it}).

Irrespective of the sample temperature, the parallel shift in the *C-V* curves and the hysteresis effects appear only when the applied gate bias exceeds +1 and +2 V for samples no. 1 and no. 2, respectively. For lower biases, no charge is trapped in the oxide and only the interface states respond to the applied gate bias (dc as well as the ac probing voltage). The gate voltages of +1 and +2 V for samples no. 1 and no. 2, respectively, correspond closely to flat band conditions with a capacitance, C_{FB}, of ~200 pF for both samples.

B. TDRC spectra

No direct and quantitative correlation between the defect densities obtained from TDRC studies of SiC and the shape, the frequency dependence and the position of the *C-V* characteristics has previously been reported in the literature.[11–16,18] A main focus in this section is to separate the TDRC signals coming from D_{it}, NIT_{ox}^{fast}, and NIT_{ox}^{slow}, to determine their densities and energy distributions, and based on this knowledge to quantitatively explain the features of the *C-V* characteristics reported in the previous section. Accordingly, also the defect states that are reduced because of the N-implantation process (sample no. 1) can be unveiled.

Prior to recording the TDRC spectra, the samples were slowly cooled down from 295 to 35 K (~90 min), ensuring that also slow capturing states are filled with electrons when a positive gate bias is applied during the cooling; examples of recorded TDRC spectra for different positive filling (charging) biases are given in Fig. 5. As mentioned in Sec. III A., for filling voltages lower than those corresponding to C_{FB} in both type of samples no charge injection into the oxide takes place. Therefore, the TDRC spectra recorded after charging with 1 V and 2 V for samples no. 1 and no. 2, respectively, yield information about D_{it} only (shaded areas in Fig. 5). Furthermore, only those D_{it} with energy positions deep enough to be filled during these small charging biases will respond and in the following, they are denoted as deep D_{it}. The density of deep D_{it} is reduced by a factor of ~5 in

Author complimentary copy. Redistribution subject to AIP license or copyright, see http://jap.aip.org/jap/copyright.jsp

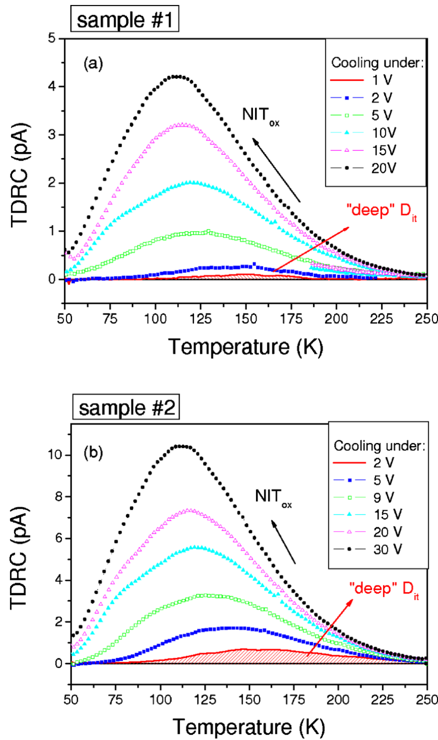

FIG. 5. (Color online) TDRC spectra for different positive biases applied during cooling on: (a) sample no. 1 and (b) sample no. 2.

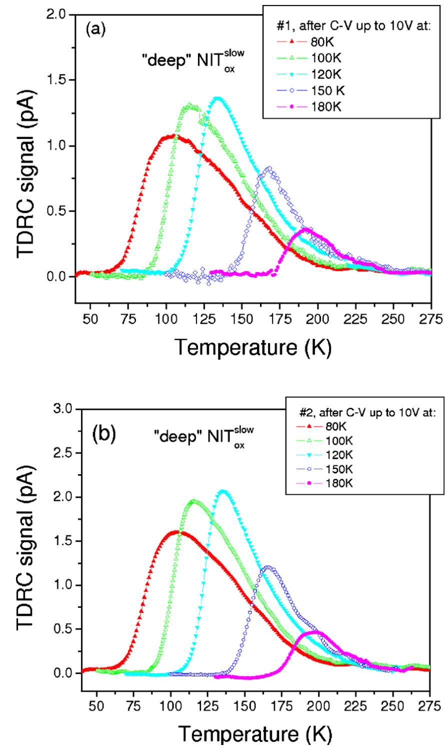

FIG. 6. (Color online) Examples of TDRC spectra recorded after *C-V* measurements performed at different temperatures in the voltage range −10 to +10 V for: (a) sample no. 1 and (b) sample no. 2.

the N-implanted sample (no. 1). The spectra corresponding to larger charging biases contain signals also from shallow D_{it} (shallower than the deep D_{it}) but they are obscured by other signals that do not reach saturation when increasing the charging bias. Thus, as already reported in literature, most of the TDRC signal recorded in this latter case comes from NIT_{ox}; these are predominantly slow states with temperature dependent capture cross sections and are the main reason for the parallel shift in the *C-V* curves at low temperature.[13–18] Since no saturation is reached when increasing the accumulation bias up to the maximum values before failure occurs, the total amount of NIT_{ox} centers in the samples cannot be determined. Nevertheless, comparing the TDRC signals corresponding to similar injection levels, Fig. 5 reveals a substantially higher density of NIT_{ox} and deep D_{it} in sample no. 2 relative to those in sample no. 1 (N-implanted), which is fully consistent with the *C-V* curves in Figs. 1 and 4. However, due to the dependence on the charging temperature, the TDRC spectra in Fig. 5 cannot be quantitatively correlated with the *C-V* curves in Figs. 1 and 4. For such a correlation, especially with respect to NIT_{ox}^{slow}, TDRC spectra need to be recorded successive to *C-V* measurements performed at a certain temperature. As shown in Fig. 4, some of the charge injected into the oxide during a *C-V* measurement will still respond to the bias applied (hysteresis produced by shallow NIT_{ox}^{slow}) while some (deep NIT_{ox}^{slow}) will not respond yielding the stable parallel shift in the *C-V* curves. We monitored the deep NIT_{ox}^{slow} directly by TDRC; after undertaking the *C-V* measurements at a certain temperature, the structure was immediately cooled down to ~40 K and then heated up for acquisition of the corresponding TDRC spectrum. For both the cooling and heating during the TDRC sequence, the maximum reverse bias applied during the *C-V* measurements (−10 V) was maintained. In Fig. 6, TDRC spectra recorded after *C-V* measurements performed at different temperatures and in the voltage range of −10 to +10 V are depicted for samples no. 1 and no. 2. The energy distribution and the density of these deep NIT_{ox}^{slow} states can be deduced from the TDRC spectra using Eqs. (1) and (3) if the attempt to escape frequency factor ν, given by Eq. (2), is known. Previous studies have shown anomalously low effective capture cross sections for these states,[13–16] and therefore, values of ν smaller than 10^8 s^{-1} have to be considered when deducing the density versus energy distributions. In addition, as mentioned above, the electron capture cross section σ_n of these centers displays a strong temperature dependence. This can be observed also in our experiments (see Fig. 6) where both the position and magnitude of the TDRC peak change with temperature, depending on the temperature where the injection was performed (here, via *C-V* measurements). Unfortunately, as long as the filling of these traps does not saturate

Author complimentary copy. Redistribution subject to AIP license or copyright, see http://jap.aip.org/jap/copyright.jsp

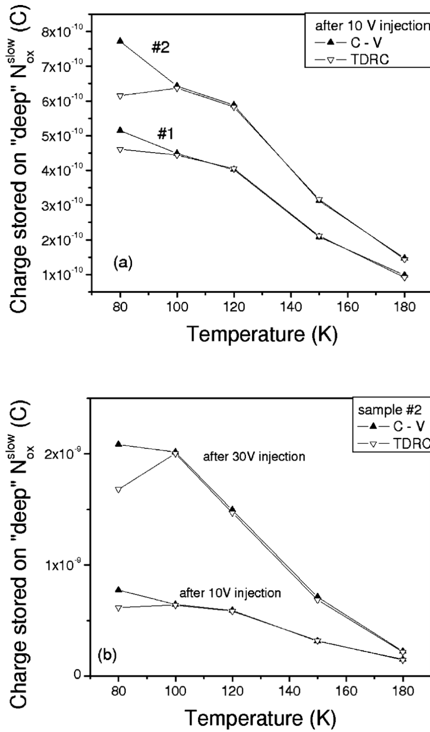

FIG. 7. Comparison between the amount of charge frozen on deep NIT_{ox}^{slow} states extracted from the TDRC spectra and from the shift in the *C-V* curves performed at different temperatures: (a) after injection with 10 V for samples no. 1 and no. 2 and (b) after injection with 10 V and 30 V for sample no. 2.

upon injection before failure of the structure occurs, accurate values for the temperature dependence of σ_n and consequently of the frequency factor ν cannot be obtained. However, the value of ν does not affect the corresponding total charge emitted during the TDRC scan, which is given by Eq. (5). The values of the charge frozen on deep NIT_{ox}^{slow} states, extracted from the TDRC spectra in Fig. 6 using Eq. (5), are represented in Fig. 7. In the same figure, the values of the charge determined from the shift in the *C-V* curves at different temperatures, according to Eq. (11), are also included. For temperatures $\geq$100 K, Fig. 7 shows a close agreement between the two sets of values and this holds for both sample no. 1 and no. 2. However, the absolute values are about a factor of 1.5 lower for sample no. 1 (N-implanted) compared to those for sample no. 2, Fig. 7(a). Hence, the N-implantation process reduces the concentration of deep NIT_{ox}^{slow}, which can be attributed to suppression of the formation of the defects giving rise to deep NIT_{ox}^{slow} and/or passivation of their electron states by the excess of implanted N atoms. Further, the TDRC spectra in Figs. 6(a) and 6(b) are rather similar in shape indicating that the N-implantation process reduces the density of all deep NIT_{ox}^{slow} states by the same relative amount, irrespective of the activation energy for electron emission. This supports an interpretation where all the deep NIT_{ox}^{slow} states originate from the same (or similar) type of defect.

For sample temperatures below 100 K, the TDRC data yield lower values of stored charge than the *C-V* data, as illustrated for 80 K in Fig. 7. This indicates the presence of shallow and/or fast enough defect states, at or near the interface (shallow D_{it} and NIT_{ox}^{fast}), which do not remain frozen in the reverse biased device but discharge during the cooling down to 35 K before the TDRC measurement is started. In order to monitor the injected charge trapped by shallow D_{it} and NIT_{ox}^{fast} the filling and subsequent appliance of reverse (discharging) bias has to be performed at a sufficiently low temperature. TDRC spectra obtained after injection at 35 K with different positive biases are presented in Fig. 8. For both samples and after accounting for the contribution of deep D_{it}, the first states to be charged are the shallow D_{it} and NIT_{ox}^{fast} and with increasing charging biases also the slow states (NIT_{ox}^{slow}) are filled. However, a main difference between the two types of samples is the pronounced presence of shallow states in sample no. 2, giving rise to the specific peak at 75 K and ascribed here to NIT_{ox}^{fast}. This type of shallow defects has previously been observed and characterized in samples with differently processed thermal oxides (dry, wet, and/or with postoxidation in N_2 or Ar/H_2 ambient);[13–18] the activation energy for electron emission and the electron capture cross section were determined to be 0.11 eV and 10^{-17} cm^2, respectively.[15] Hence, the formation/passivation of NIT_{ox}^{fast} is strongly suppressed/enhanced by the N-implantation process employed for sample no. 1. In sample no. 2, the contribution of NIT_{ox}^{fast} can be separated from the signal caused by NIT_{ox}^{slow} due to the clear signature at 75 K in the TDRC spectra. The slow oxide states start to become charged for injection voltages exceeding 8 V, see Figs. 8(a) and 8(b). NIT_{ox}^{fast} and NIT_{ox}^{slow} can be clearly deconvoluted from the difference between the TDRC spectra corresponding to 30 and 8 V charging biases and the solid line in Fig. 8(a) is attributed to the TDRC signal generated by NIT_{ox}^{fast} after injection with 30 V. This signal contains presumably also some contribution from the shallow D_{it} but it is not readily resolved from NIT_{ox}^{fast}.

As discussed previously, charging of sample no. 1 with 1 V during cooling does not produce any parallel shift in the *C-V* curves and the corresponding TDRC signal [dashed line in Fig. 8(c)] is associated with deep D_{it}; filling at 35 K with 2 V bias reproduces nicely the signal from deep D_{it} and in addition, a contribution from more shallow states occurs, see, the solid curve in Fig. 8(c). This curve is attributed to charge emission from deep D_{it}, shallow D_{it} and NIT_{ox}^{fast} which are filled at 35 K in sample no. 1 and these states are decisive for the frequency dependence of the *C-V* curves, as will be discussed further in the Sec. III C.

C. Extraction of density versus energy distributions and computation of *C-V* curves

Utilizing the TDRC spectra deduced for the fast states in sample no.1 and no. 2 [solid lines in Figs. 8(c) and 8(a)] together with Eqs. (1)–(3), the energy distributions of the

Author complimentary copy. Redistribution subject to AIP license or copyright, see http://jap.aip.org/jap/copyright.jsp

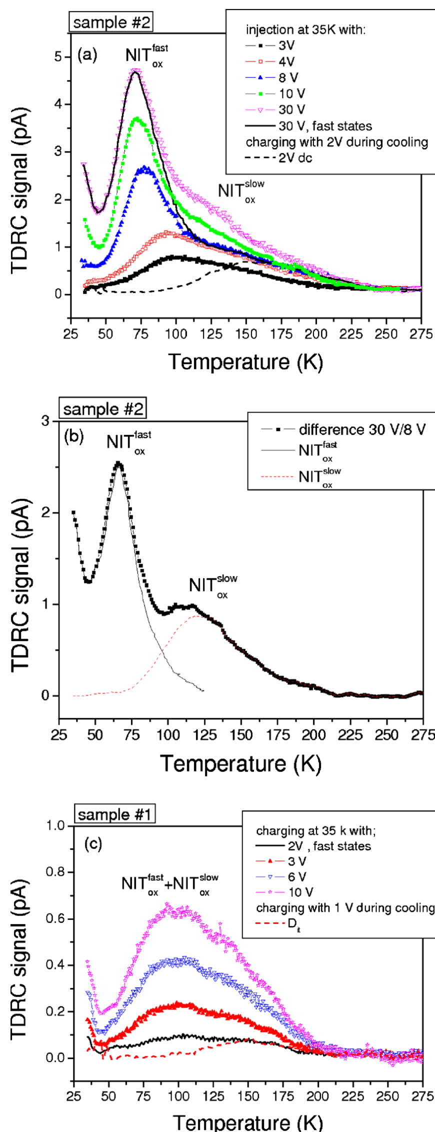

FIG. 8. (Color online) TDRC spectra obtained from (a) sample no. 2 after charging at 35 K with different positive gate biases (charging time 30 s) and after charging with 2 V during cooling (dashed line); (b) sample no. 2, deconvolution of the contributions from NIT_{ox}^{fast} and NIT_{ox}^{slow} by taking the difference between the signals recorded after injection by 30 and 8 V; and (c) sample no. 1 after charging at 35 K with different positive biases and after charging with 1 V during cooling (dashed line).

density of fast states have been extracted and the results are given in Fig. 9. In the extraction, ν is put equal to 10^9 s^{-1}, in agreement with the previously determined value of 10^{-17} cm^2 for the NIT_{ox}^{fast} capture cross section at temperatures around 75 K.[15]

Knowing the density versus energy distribution of the fast states, the shape of the C-V characteristics and the fre-

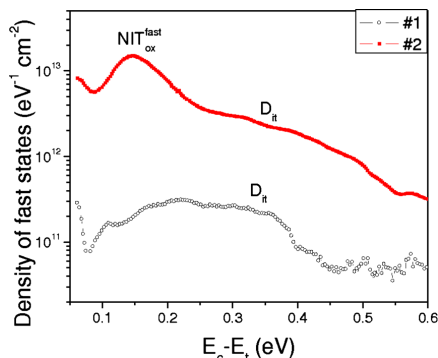

FIG. 9. (Color online) Extracted energy distribution of the density of fast states for the two types of samples.

quency dependence at different temperatures can be computed. The computations were performed using Eqs. (6)–(18) with $D(E_t)$ taken from Fig. 9. Thus, NIT_{ox}^{fast} was also included and no distinction was made relative to the “pure” D_{it}’s. For clarity, comparison is made with C-V curves recorded from A to D only (10 to −5 V and 30 to −5 V for sample no. 1 and no. 2, respectively) in order to include the effect of NIT_{ox}^{slow} causing a parallel shift in the C-V curves (Fig. 7). The computed results are given in Fig. 10 and they display a close agreement with the experimental ones shown in Fig. 2. This conclusion holds for both samples no. 1 and no. 2 and supports the validity of the distributions depicted in Fig. 9.

Further, the data in Fig. 9 illustrate the strong beneficial effect of the N-implantation on the density of fast states where the absolute values are reduced by one to two orders of magnitude in sample no. 1 relative to sample no. 2. Moreover, the shapes of the distributions differ considerably, and in particular, the peak at $\sim E_c - 0.13$ eV, primarily attributed to NIT_{ox}^{fast}, is dominant in sample no. 2 but essentially below the detection limit in sample no. 1. This provides firm evidence that NIT_{ox}^{fast} and NIT_{ox}^{slow} do not originate from the same type of defect center since the effect of the N-implantation on NIT_{ox}^{slow} is less dramatic than on NIT_{ox}^{fast} (see Figs. 6 and 7). It is tempting to speculate that the formation process of the defects responsible for NIT_{ox}^{fast} is strongly prevented by the implantation of N while the decrease in NIT_{ox}^{slow} and D_{it} is merely due to partial passivation of the corresponding defects by the excess of implanted N atoms. This speculation contradicts some previous interpretation by Rudenko *et al.*[15] and Pippel *et al.*[16] but supports the theoretical results of Deák *et al.*[20] In Ref. 20, the distinct peak at $\sim E_c - 0.1$ eV, attributed to NIT_{ox}^{fast} in Fig. 9, was ascribed to carbon dimers, originally forming at the interface and then substituting two nearby oxygen atoms in the silica layer, while the broad distribution of deep traps (NIT_{ox}^{slow}) was assigned to silicon interstitials. The observed beneficial effect of the N-implantation (strongest on NIT_{ox}^{fast}) may thus be envisaged as a substitution (or passivation) of carbon dimers with N atoms leading to a large decrease in both NIT_{ox}^{fast} and D_{it}.

Author complimentary copy. Redistribution subject to AIP license or copyright, see http://jap.aip.org/jap/copyright.jsp

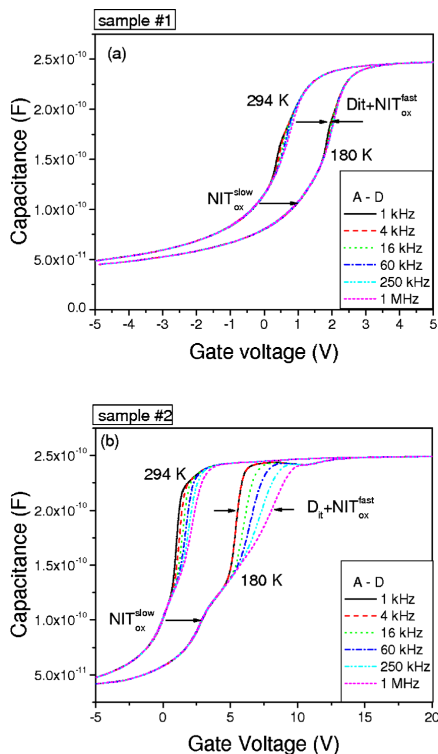

FIG. 10. (Color online) Computed *C-V* curves, from accumulation to depletion at 294 and 180 K, for: (a) sample no. 1 and (b) sample no. 2.

IV. CONCLUSIONS

Three main categories of electron states are unveiled at or near the $SiO_2/4H-SiC$ interface in capacitor structures; D_{it}, NIT_{ox}^{fast} and NIT_{ox}^{slow}. The density versus energy distributions of the fast states (D_{it} and NIT_{ox}^{fast}) have been determined by TDRC and used as input for computing the shape, temperature and probe frequency dependence of *C-V* curves. A close quantitative agreement is obtained with the measured *C-V* curves and this is valid for both sample no. 1 (N-implanted) and sample no. 2 (nonimplanted). A similar agreement between the TDRC and *C-V* data holds also for the total amount of slow states (NIT_{ox}^{slow}) in the samples and these states account for the parallel shifts and hysteresis effects of the recorded *C-V* characteristics.

Sample no. 1 exhibits a lower density of D_{it} by one order of magnitude compared to that for sample no. 2 but the shapes of the density versus energy distributions remain similar (Fig. 9). An analogous behavior is obtained for NIT_{ox}^{slow} but with a considerably smaller reduction in density ($\sim$30%). In contrast, NIT_{ox}^{fast} displays a dramatic decrease in density for sample no. 1 with at least two orders of magnitude lower values relative to sample no. 2 and a different density versus energy dependence (Fig. 9). In particular, the distinct peak associated with NIT_{ox}^{fast} at $\sim E_c-0.1$ eV is essentially below the detection limit in sample no. 1. These data suggest strongly that NIT_{ox}^{fast} and NIT_{ox}^{slow} are of different origin. A speculation where NIT_{ox}^{fast} and D_{it} are due to carbon dimers, being substituted and/or passivated by the excess of implanted N in sample no. 1, and NIT_{ox}^{slow} is due to silicon interstitials appears to be conceivable and is consistent with theoretical results in the literature.

ACKNOWLEDGMENTS

Financial support by the Norwegian Research Council (FRINAT Program) and by the Romanian National Authority for Scientific Research through the CNCSIS Project PCCE ID_76 are gratefully acknowledged.

[1]V. V. Afanas'ev, A. Stesmans, F. Ciobanu, G. Pensl, K. Y. Cheong, and S. Dimitrijev, Appl. Phys. Lett. **82**, 568 (2003).
[2]S. Dhar, S. R. Wang, J. R. Williams, S. T. Pantelides, and L. C. Feldman, MRS Bull. **30**, 288 (2005).
[3]G. V. Soares, I. J. R. Baumvol, L. Hold, F. Kong, J. Han, S. Dimitrijev, S. Radtke, and F. C. Stedile, Appl. Phys. Lett. **91**, 041906 (2007).
[4]K. Fujihira, Y. Tarui, M. Imaizumi, K. Ohtsuka, T. Takami, T. Shiramizu, K. Kawase, J. Tanimura, and T. Ozeki, Solid-State Electron. **49**, 896 (2005).
[5]F. Ciobanu, G. Pensl, V. V. Afanas'ev, and A. Schoner, Mater. Sci. Forum **483–485**, 693 (2005).
[6]G. Pensl, F. Ciobanu, T. Frank, D. Kirfmse, M. Krieger, S. Reshanov, F. Schmid, M. Weidner, T. Oshima, H. Itoh, and W. J. Choyke, Microelectron. Eng. **83**, 146 (2006).
[7]F. Ciobanu, T. Frank, G. Pensl, V. V. Afanas'ev, S. Shamuilia, A. Schoner, and T. Kimoto, Mater. Sci. Forum **527–529**, 991 (2006).
[8]F. Moscatelli, A. Poggi, S. Solmi, and R. Nipoti, IEEE Trans. Electron Devices **55**, 961 (2008).
[9]A. Poggi, F. Moscatelli, Y. Hijikata, S. Solmi, and R. Nipoti, Microelectron. Eng. **84**, 2804 (2007).
[10]A. Poggi, F. Moscatelli, Y. Hijikata, S. Solmi, M. Sanmartin, F. Tamarri, and R. Nipoti, Mater. Sci. Forum **556-557**, 639 (2007).
[11]J. S. Uranwala, J. G. Simmons, and H. A. Mar, Appl. Phys. Lett. **26**, 697 (1975).
[12]H. A. Mar and J. G. Simmons, Solid-State Electron. **17**, 131 (1974).
[13]H. Ö. Ólafsson, E. Ö. Sveinbjörnsson, T. E. Rudenko, V. I. Kilchytska, I. P. Tyagulski, and I. N. Osiyuk, Mater. Sci. Forum **389–393**, 1001 (2002).
[14]H. Ö. Ólafsson, E. Ö. Sveinbjörnsson, T. E. Rudenko, V. I. Kilchytska, I. P. Tyagulski, and I. N. Osiyuk, Mater. Sci. Forum **433–436**, 547 (2003).
[15]T. E. Rudenko, I. N. Osiyuk, I. P. Tyagulski, H. O. Olafsson, and E. O. Sveinbjornsson, Solid-State Electron. **49**, 545 (2005).
[16]E. Pippel, J. Woltersdorf, H. O. Olafsson, and E. O. Sveinbjornsson, J. Appl. Phys. **97**, 034302 (2005).
[17]K. McDonald, R. A. Weller, S. T. Pantelides, L. C. Feldman, G. Y. Chung, C. C. Tin, and J. R. Williams, J. Appl. Phys. **93**, 2719 (2003).
[18]F. Allerstam, H. Ö. Ólafsson, G. Gudjónsson, D. Dochev, E. Ö. Sveinbjornsson, T. Rödle, and R. Jos, J. Appl. Phys. **101**, 124502 (2007).
[19]J. M. Knaup, P. Deak, Th. Frauenheim, A. Gali, Z. Hajnal, and W. J. Choyke, Phys. Rev. B **72**, 115323 (2005).
[20]P. Deák, J. M. Knaup, T. Hornos, C. Thill, A. Gali, and T. Frauenheim, J. Phys. D: Appl. Phys. **40**, 6242 (2007).
[21]J. W. Palmour, R. F. Davis, H. S. Kong, S. F. Corcoran, and D. P. Griffis, J. Electrochem. Soc. **136**, 502 (1989).
[22]G. Pensl, S. Beljakowa, T. Frank, K. Gao, F. Speck, T. Seyller, L. Ley, F. Ciobanu, V. Afanas'ev, A. Stesmans, T. Kimoto, and A. Schoner, Phys. Status Solidi B **245**, 1378 (2008).
[23]E. H. Nicollian and J. R. Brews, *MOS (Metal Oxide Semiconductor) Physics and Technology* (Wiley, New York, 1982).

Author complimentary copy. Redistribution subject to AIP license or copyright, see http://jap.aip.org/jap/copyright.jsp

Paper VII

Paper VIII